

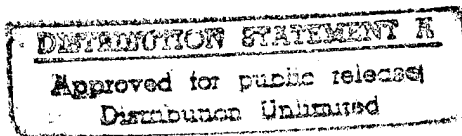
N83-13177

EFFECT OF MATRIX RESIN ON THE IMPACT FRACTURE CHARACTERISTICS
OF GRAPHITE-EPOXY LAMINATES

P. E. Hertzberg, et al

Boeing Commercial Airplane Company
Seattle, WA

Jan 82



19960321 046

ASCE

U.S. DEPARTMENT OF COMMERCE
National Technical Information Service

NTIS

1996 QUARTERLY INDEX NUMBERED 1

N83-13177

NASA Contractor Report 165784

EFFECT OF MATRIX RESIN ON THE IMPACT FRACTURE
CHARACTERISTICS OF GRAPHITE-EPOXY LAMINATES

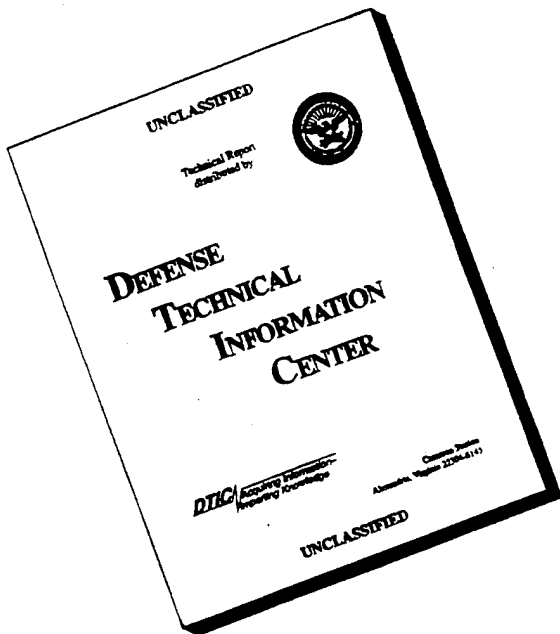
P. E. Hertzberg, B. W. Smith, and A. G. Miller

Boeing Commercial Airplane Company

Seattle, Washington

Prepared for
Langley Research Center
under Contract NASI-15107

DISCLAIMER NOTICE



**THIS DOCUMENT IS BEST
QUALITY AVAILABLE. THE
COPY FURNISHED TO DTIC
CONTAINED A SIGNIFICANT
NUMBER OF PAGES WHICH DO
NOT REPRODUCE LEGIBLY.**

1. Report No. NASA CR 165784	2. Government Accession No.	3. Recipient's Catalog No.	
4. Title and Subtitle EFFECT OF MATRIX RESIN ON THE IMPACT FRACTURE CHARACTERISTICS OF GRAPHITE-EPOXY LAMINATES		5. Report Date January 1982	
7. Author(s) P. E. Hertzberg, B. W. Smith, and A. G. Miller		6. Performing Organization Code	
9. Performing Organization Name and Address Boeing Commercial Airplane Company P.O. Box 3707 Seattle, Washington 98124		8. Performing Organization Report No. D6-51677	
12. Sponsoring Agency Name and Address National Aeronautics and Space Administration Washington, DC 20546		10. Work Unit No.	
15. Supplementary Notes Langley Technical Monitor: Marvin Rhodes Final Report		11. Contract or Grant No. NAST-15107	
16. Abstract This report presents the results of an investigation into the effect of resin chemistry on basic impact-energy-absorbent mechanisms exhibited by graphite-epoxy composites. Impact fracture modes and microscopic resin deformation characteristics were examined for 26 NASA-impacted graphite-epoxy laminates with different resin chemistries. Discrete specimen fracture modes were identified through cross-sectional examination after impact and subsequently compared with measured glass transition temperatures, cure cycles, and residual impact capabilities. Details of microscopic resin deformation mechanisms and their overall relationship to impact loading conditions, voids, and resin content also were characterized through detailed scanning electron microscopic examination of separated fracture surfaces.			
17. Key Words (Suggested by Author(s)) Composite Graphite-epoxy Impact Resin Toughness		18. Distribution Statement UNCLASSIFIED-UNLIMITED	
19. Security Classif. (of this report) UNCLASSIFIED	20. Security Classif. (of this page) UNCLASSIFIED	21. No. of Pages 130	22. Price

CONTENTS

	Page
1.0 SUMMARY	1
2.0 INTRODUCTION	2
3.0 TECHNICAL APPROACH AND RESULTS	4
3.1 Impact Damage Level Assessment	4
3.2 Chemical Characterization	4
3.3 Instrumented Impact	5
3.4 Fractographic Examination	5
4.0 DISCUSSION	7
4.1 Fracture Mechanisms	7
4.2 Resin Deformation Analysis	10
4.2.1 Neat Resin Versus Composite Fracture: Cycom 937	10
4.2.2 Mechanism 1: Air Logistics I	12
4.2.3 Mechanism 2: Narmco 107	14
4.2.4 Mechanism 2: Ciba 4	15
4.2.5 Mechanism 3: Ciba IM	16
4.2.6 Mechanism 3: Hexcel I	17
4.2.7 Mechanism 3: Cycom 919	18
4.2.8 Effect of Resin Content: BP-907 and BP-907-LR	19
4.2.9 Mechanism 4: Narmco X1114	20
4.2.10 Mechanism 4: Fibredux 920	21
5.0 CONCLUSIONS	23
APPENDIX--SPECIMEN CROSS SECTIONS	25
REFERENCES	52

TABLES

No.		Page
1	Specimen Generic Chemistry	53
2	Specimen Characteristics as Delivered	54
3	Residual Impact Properties	55

FIGURES

No.		Page
1	Fracture Mechanisms	56
2	Fracture Mechanism Versus Glass Transition Temperature, As-Received Specimens	57
3	Fracture Mechanism Versus Impact Velocity, As-Received Specimens	58
4	Fracture Mechanism Versus Cure Temperature, As-Received Specimens	58
5	Maximum Load After Incipient Load Versus Glass Transition Temperature, Impacted Specimens	59
6	Incipient Load/ (Thickness)(Width) Versus Glass Transition Temperature, Impacted Specimens	60
7	Neat Resin Fracture, Narmco 5208 (200X)	61
8	Neat Resin Fracture, Cycom 937 (200X)	61
9	Fracture Origin, Neat Resin, Narmco 5208 (500X)	62
10	Crack Propagation Zone, Neat Resin, Narmco 5208 (1000X)	62
11	Fracture Origin, Neat Resin, Cycom 937 (10,000X)	63
12	Crack Propagation Zone, Neat Resin, Cycom 937 (50,000X)	63
13	Elastomer Deformation Pits, Cycom 937 (19X)	64
14	Elastomer Deformation Pits, Cycom 937 (500X)	64
15	Interlaminar Fracture, Cycom 937 (100X)	65
16	Interlaminar Fracture, Cycom 937 (200X)	65
17	Interlaminar Fracture, Cycom 937 (500X)	66
18	Interlaminar Fracture, Cycom 937 (2000X)	66
19	Resin-Fiber Bonding, Cycom 937 (2500X)	67
20	Static Notched Tension Failure, Origin, Cycom 937 (1000X)	67
21	Static Notched Shear Failure, Propagation Zone, Cycom 937 (1000X)	68
22	Static Notched Shear Failure, Different Area, Cycom 937 (1000X)	68
23	Compression-Loaded Interlaminar Shear Failure, Cycom 937 (100X)	69

No.		Page
24	Compression Shear Delamination (Note Voids), Cycom 937 (350X)	69
25	Static Notched Shear Failure, Propagation Zone, Cycom 937 (500X)	70
26	Fiber-Matrix Bonding, Compression Shear, Cycom 937 (5000X). .	70
27	Static Notched Tension Failure, Origin, Cycom 937 (1000X) . . .	71
28	Static Notched Tension Failure, Propagation Zone, Cycom 937 (1000X)	71
29	Delamination Face, -45-deg Ply, Air Logistics I (51X)	72
30	Delamination Face, -45-deg Ply, Air Logistics I (200X)	72
31	Plastic Deformation of Resin Around Fibers, Air Logistics I (500X)	73
32	Extreme Resin Deformation, Air Logistics I (5000X)	73
33	Fiber-Matrix Bonding, Air Logistics I (5000X)	74
34	Covering Resin Layer, Air Logistics I ((10,000X))	74
35	Compression Fracture, Air Logistics I (16X)	75
36	Compression Shear, Air Logistics I (500X)	75
37	Transverse Compression Intraply Failure, Air Logistics I (500X)	76
38	Compression Shear with Large Plastic Flow, Air Logistics I (500X)	76
39	Fiber-Matrix Bond, Compression Side, Air Logistics I (5000X)	77
40	Fiber-Matrix Bond, Compression Side, Air Logistics I (10,000X)	77
41	Plastic Flow, Shear Interlaminar Failure, Narmco 107 (100X)	78
42	Plastic Flow, Shear Interlaminar Failure, Narmco 107 (500X)	78
43	Flow of Resin Under Shear Loads, Narmco 107 (5000X)	79
44	Hairy Appearance, Possible Elastomer Formation, Narmco 107 (10,000X)	79
45	Resin-Fiber Bonds, Narmco 107 (1000X)	80
46	Resin-Fiber Bonds, Narmco 107 (10,000X)	80

No.		Page
47	Compression-Loaded Shear, Narmco 107 (100X)	81
48	Transverse Fracture from Compression Side, Narmco 107 (100X)	81
49	Compression Shear, Narmco 107 (500X)	82
50	Transverse Fracture of 90-deg Ply, Narmco 107 (500X)	82
51	Transverse Ply Fracture, Compression Side, Narmco 107 (1000X)	83
52	Hairy Skin Fracture Appearance, Shear-Loaded, Narmco 107 (5000X)	83
53	Compression Shear Hairs, Narmco 107 (20,000X)	84
54	Delamination Fracture, Tension Side, Ciba 4 (100X)	84
55	Apparent Brittle Fracture, Delamination Face, Ciba 4 (500X)	85
56	Apparent Brittle Fracture, Ciba 4 (500X)	85
57	Notched Shear Static Failure, Narmco 5208 (900X)	86
58	Notched Shear Static Failure, Different Area, Narmco 5208 (1000X)	86
59	Resin Tension Fracture, Ciba 4 (2000X)	87
60	Resin Tension Fracture, Different Area, Ciba 4 (2000X)	87
61	90-deg Tension Failure Near Origin, Narmco 5208 (1000X)	88
62	90-deg Tension Failure, Propagation Zone, Narmco 5208 (1000X)	88
63	Fiber-Matrix Bond, Ciba 4 (10,000X)	89
64	Compression-Loaded Interlaminar Fracture, Ciba 4 (100X)	89
65	Compression-Loaded Interlaminar Shear Failure, Ciba 4 (500X)	90
66	Compression-Loaded Interlaminar Shear Failure, Ciba 4 (1000X)	90
67	Tension Failure, Ciba IM (17X)	91
68	Typical Crossply Failure, Significant Pullout, Ciba IM (200X)	91
69	Delamination Face, Ciba IM (500X)	92
70	Delamination Face, More Pronounced, Ciba IM (500X)	92
71	Resin Side of Fracture Delamination Face, Ciba IM (500X)	93

No.		Page
72	Fiber-Matrix Bonding, Ciba IM (10,000X)	93
73	Neutral Axis, Ciba IM (200X)	94
74	Neutral Axis, Ciba IM (500X)	94
75	Neutral Axis, Ciba IM (500X)	95
76	Influence of Voids on Fracture, Ciba IM (1000X)	96
77	Delamination Plane with Transverse Cracks, Hexcel I (100X) . .	96
78	Plastic Flow on Shear Interlaminar Plane, Hexcel I (500X) . . .	96
79	Good Resin Ductility, Transverse Tension Loading, Hexcel I (4000X)	97
80	Resin Flow with Pits, Hexcel I (10,000X)	97
81	Resin Plastic Flow, Compression-Loaded Shear, Hexcel I (5000X)	98
82	Resin Ductility, Hexcel I (5000X)	98
83	Resin Flow, Hexcel I (10,000X)	99
84	Resin Flow, Different Area, Hexcel I (5000X)	99
85	Apparent Brittle Fracture, Cycom 919 (100X)	100
86	Apparent Brittle Fracture, Cycom 919 (500X)	100
87	Hairy Appearance, Resin Whiskers, Cycom 919 (5000X)	101
88	Feathered Hackles Indicating Plastic Flow, Cycom 919 (1000X)	101
89	Resin-Fiber Bond, Cycom 919 (5000X)	102
90	Compression-Loaded Shear, Cycom 919 (500X)	102
91	Resin-Fiber Bond, Cycom 919 (5000X)	103
92	Resin-Fiber Bond, Exposed Fibers, Cycom 919 (10,000X)	103
93	Delamination Face, BP-907 (100X)	104
94	Similar Delamination Face, BP-907-LR (100X)	104
95	Delamination Face, BP-907 (500X)	105
96	Delamination Face, BP-907-LR (500X)	105
97	Ductile Resin Failure, BP-907 (2000X)	106
98	Brittle Cleavage Failure, BP-907-LR (2000X)	106
99	Microscopic Fracture Mechanism, BP-907 (5000X)	107
100	Microscopic Fracture Mechanism, BP-907-LR (5000X)	107
101	Resin-Fiber Bond, BP-907 (10,000X)	108
102	Resin-Fiber Bond, BP-907-LR (10,000X)	108

No.		Page
103	Compression-Loaded Shear Delamination, BP-907 (100X)	109
104	Compression-Loaded Shear Delamination, BP-907-LR (100X) . . .	109
105	Ductile Flow, BP-907 (500X)	110
106	Ductile Flow, BP-907-LR (500X)	110
107	Microscopic Fracture Appearance, BP-907 (5000X)	111
108	Microscopic Fracture Appearance, BP-907-LR (5000X)	111
109	Shear Delamination, Narmco X1114 (100X)	112
110	Shear Delamination, Narmco X1114 (500X)	112
111	Deformed Resin After Shear, Narmco X1114 (500X)	113
112	Tension Failure, 90-deg Ply, Narmco X1114 (540X)	113
113	Delamination Face, Narmco X1114 (1000X)	114
114	Fiber-Matrix Bond, Narmco X1114 (5000X)	114
115	Compression-Loaded Shear, Narmco X1114 (100X)	115
116	Compression-Loaded Shear, Narmco X1114 (500X)	115
117	Deformed Resin at Crossply Boundary, Narmco X1114 (500X) . .	116
118	Deformation Pits in Flowed Resin, Narmco X1114 (5000X) . .	116
119	Possible Microvoid Formation in Strained Resin, Narmco X1114 (5000X)	117
120	Fiber-Matrix Bond, Narmco X1114 (5000X)	117
121	Possible Microvoid Initiation and Growth, Narmco X1114 (20,000X)	118
122	Delamination Face, Fibredux 920 (100X)	118
123	Ductile Flow Around Fibers at Interlaminar Boundary, Fibredux 920 (500X)	119
124	Crack Propagation After Fiber Failure, Fibredux 920 (5000X)	119
125	Fiber-Matrix Bond, Fibredux 920 (10,000X)	120
126	Compression-Loaded Shear at Interlaminar Boundary, Fibredux 920 (100X)	120
127	Compression Side Shear, Fibredux 920 (500X)	121
A-1	Air Logistics I	26
A-2	BP-907	27
A-3	BP-907-LR	28
A-4	Ciba I	29

No.		Page
A-5	Ciba 1M	30
A-6	Ciba 2	31
A-7	Ciba 3	32
A-8	Ciba 4	33
A-9	Cycom 919	34
A-10	Cycom 937	35
A-11	Cycom 982	36
A-12	Fibredux 920	37
A-13	Fibredux 920/AS4	38
A-14	Hercules 3501-6/AS4	39
A-15	Hexcel 1	40
A-16	Hexcel 2	41
A-17	HYE 976	42
A-18	Narmco 107	43
A-19	Narmco X108	44
A-20	Narmco X109	45
A-21	Narmco X1114	46
A-22	Narmco 5208	47
A-23	Narmco 5208 (14-hr Cure)	48
A-24	Narmco 5235	49
A-25	U.S. Poly 1	50
A-26	U.S. Poly 2	51

EFFECT OF MATRIX RESIN ON THE IMPACT FRACTURE CHARACTERISTICS OF GRAPHITE-EPOXY LAMINATES

P. E. Hertzberg, B. W. Smith, and A. G. Miller

Boeing Commercial Airplane Company

1.0 SUMMARY

This report presents the results of an investigation into the effect of resin chemistry on graphite/epoxy impact fracture characteristics. Twenty-six graphite/epoxy laminates with different resin chemistries, impacted and sectioned by NASA, were examined. Primary emphasis was placed on identifying overall macroscopic internal damage types and discrete resin deformation mechanisms. Additional analyses were performed to examine possible correlations among observed fracture characteristics, residual impact behaviors, and material glass transition temperatures.

Submitted samples were characterized through the following procedures:

- Impact damage level assessment
- Chemical characterization
- Instrumented impact
- Fractographic examination

Results of this investigation demonstrate that composite materials subjected to impact characteristically fracture by some combination of tension intraply cracking and shear-induced delamination. Furthermore, the relative amount of tension intraply cracking and shear-induced delamination can be significantly altered by resin chemistry. Based on the relative amounts of each type of fracture, four fracture mechanism categories were established. Comparison of each of these four categories with provided chemistry and cure cycle data, impact velocity, residual impact behavior, and measured glass transition temperatures revealed no correlatable relationships except in the specific case where glass transition temperatures were compared with qualitative impact categories.

Detailed fractographic examination of separated impact fracture surfaces revealed several distinct energy-absorbent fracture mechanisms dependent on resin chemistry. Three predominant deformation mechanisms were observed: (1) brittle cleavage, (2) overall continuous matrix ductility, and (3) combinations of both in two separate phases. Additional fractographic examinations revealed no dissimilarities between high- and low-speed impact conditions, nor were interlaminar voids found to act as crack initiation sites.

2.0 INTRODUCTION

Graphite/epoxy composite materials are being used increasingly in both commercial and military aircraft. Traditionally, use of graphite/epoxy materials has been confined to secondary, noncritical structure. However, requirements for reduced structural weight and improved aircraft performance and efficiency are making composite materials increasingly competitive for expanded usage in primary, load-carrying structure.

Use of advanced composite materials in both primary and secondary structure requires durable structures that are resistant to service environments, such as moisture, elevated temperature, and impact damage. Studies by NASA and the aircraft industry have demonstrated that accidental damage, particularly ballistic-type impact, produces the most pronounced decrease in compression strength (strain) for state-of-the-art graphite/epoxy composite materials. The residual strength (strain) capability associated with nonvisible levels of impact damage often defines the minimum strength capability for compression-loaded composite structures.

As a result of the pronounced impact-residual strength sensitivity of composite materials, significant effort has been expended to develop materials with improved impact characteristics. Variation of matrix resin formulation is the most widely accepted approach for improving impact resistance. Resin modification studies, such as performed under NASA Contract NASI-12675 (ref 1), have defined, in general, the fundamental resin properties needed to achieve improved impact resistance. However, the specific energy-absorbent fracture mechanisms by which improved impact resistance occurs for these same resin modifications have not yet been investigated. The program reported herein examined the effect of resin modifications on impact failure modes and fracture characteristics.

Twenty-six graphite/epoxy laminates with different resin chemistries were submitted by NASA-Langley Research Center to Boeing Commercial Airplane Company (BCAC) for failure/fracture analysis. The submitted specimens were impacted at various high speeds--approximately 107 m/s (350 ft/s)--and sectioned through the impact centerline by NASA before submittal to BCAC.

Variations in resin chemistry and content were obtained from commercial prepreg suppliers, who modified resin formulations at their discretion to produce matrices with improved impact resistance. Narmco 5208 and Hercules 3501-5A were included as standard systems representing state-of-the-art epoxy formulations. Twenty-one of the submitted specimens represent chemistry formulations investigated under NASA Contract NASI-12675. Specific manufacturer's product designations, recommended cure temperatures, and approximate generic resin chemistries are listed in Table I.

Use of commercial products or names of manufacturers in this report does not constitute official endorsement of such products or manufacturers, either expressed or implied, by the National Aeronautics and Space Administration.

3.0 TECHNICAL APPROACH AND RESULTS

Failure modes and fracture characteristics for each of the 26 submitted specimens were examined in four phases:

- Impact Damage Level Assessment
- Chemical Characterization
- Instrumented Impact
- Fractographic Examination

In all phases, state-of-the-art fractographic/failure analysis techniques were used, with particular emphasis on the identification of morphological features and fracture modes indicative of energy-absorbent mechanisms.

3.1 IMPACT DAMAGE LEVEL ASSESSMENT

As-received impacted specimens were examined to ascertain the level and type of damage produced by the NASA impact tests. Damage assessments were performed by polishing the exposed, NASA-sectioned, impact centerlines using standard metallographic techniques. The photomicrographs obtained are included in the appendix.

Based on examination of these photomicrographs, four distinct fracture mechanisms were identified, as illustrated in Figure 1. Table 2 lists the impact velocities and fracture mechanisms exhibited for each of the 26 submitted specimens. The apparent dependence, or lack of dependence, of fracture mechanism on impact velocity and cure temperature is illustrated in Figures 2 and 3.

3.2 CHEMICAL CHARACTERIZATION

Because of the wide variations in impact damage revealed by metallographic examination, some chemical characterization of the cured specimen matrices was desirable. The chemical compositions of each resin system prior to cure are listed in Table 1. This generic information was supplied by NASA.

Chemical characterization of the submitted cured laminates was limited to evaluation of the resin glass transition temperature (T_g) by thermomechanical analysis (TMA). T_g values for the 26 submitted specimens are listed in Table 2. It should be noted that

several specimens exhibited more than one Tg. The effect of Tg on exhibited fracture mechanisms is illustrated in Figure 4.

3.3 INSTRUMENTED IMPACT

Instrumented impact testing was performed both to evaluate secondary residual impact characteristics and to generate separated fracture surfaces under impact loading conditions for subsequent scanning electron microscopy (SEM) characterization. Specimens were impacted at the site of the original ball impact with an Effects Technology, Inc. (ETI) instrumented drop tower at approximately 1.5 m/s (4.9 ft/s). The original impact site was used as an impact target, so that any damage present would continue to propagate in the same mode as under the NASA impact conditions.

So that instrumented impact data could be compared without elaborate analysis, specimens were cut to the same approximate length and held in a standard Charpy, three-point load fixture. Values of incipient damage load (P_I) and peak load (P_F) are listed in Table 3. Tg effects on P_I and P_F values are illustrated in Figures 5 and 6.

3.4 FRACTOGRAPHIC EXAMINATION

Impact-generated fracture surfaces were examined to evaluate both resin deformation characteristics and the general quality of fiber-matrix adhesion. After instrumented impact, specimens were separated into two pieces, coated with Au/Pd, and examined using SEM. Typical magnifications of 100X to 500X were used to show the presence or absence of voids and inclusions and the general fracture appearance on the single ply level. Inspection at higher magnifications, 1000X to 5000X, was used to examine details of matrix resin deformation and second-phase elastomer inclusions, if present. Details of microscopic deformation of both base resins and second-phase particles also are revealed at these magnifications.

The presence or absence of residual resin on graphite fibers was ascertained by inspection at 10 000X magnification. Subsequent ranking of fiber-matrix bond strength was done qualitatively for a variety of fracture planes using a disbond/no-disbond criterion.

Fracture surfaces and resin deformation morphologies are illustrated in Figures 7 through 127. Fracture characteristics of unreinforced elastomer-modified and non-elastomer-modified neat resins are included in Figures 7 through 14, to provide a background for interpreting the effect of elastomeric modification without the complicating addition of either fibers or impact load conditions.

For the impact-damaged laminates (figs. 15 through 124), stress conditions under the indenter are not well defined. However, for the purpose of this report, intraply cracking will be referred to as transverse tension cracking. Delamination or interply (laminar) cracking will be defined as compression-loaded shear or tension-loaded shear cracking, depending on the position of the cracks relative to the specimen neutral axis and the impact direction.

4.0 DISCUSSION

The impact event includes both initiation and propagation of damage. The damage initiation phase, as well as some propagation, was accomplished in each specimen by the NASA impact. The actual mechanisms of crack initiation and propagation are not well defined in any of the specimens examined. For example, it is not clear whether cracks initiate under some stress state within a ply and then propagate to an interlaminar area, creating an interlaminar crack, or if both types of cracks are initiated repeatedly and simply interconnect at these points by separate and different propagation mechanisms. In no case were definite fracture origins identified, and it must be recognized that all the SEM photographs are views of damage propagation produced by either the initial NASA impact or the second impact produced by the ETI instrumented drop tower. No differences were detected by fractography that would indicate that the damage produced by the second impact is different from that produced by the first.

4.1 FRACTURE MECHANISMS

Results of the microstructural evaluation (see photomicrographs contained in the appendix) were used to separate the specimen fracture mechanisms into four categories based on the relative amounts of interlaminar or intralaminar fracture, as shown in schematic form in Figure 1. Table 3 lists the fracture mechanisms exhibited by each specimen. The microstructural photographs were taken of the samples as received from NASA. Therefore, the evaluation of the photographs considers only the damage introduced by the aluminum ball impact before submittal to BCAC. The appropriate microstructural montage should be viewed before consideration of the SEM photographs described later.

The specimen that has been determined to fail by mechanism 1, tension-dominated cracking, is Air Logistics 1. This failure is unique and is among the least well-defined. The failure is typified by very little or no interlaminar cracking, and all visible damage is restricted to the tension side of the impact event. All observed cracking is restricted in length to intraply areas and seems to be confined to the matrix only.

Mechanism 2 failure also is tension-dominated, with restricted amounts of interlaminar cracking. As one would expect, the longest cracks found under these

conditions occur at the 0/90-deg ply interfaces, where laminate theory predicts the plane of maximum shear stress at a point removed from the impact site. This plane (ref 2) has been determined to be the plane of minimum fracture toughness for a laminated composite, and the combination of maximum stress and minimum toughness produces large delaminations. The only resistance to crack propagation in this mode comes from the irregular contour of the interply boundary and the inherent toughness of the matrix resin. Varying results obtained from specimens falling into this category appear to be a function of matrix fracture toughness, since the boundary contours should be the same for each specimen.

Materials that failed by mechanism 3 appear to be the least tough of all those submitted. These materials have very extensive delaminations on 0/90- and ± 45 -deg ply interfaces, as well as tension cracks in almost all plies, including the impact surface ply. A typical mechanism 3 fracture is shown in the photomicrographs of Narmco 5208 or Ciba I. The severely damaged specimens of this type also have damage on the compression side of the specimen, including the indenter area. It is not clear whether this damage occurred due to compression loading or by shear, because the material in this area appears to be shattered into small pieces.

Mechanism 4 materials are best described as delamination-prone. These specimens, like those failing by mechanism 3, are extensively delaminated at 0/90- and ± 45 -deg ply interfaces. The delaminations appear to run almost the entire length of the specimens, indicating that the propagation of cracks is extremely easy in these resins. However, the intensity of intraply tension cracks connecting the delaminations appears to be very low, leading to the supposition that these resins may have very different mode I and mode II fracture toughness. It should be noted that all samples, including those that failed via mechanism 4, have some tension cracks, especially in the ply farthest away from the indenter.

The results of the segregation can be seen graphically in Figure 2. The x-axis on this plot may be considered to be a visual estimate of the composite fracture toughness under impact conditions. The impact event or condition includes initiation and propagation of cracks, while conventional fracture toughness measurements are concerned with crack propagation only.

The amount of damage sustained from the impact events used for this study seems to depend on resin chemistry. However, a wide range of impact velocities was not a test variable. The dependence of the damage mechanism on the limited impact velocity ranges used is shown in Figure 3.

One common view of resin properties with respect to impact response is that 121°C (250°F) curing resins have better impact resistance than 177°C (350°F) curing materials. This view does not seem to apply to the materials used in this study, as shown in Figure 4. However, systematic changes in cure temperature were not applied to a single system, since each resin was cured per the manufacturer's recommendations.

As indicated in Section 2.0, 21 of the resin chemistries studied within this program were similarly examined under NASA Contract NASI-12675 (ref 1). Results of this contract showed that neat resin mechanical properties, such as modulus, ultimate strain, and ultimate strength, can be correlated and used to predict composite ultimate strength behaviors and approximate impact zone damage sizes. However, subsequent comparisons of neat resin properties with impact fracture modes identified within this program do not appear to bear out this same correlation. This result agrees well with internal Boeing studies (ref 2), which have, in general, demonstrated that neat resin properties do not correlate with either composite fracture toughness or impact resistance.

As a specific example, Narmco 5208, Ciba 3, and USP I were all determined in the current program to have failed by mechanism 3. However, examination of neat resin behavior reported under Contract NASI-12675 indicates that, for the same identified fracture mechanisms, differences of up to 41% in modulus, 76% in ultimate strain, and 50% in ultimate strength exist for these three resins. The disparity that appears to exist between the fracture mechanisms identified within this program and those correlations reported under Contract NASI-12675 may be attributable to the way in which impact damage levels were assessed. Damage levels and types examined within this program were assessed through cross-sectional methods in which particular emphasis was placed on internal damage density and types. However, damage levels correlated with neat resin behaviors under Contract NASI-12675 were assessed by C-scan ultrasonic methods and represent damage area measurements with no consideration of internal damage states.

4.2 RESIN DEFORMATION ANALYSIS

In general, the materials submitted for this analysis fall into two broad categories: those that can support plastic deformation on the microscopic scale and those that cannot. This delineation applies only to the resin matrix and not to the fibers. There is no evidence on any fracture surface from any specimen that the fibers have undergone plastic strain before failure, and all further references to plastic deformation pertain to the resin phase only. However, this does not mean that nonelastic fracture processes, such as fiber pullout, have not occurred.

4.2.1 Neat Resin Versus Composite Fracture: Cycom 937

Because of the difficulty of interpreting cross-fiber composite fractures, it may be instructive to examine some simpler cases before attempting an analysis of the various composites. The fractures shown in Figures 7 through 14 are from compact tension fracture-toughness (K_{IC}) specimens manufactured from neat resins and loaded in tension. Two comparative photographs are shown in Figures 7 and 8. These are SEM photographs of fracture origins and propagation zones of unreinforced Narmco 5208 and Cycom 937, respectively.

Narmco 5208 (fig. 7) is a tetraglycidylmethylenedianiline (TGMDA)-diaminodiphenylsulfone (DDS), 177°C (350°F) curing epoxy with good high-temperature properties, low strain to failure, and brittle fracture behavior. This brittle behavior is manifested in the smooth, glassy cleavage planes found in the fracture face, as well as the well-defined origin zones and transverse cleavage planes perpendicular to the direction of crack propagation. Figure 7 describes the classically brittle case, and the features seen at low magnification continue as increasing magnification is used (figs. 9 and 10). There is little ductility in this material and no deliberate introduction of second-phase elastomer or elastomer modification of any kind.

Cycom 937 (fig. 8) is a highly elastomer-modified epoxy, using a different base resin, bisphenol-A, and several different elastomer additions. Because of these additions, Cycom 937 has a much lower T_g than Narmco 5208, 121°C (250°F) versus 177°C (350°F), even though both are cured at 177°C (350°F). The elastomeric modification gives Cycom 937 a much higher strain to failure and the ability to sustain some plastic flow before ultimate rupture. This is seen in the lack of a clearly defined origin zone and the absence of transverse cleavage planes found in Narmco 5208. These features are obliterated by the ductile flow of Cycom 937 prior to failure. In addition, much

lower magnifications must be used to define the origin position, since macroscopic order is quickly lost because of plastic deformation of the fracture surface (figs. 11 and 12).

The second-phase elastomer leaves a clearly recognizable feature when compared with the smooth surfaces of Figures 9 and 10. The small holes or pits are products of the deformation due to dilatational stress of the matrix around the lower modulus elastomer particles, which are tightly bonded to the parent matrix. Higher magnification shows these deformation pits in greater detail (figs. 13 and 14). The actual mechanism of elastomer-matrix interaction is not clear, but it is generally recognized that the pits are not the "holes where the rubber particles were." No mating surfaces with particles in them are ever found. It has been speculated that the remnants of the particles are stretched across the bottom of the pits. This would substantiate the contention that the elastomer particles are tightly bonded to the parent epoxy matrix and function in a manner similar to that of precipitates in precipitation-hardenable aluminum alloys.

Figures 15 through 19 are from the Cycom 937 graphite/epoxy laminate submitted for analysis by NASA and fractured completely using the ETI instrumented impact tester. These photographs were taken from the tension side of the fracture face, which is opposite the indenter impact surface. The photographs show, in increasing magnification, the large amounts of plastic deformation associated with this ductile matrix. This is particularly prevalent in Figure 17. Also seen in each photograph are several voids, whose presence is confirmed by the microsection. Curiously missing are the residual pits described earlier from the neat resin sample. Also, the appearance of brittle fracture ridges and hackles (ref 3) between individual fibers suggests that this mechanism may be somewhat suppressed by the presence of the fibers. However, it does occur to some extent, as can be seen in Figure 19. Figures 20, 21, and 22 are presented for comparison and show a fracture face generated by pulling a notched tension ± 45 -deg tape specimen composed of T300/Cycom 937 at 1.1 m/m/min. (in./in./min.) to static failure. Figures 20, 21, and 22 represent typical fracture features of initiation and propagation for the static failure case. Comparison of the tension impact fracture with the tension static failure shows that both fail via the same basic mechanism; the only differences seem to be the lack of deformation pits on the surface. This may be a function of the specimen fabrication, since the NASA specimen was cured per the manufacturer's recommendations and the tension specimen was cured per Boeing process specifications. This also may be a function of the

difference in deformation rates, since the higher rate would favor less deformation of the rate-sensitive elastomer particles.

Figures 23 through 26 are typical views of the compression side of the impacted specimen. As on the tension side, many voids are evident in the fractured resin, and there is a conspicuous lack of second-phase elastomer particle deformation pits.

The general appearance of both the tension and compression surfaces is similar in the impact specimen. Figures 15 through 18 and 23 through 26 were taken of the delamination planes in both cases. These planes experience a high shear stress during the impact event and, therefore, should exhibit fracture features similar to those of the ± 45 -deg notched tension specimen. This specimen also supports loads via a shear mechanism. Likewise, the overall delamination fracture surface character should be unlike that of the neat resin compact tension specimen and also should be unlike that of a 90-deg tape specimen loaded in tension. This is confirmed by comparing Figure 21 with Figures 27 and 28. The fact that the delamination fractures appear the same on both sides of the neutral axis leads to the conclusion that the delaminations found in the impact specimens are either initiated and propagated or simply propagated by shear, rather than by tension or mixed-mode loading.

4.2.2 Mechanism I: Air Logistics I

Air Logistics I, as mentioned previously, was the only specimen that was not found to delaminate when examined after the aluminum ball impact. Examination of the separated surfaces created by the ETI impact tester shows the typical macroscopic features found in Figures 29 and 30. These show very little splintering or discontinuous fracture of the individual plies, which is unlike standard aerospace materials such as Narmco 5208/T300. This indicates that Air Logistics resin has a very high strain to failure and that individual plies separate at points determined by the fibers, rather than by the matrix. A high strain to failure usually indicates an ability to support plastic deformation, and this ability is confirmed by examination of Figure 31, which shows large areas of resin in the center field that have sustained deformation on the order of 1 to 2 fiber diameters. Figure 32 is a higher magnification view of this resin deformation. Extreme elongation of strands of resin between plies has been sufficient to create a condition similar to microvoid coalescence in metals or crazing in thermoplastics such as acrylics. This type of deformation can be described as gross

molecular flow, and movements of atoms of this magnitude would require extremely large amounts of energy. These large required amounts of energy would give the material a very high fracture toughness in both mode I and mode II, which is reflected in the very small amount of cracking seen in the microsection and the apparently total lack of delamination.

This resin also exhibits good fiber-matrix bond strength, as seen in Figures 33 and 34. These photographs show a typical fiber from a pulled-out fracture artifact. The presence of a resin layer on the surface indicates that Air Logistics resin fails cohesively in the resin surrounding the fibers.

A typical low-magnification view of the compression side of the ETI-induced fracture is shown in Figure 35. This appearance is typical of compression fractures, with considerable damage done to fracture surfaces by the sliding of one surface over another after separation has occurred. It is interesting to note the consistency of the failures on a ply-by-ply basis, in that little pullout is evident.

A shear failure on the compression side is shown in Figure 36. As on the tension side, massive resin plastic flow has occurred in the material between the fibers and between the plies.

A transverse compression failure is shown in Figure 37, and another view of a compression shear interply fracture is shown in Figure 38. Examination of Figure 37 shows that resin deformation seems to be more restricted in the intraply regions and, in fact, is not substantially greater than in some of the more brittle systems. However, Figures 36 and 38 show that interlaminar resin regions are able to support high flow in a manner similar to the tension side.

Compression loading does not appear to create any type of fiber-matrix interfacial failures, as can be seen in Figures 39 and 40. These photographs confirm that under tension (figs. 33 and 34), shear (fig. 39), and compression (fig. 40), Air Logistics I exhibits cohesive matrix failure only.

4.2.3 Mechanism 2: Narmco 107

Narmco 107, like Air Logistics I, fails by a tension-dominated crack mechanism after impact. However, this material has somewhat larger delaminations in the interply spacing. Also like Air Logistics I, this resin is capable of tremendous plastic deformation during the impact process. This is clearly shown in Figures 41 through 44. These photographs show delamination planes on the tension bending side of the fractures. Significant aspects of these planes are the rough, blocky appearance of the fractured resin, the almost complete lack of an imprint from the next ply, and the hairy appearance of the deformed resin. This hairy texture could be an indication of alignment of elastomer chains in a manner similar to that of crazing in thermoplastic materials.

Resin-to-fiber bonding (fig. 45) in this system is quite good, with pulled-out fibers and those with cracks close to the outer fiber surfaces being covered with a thick coating of resin. This is especially well illustrated in Figure 46.

Compression and compression shear faces are shown at comparative magnifications in Figures 47 through 50. These photographs show that the shear deformations, compared to the tension side of the fractures, are caused by the same basic mechanism and produce the same type of fracture appearance. The transply deformations, when viewed in a broken 90-deg ply, show characteristic compression features on the macroscopic level. Figure 51 shows a rare patch of undamaged compression failure surface in the center-right side of the photograph. It is interesting to compare the area of well-defined hackles and the stretching of the broken resin in the area of nonsmeared fracture, to the far more typical appearance of the rest of the photograph. This smoother, flowed appearance is characteristic of neat resin composite compression failures and is a result of separated ply movement after crack formation. The direction of gross separated ply movement in this photograph is to the left, while the actual crack propagated to the right.

Figure 52 shows the hairy resin failure appearance first noted on the tension side. This feature is far more pronounced on the compression side and clearly shows the direction of plastic flow during the deformation process. These hairs are shown in higher magnification in Figure 53, which also shows the roots extruded from the base resin into a filament and, in some cases, bridging a gap between two large blocks of resin.

This additional elastomeric elongation mechanism may explain the apparent toughness of Narmco 107.

4.2.4 Mechanism 2: Ciba 4

Ciba 4 shares the impact fracture mechanism of Narmco 107, which is tension-dominated mixed mode. However, significant differences between the two appear upon examination of the fracture surfaces. Narmco 107 exhibits considerable ductile flow in tension, compression, and shear, with ductile tearing and fibrillation being the ultimate separation mechanism. Ciba 4, on the other hand, shows approximately the same impact resistance when viewed via microsection, but shows brittle fracture with cleavage as the ultimate separation mechanism. This is evident when Figures 41, 42, and 54 are compared. Ciba 4 shows the imprint of the overlapping ply and a brittle cleavage failure of the interlaminar resin, while Narmco 107 shows only deformed resin with only a trace of the overlapping plies.

Figures 55 and 56 show higher magnification views of this brittle deformation in two separate areas. For comparison, Figures 57 and 58 show typical shear failures of a brittle resin system, Narmco 5208, in a graphite composite manufactured using tape in a ± 45 -deg layup and failed in tension. Note the similarity of resin fracture features between the fibers of Figures 57 and 58 and the resin fracture of Figures 55 and 56. Recognition must be given to the scale of the features. The brittle cleavage formations of Ciba 4 are much larger and do show some slight rounding, indicating that limited plastic deformation has occurred. This would be expected, since the photomicrographs suggest that Ciba 4 is considerably tougher, based on apparent impact damage, than Narmco 5208.

Resin tension fracture, viewed from a transverse crack in a tension-loaded 90-deg ply, is shown in Figures 59 and 60. As in the case of the shear appearance, the ultimate separation mechanism is cleavage. However, plastic flow of the bulk materials appears to have occurred before separation. This is evident when Figures 59 and 60 are compared to Figures 61 and 62, a 90-deg tension failure of Narmco 5208. Care must be taken when making comparisons due to the different magnifications, but the similarity of features is evident.

Fiber-matrix bonding is quite good in Ciba 4. The high magnification necessary to view fiber-matrix interaction also is necessary to resolve indications of plastic deformation and second resin addition. The small bumps on the fibers shown in Figures 63 and 64 are similar to those seen in Air Logistics 1, and the intersections of the cleavage planes have stretched and thinned resin streamers, characteristic of necked and failed material.

Figures 64, 65, and 66 are photographs of interlaminar shear faces from the compression end of the specimen. Comparison with Figures 55 and 56 shows that the mechanism of shear deformation is uniform across the specimen.

4.2.5 Mechanism 3: Ciba IM

Figures 67 and 68 show tension intraply failure of $0/\pm 45$ -deg plies in Ciba IM. Ciba IM has been determined to fail by fracture mechanism 3, which is shear-dominated mixed-mode cracking. This mode, and the specimens falling into it, exhibited the most damage as measured by visual evaluation of the polished microstructures. This category includes the two industry standard 177°C (350°F) curing materials, Narmco 5208 and Hercules 3501-5A.

The microstructure suggests that the resin of Ciba IM is brittle, with little ability to support plastic flow. However, this is not found to be true when examining the fracture surfaces of the separated pieces. Figures 69 through 72 show tension-side delamination faces after impact. While the basic mechanism appears to be cleavage, the ends of the cleaved features are rounded and feathered, indicating that some plastic flow has occurred before separation of the two planes. Figures 73 and 74 show a topography typical of one side of the delamination plane; the other side is shown in Figures 75 and 76. The planes in Figures 73 through 76 show fracture close to the fiber surfaces, as if the delamination crack paralleled the fiber plane. Figures 73 through 76, therefore, show the surface of the resin residing in the interlaminar spacing, and evidence of plastic deformation is much more obvious. Of particular interest is the imprint of the overlapping ply in the upper center of Figure 75. Note that the pulled-out fiber track curves, indicating bulk resin flow.

Fiber-matrix bonding is very good in Ciba IM. Figure 72 shows a tension failure at a point removed from the fiber-matrix interface, indicating that the cracking is

cohesive, rather than adhesive. This condition is typical of the fibers found on the fracture surfaces. The rounded shapes could be caused either by dilatational stress via the same mechanism as found in Cycom 937, or by the collapse of crazes formed by the thermoplastic addition to the bisphenol-A base resin (ref 4).

Figure 73 shows delamination planes on the compression side of the specimen, as well as a compression-loaded, \pm 45-deg ply and a pulled-out tension-loaded crossply. The interface shown was at the neutral axis of the impact-loaded specimen and had only shear loading. A higher magnification view is shown in Figure 74. The light spots on the photograph are an artifact of the photographic process. The fracture features on these planes are similar to those of the delamination faces on the tension side, but are much less distinct. Also, considerable secondary cracking out of the photograph plane has occurred, penetrating into the underlying area of the fibers. It is not clear whether such secondary cracks emanated from or penetrated into the exposed delamination surface. However, the relatively regular spacing of these transverse tension cracks suggests that they propagated into the exposed delamination surface. Figures 75 and 76 show higher magnification views of some similar planes. Figure 76 also shows the influence of voids on the fracture, since the crack has separated several voids in this photograph. The voids do not act as origins for the fracture, but simply function as free surfaces. As such, they would artificially lower the fracture toughness, because no energy would be required during cracking to create the void surface.

4.2.6 Mechanism 3: Hexcel I

Hexcel I, when examined microstructurally, shows impact damage extensive enough to be considered a mechanism 3 fracture. Because the damage in both transverse tension and interlaminar modes is extensive, the expected fracture features should be brittle and typical of low-toughness materials. This does not coincide with the overall chemistry (table 1), from which a natural assumption of high toughness would be made. It also does not agree with the appearance of the separated faces, as shown in Figures 77 and 78. Figure 77 shows a delamination face of a \pm 45/0-deg interface with considerable transverse cracking in the 0-deg ply. Higher magnification views, Figures 78, 79, and 80, show that considerable ductility of the resin has occurred and that small pits similar to those of the Cycom 937 pure resin sample are present. It is not clear that these pits are due to the same mechanism that operates in Cycom 937,

because the microstructure of Hexcel I has considerable porosity, visible even at the low magnification used for microstructural analysis. While the $2.5 \times 10^{-1} \mu\text{m}$ voids would not be visible at the low magnifications used for optical microscopy, the presence of the large voids suggests the possibility that the pits may in fact be voids.

A fact that supports the elastomeric inclusion theory is the consistency of the pit diameters. It is unlikely that such an even void distribution would occur during cure, and the sizes of the voids sectioned by the cracks would be expected to vary widely.

The pit size distribution remains narrow throughout the specimen, as can be seen by comparing Figures 79 and 80 with Figures 81 and 82, which are photographs of a corresponding shear plane from the compression side of the specimen and exhibit the same pitted appearance. The pits conform to the plastic flow directions of the base resin, which supports the supposition that the pits are voids, or at least were created before the ultimate separation of the fracture faces.

The ductility of the base resin is obvious from Figures 78 through 84. Figure 84 shows resin elongation on the order of $10 \mu\text{m}$ at $5000X$, which is conspicuously absent in the case of the nonductile systems.

Fiber-matrix bonding of Hexcel I seems to be adequate for the impact case. This is shown in Figures 79 and 81. The conditions shown in these photographs are typical of the entire fracture appearance.

4.2.7 Mechanism 3: Cycom 919

Mechanism 3 also was determined to be active in Cycom 919 resin. This specimen showed severe delamination on all planes of the specimen and transverse tension cracking in all plies, including the uppermost. Therefore, Cycom 919 is similar to Hexcel I, with respect to the microstructure and its evaluation. It also is based on bisphenol-A and was processed at 121°C (250°F).

Cycom 919 appears to fail in a brittle fracture mode when viewed at low magnification, as shown in Figure 85. Figure 86 is at higher magnification and is still dominated by a brittle appearance. However, small patches in the center have the hairy appearance of Narmco 107, discussed earlier. A higher magnification photograph of

this feature is shown in Figure 87. This magnification reveals the fact that plastic deformation of the resin does occur in this material. This deformation is similar to that of several other specimens used in this study and consists of stretching and feathering of the hackles formed by the intersection of opposing cleavage facets. Several different areas are shown in Figures 88 and 89.

Fiber-matrix bonding is adequate in Cycom 919, as shown in Figures 90, 91, and 92. The fiber surfaces shown in this figure are coated with a thin layer of resin, some of which is plastically deformed.

4.2.8 Effect of Resin Content: BP-907 and BP-907-LR

Fracture features of American Cyanamid BP-907 and the effect of resin content on impact properties are revealed by the simultaneous analysis of specimens BP-907 and BP-907-LR (low resin). Examination of the microstructures reveals that BP-907 fails by mechanism 2, tension-dominated mixed mode, while BP-907-LR fails by mechanism 4, predominantly shear. This is not an unexpected result, because the interlaminar spacing would be the area most affected by a reduction in resin content. Variations in resin content are manifested as either thicker or thinner interlaminar areas. A thick interlaminar spacing allows more expansion of the plastic zone at the tip of an interlaminar crack, which then would incorporate more material in the plastic deformation processes at the crack tip. Low resin content, therefore, would reduce the amount of plastic deformation, producing a lower fracture toughness. In addition, voids caused by a low resin condition would tend to migrate to the interlaminar boundary, thereby reducing the fracture toughness of this region by the creation of free surfaces.

Fracture features of the compression side are very similar to those of the tension-loaded plies. These are shown in Figures 93 through 96. The only differences detected are a somewhat greater amount of plastic deformation at cleavage apices, and a slightly thicker resin coating on somewhat exposed fibers.

The presence of voids on the shear planes is shown in Figures 93 and 94. The greater number of voids is clearly evident in Figure 94. As in previously discussed specimens, the voids do not act as crack initiators, but serve as free surfaces.

Higher magnification views of voids and void-free surfaces are shown in Figures 95 and 96. The amount of plastic deformation is much greater in the material with higher resin content. This trend continues with the higher magnification views (figs. 97 and 98). These photographs graphically show the different extent of deformation created by the presence of additional resin.

The basic microscopic fracture mechanism appears to be the same in both the high- and low-resin-content materials. This conclusion is based on comparison of the two photographs in Figures 99 and 100. However, the fact that insufficient material may be available for the complete operation of this fracture mechanism may impair its efficiency as a toughening agent, as shown by Figures 101 and 102. The elongation of the resin under stress is clearly shown by Figure 102; but the formation of the large, deformed bodies seems to require the presence of greater amounts of resin. This would be manifested in an apparent increase of impact toughness, since the energy required to deform greater amounts of resin would necessarily be higher than that required for a lesser amount of the same resin.

Figures 101 and 102 also show that the interface properties of BP-907 are not affected by resin content and that complete wetting of the fibers occurs despite the lower resin content of BP-907-LR.

The differences in apparent ductility also extend to the compression-loaded interfaces. This is seen in Figures 103 through 108. These photographs show, as on the tension side, that the same deformation mechanism applies to the entire specimen, but that the lower resin content reduces the material available for this mechanism to act on. This would result in a lower apparent toughness for the materials with lower resin content.

4.2.9 Mechanism 4: Narmco X1114

Narmco X1114 appears to fail by mechanism 4, shear delamination. Examination of the microstructure shows that while cracking is confined almost exclusively to the interlaminar planes, it is not extensive in length and occurs on nearly every ply interface. The short length and through-thickness multiplicity of cracks suggest that the material may have a high interlaminar fracture toughness with respect to crack propagation, but that the energy required to initiate cracking in the matrix phase is

low. Analysis of these delaminations would be expected to show considerable plastic deformation of the fracture faces.

Considerable plastic flow is indeed found upon examination of the separated surfaces. This deformation is shown in Figures 109 through 114. These photographs, particularly Figures 111 through 114, show that there is virtually no brittle fracture or cleavage on the fracture planes. All of the resin shows an almost gummy appearance, as if capable of extreme strain. The fact that this composite has a Tg of only 46°C (114°F) may be a factor in this extreme plastic flow. Figure 114 shows that bonding to the fibers is extremely good for this system, and Figure 113 shows that even tension fiber failure does not translate into a failure of the surrounding resin.

Compression-side shear faces are similar to the tension faces at low magnification, as shown in Figure 115. Figures 116 through 121 are at higher magnification and show an additional mode not found in the tension delaminations. While compression-side shear planes also support the large degree of plastic flow found in the tension faces, a feature similar to that of Hexcel I also is found. This feature is especially prominent in Figures 118 through 121. It should be noted, however, that the microstructural view of Narmco X1114 did not show the large amount of porosity that was evident in the case of Hexcel I. Therefore, it seems unlikely that the porous, spongy appearance of this resin is due to voids. Another similarity between the two specimens is that both have the same base resin, bisphenol-A. However, several other specimens, such as BP-907, also have bisphenol-A as a base and do not exhibit this topography. This leaves the additives and second resins as causative agents for this mechanism of deformation. No information is available to show a link between these materials and the deformation process, so the actual cause of this fracture structure remains unclear.

4.2.10 Mechanism 4: Fibredux 920

Fibredux 920, like Narmco X1114, fails by predominant shear along interlaminar planes. However, the microstructure of Fibredux 920 reveals that the delaminations are of significantly longer length in this material than in Narmco X1114. Also, the Tg is nearly 32°C (89°F) higher in Fibredux 920. It also should be noted that the base resin is again the same, bisphenol-A, and that the generic chemistry is identical to that of Ciba 4, which was determined to fail by mechanism 2.

A typical delamination from the tension side of this material is shown in Figure 122. As in the case of the other mechanism 4 materials, this photograph shows considerable plastic deformation on the fracture face in the form of elongated resin blocks. Also present on the fracture plane is a significant amount of porosity, which is not visible in the microstructure.

Figures 123 and 124 show this delamination surface at higher magnification. Figure 123 reveals that there are few, if any, fracture details that would suggest any kind of brittle fracture or cleavage and shows that this resin apparently fails by ductile tearing only. However, Figure 124 shows a crack propagating through the resin after a tension fiber failure, indicating that this material will support crack propagation under the proper conditions. The fiber-matrix bond also is revealed in this photograph, and it is significant that the crack propagates exclusively through the resin, and not along the interface. Figure 125 is a similar photograph taken from the other side of the specimen and shows a similar appearance, in that the bare fiber surface is not exposed. Figures 126 and 127 should be compared to Figures 122 and 123, respectively. These figures show good agreement with respect to the fracture topography and confirm that the shear mechanism operating in the interlaminar spacing of this material is consistent throughout the thickness.

5.0 CONCLUSIONS

As revealed by cross-sectional microscopic inspection, composite materials subjected to impact characteristically fracture by some combination of tension intraply cracking and shear-induced delamination.

Impact fracture characteristics can be significantly altered through changes in resin chemistry, as illustrated by comparing the internal damage states of Air Logistics I with those of Narmco 5208. More specifically, examination of impact damage levels and types sustained by all 26 resin formulations reveals four discernible impact mechanisms. Based on the relative levels of tension intraply cracking and shear-induced delamination, the four mechanisms are as follows:

- Tension, no delamination
- Tension and shear, tension dominated
- Tension and shear, shear dominated
- Shear, small amounts of tension

Comparison of these four qualitative fracture mechanism categories with neat resin characterization work performed under NASA Contract NASI-12675 (ref 1) reveals no readily definable correlation with resin modulus, strain, or ultimate strength. This lack of correlation agrees well with internal Boeing studies (ref 2), which have repeatedly demonstrated that neat resin properties do not correlate with either composite impact resistance or interlaminar fracture toughness.

Comparison of impact damage characteristics with the approximate generic chemistries provided, as well as with recommended cure cycles, reveals little if any discernible correlation. Neither low cure temperature nor the simple addition of elastomers was found to guarantee improved impact resistance.

Impact damage characteristics were found to correlate qualitatively with measured glass transition temperatures. In general, low glass transition temperatures produced damage types with pronounced intraply tension cracking, while higher glass transition temperatures produced a wide variety of damage types exhibiting both extensive transply cracking and shear-induced delamination. However, despite this qualitative correlation, no relationship existed when comparing glass transition temperatures with residual impact load capabilities.

Scanning electron microscopic examination of impact-induced fracture surfaces revealed significant changes in resin deformation mechanisms with variations in resin chemistry. In general, observed deformation mechanisms fell into three categories: (1) brittle fracture with cleavage lines, (2) ductile fracture with high matrix resin elongation, and (3) two-phase combinations of brittle fracture and matrix ductility characterized by deformation pits or localized matrix fibrillation. Evidence of ductility of either the matrix resin or localized phase regions was found in all cases where improved impact resistance was observed. However, the same conditions of matrix ductility were not found to necessarily guarantee improved impact resistance, as demonstrated by examination of Hexcel 1.

Although voids were found on numerous separated fracture surfaces, no evidence was found to suggest that voids act as crack initiators during impact loading.

Scanning electron microscopic characterization of ETI impact-separated fracture surfaces revealed no discontinuities or changes in propagation mode from 107 m/s (350 ft/s) impact zones to ETI 1.5 m/s (4.9 ft/s) impact zones.

Resin content can significantly affect fracture mechanisms and fractographic features, based on both optical and scanning electron microscopic inspection of BP-907. Reductions in resin content produced more shear-induced delamination and reduced levels of overall plastic deformation. However, little difference, if any, was detected in the actual deformation mechanism itself, two-phase deformation pits.

APPENDIX—SPECIMEN CROSS SECTIONS

ORIGINAL PAGE
BLACK AND WHITE PHOTOGRAPH

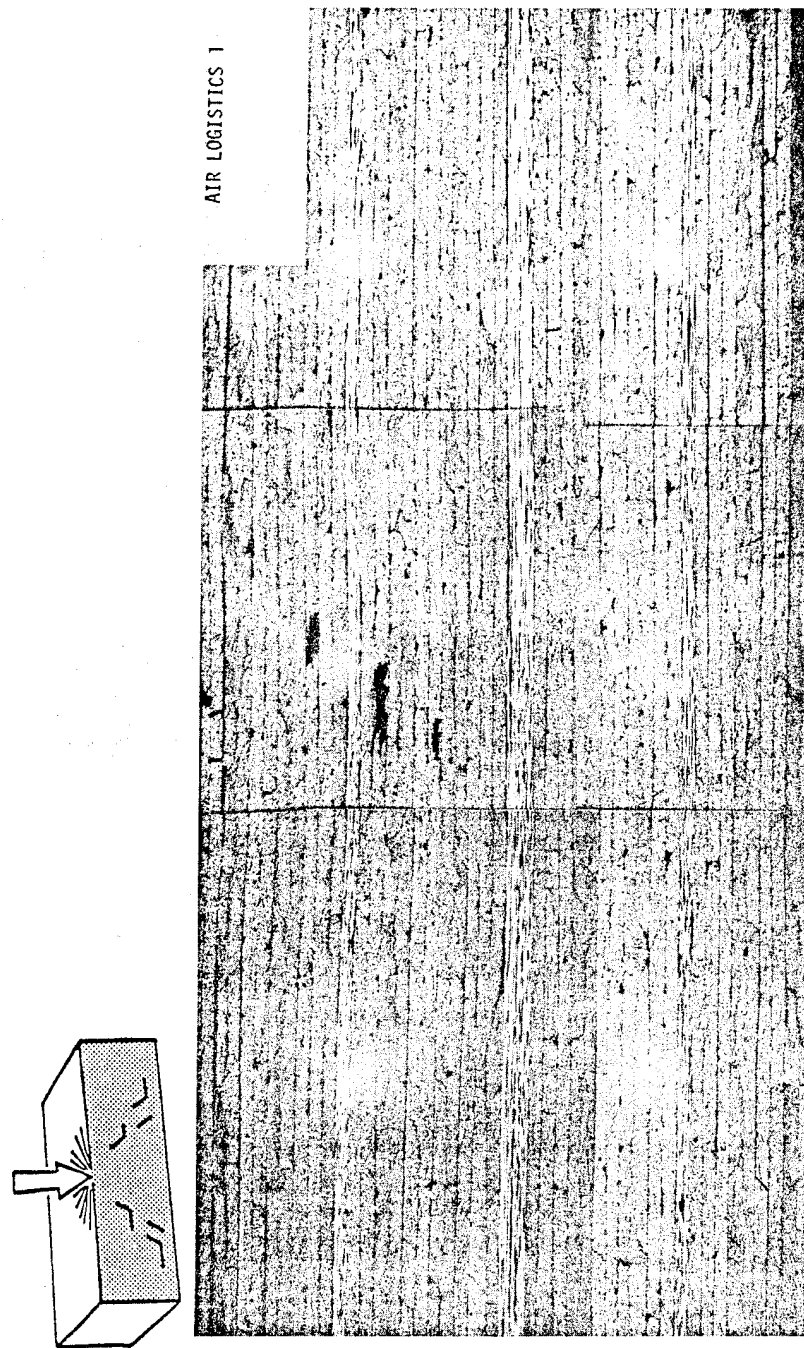


Figure A-1. Air Logistics 1

ORIGINAL PAGE
BLACK AND WHITE PHOTOGRAPH



Figure A.2. BP-907

ORIGINAL PAGE
BLACK AND WHITE PHOTOGRAPH



Figure A-3. BP-907-LR

ORIGINAL PAGE
BLACK AND WHITE PHOTOGRAPH

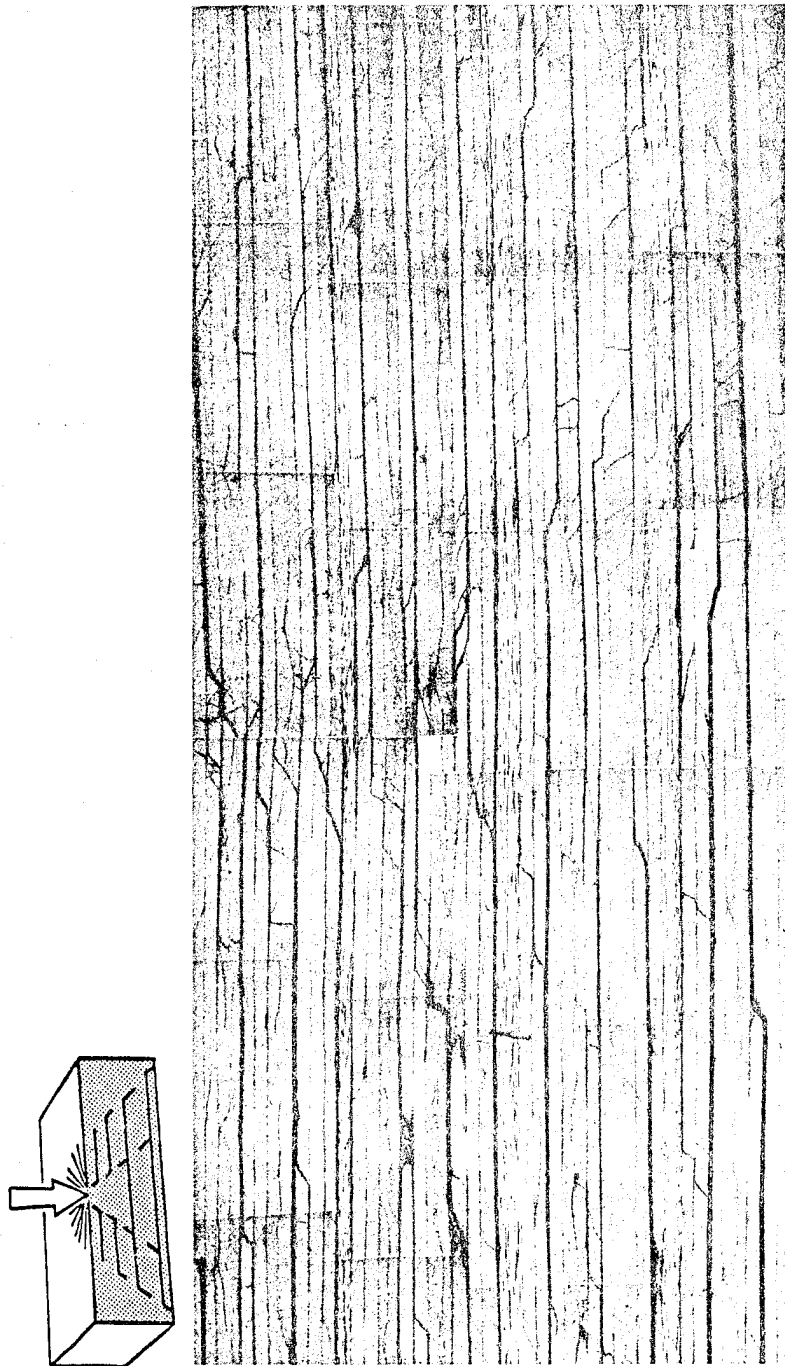


Figure A-4. Ciba 1

ORIGINAL PAGE
BLACK AND WHITE PHOTOGRAPH

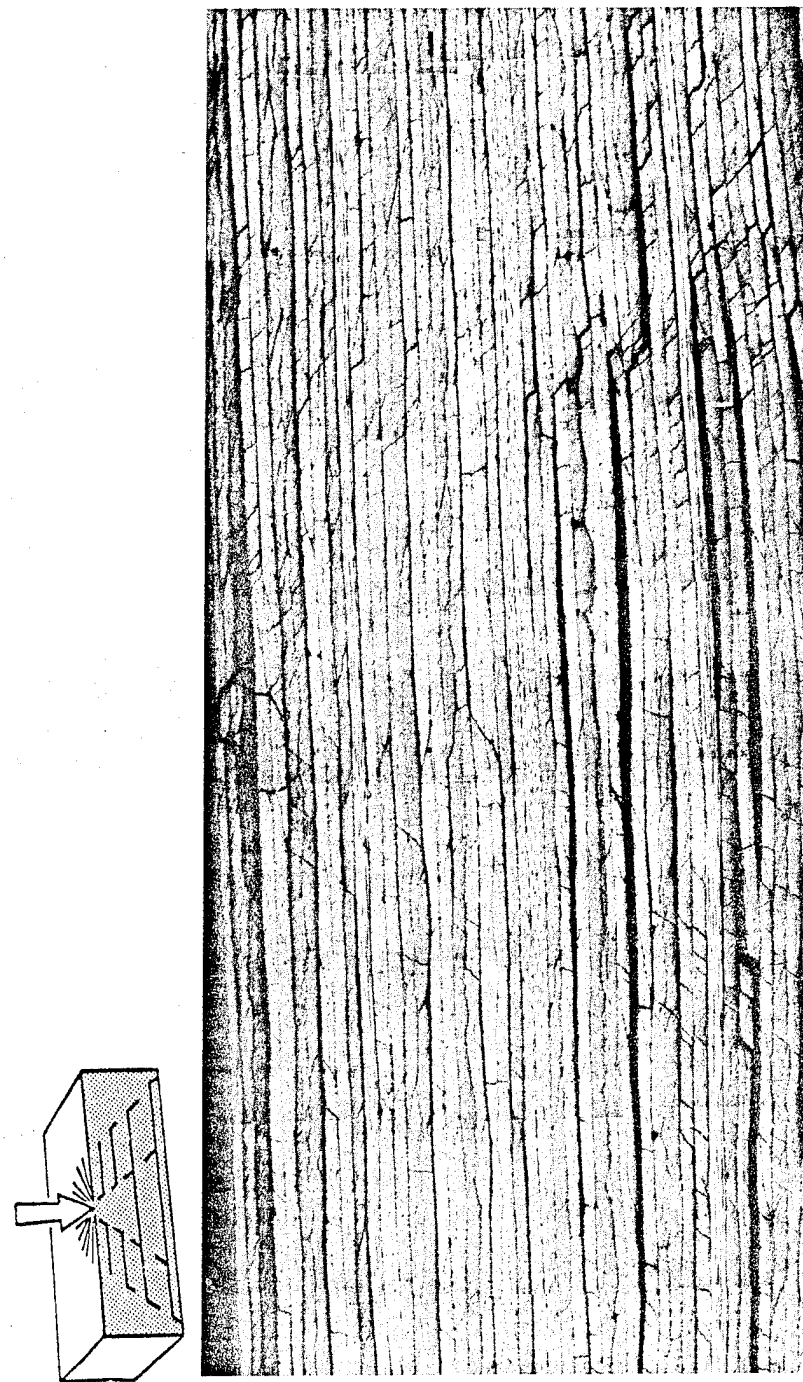


Figure A-5. Ciba 1M

ORIGINAL PAGE
BLACK AND WHITE PHOTOGRAPH



Figure A-6. Ciba 2

ORIGINAL PAGE
BLACK AND WHITE PHOTOGRAPH

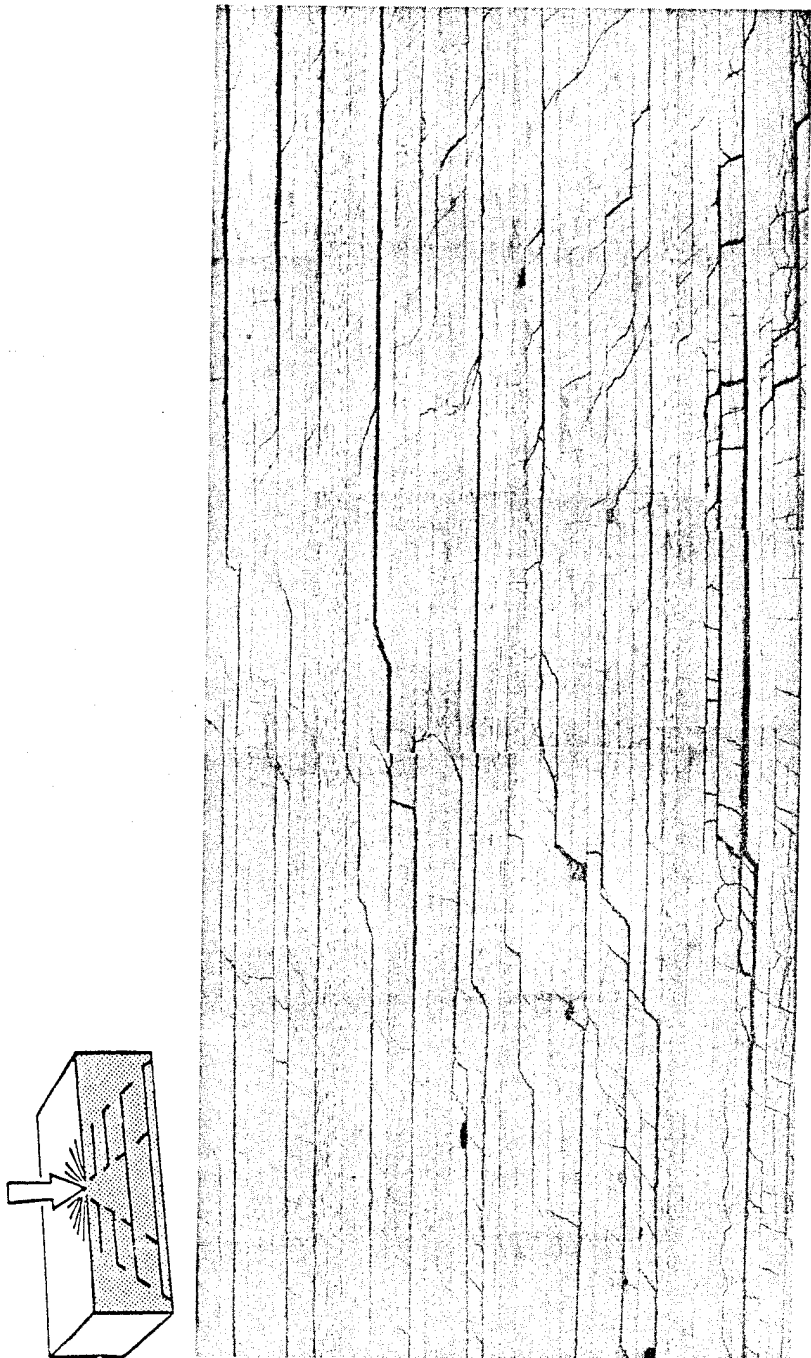


Figure A-7. Ciba 3

ORIGINAL PAGE
BLACK AND WHITE PHOTOGRAPH

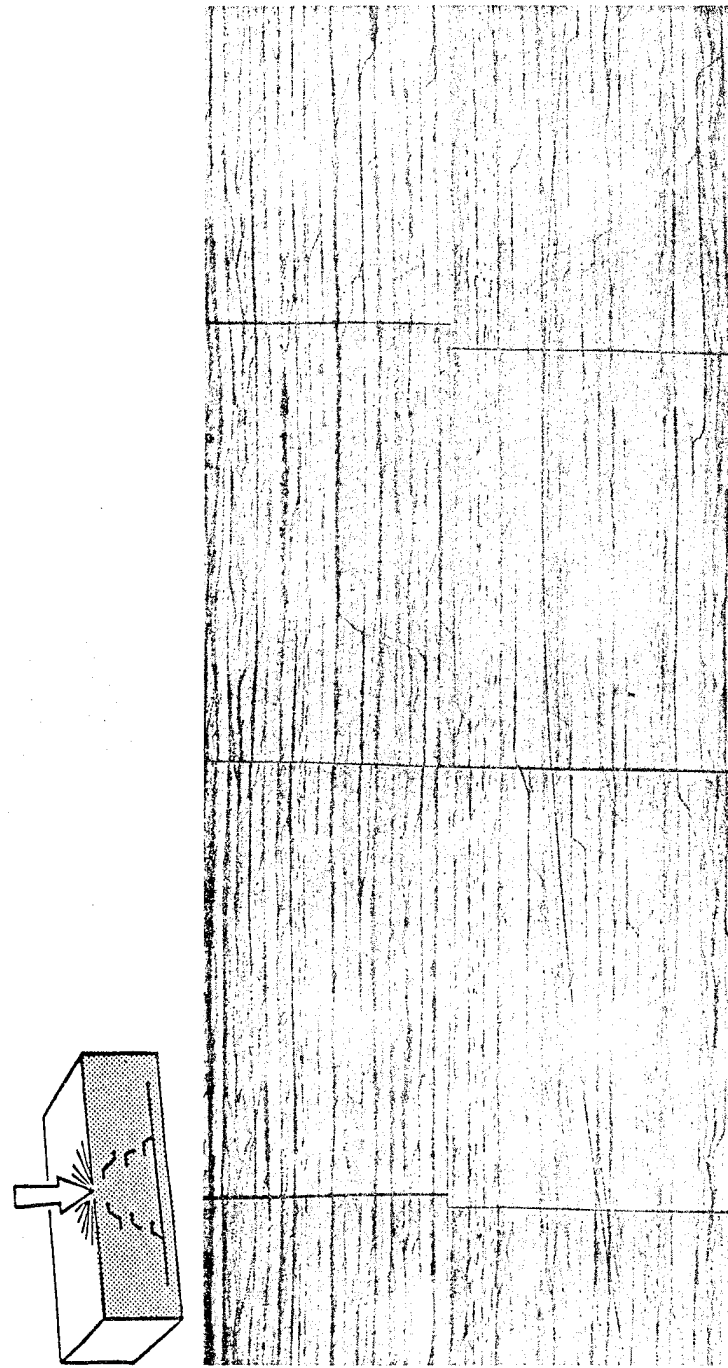


Figure A-8. Ciba 4

ORIGINAL PAGE
BLACK AND WHITE PHOTOGRAPH



Figure A-9. Cycom 919

ORIGINAL PAGE
BLACK AND WHITE PHOTOGRAPH

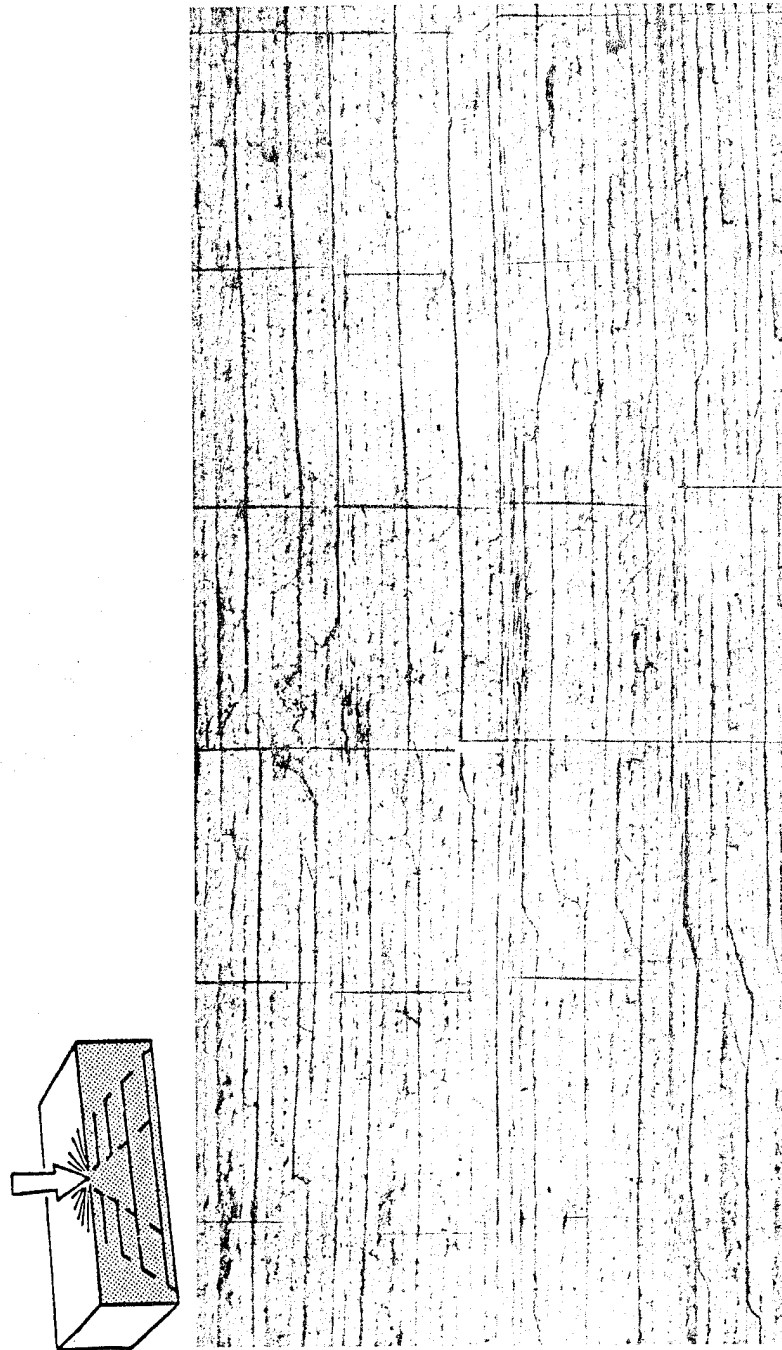


Figure A-10. Cyccon 937

ORIGINAL PAGE
BLACK AND WHITE PHOTOGRAPH

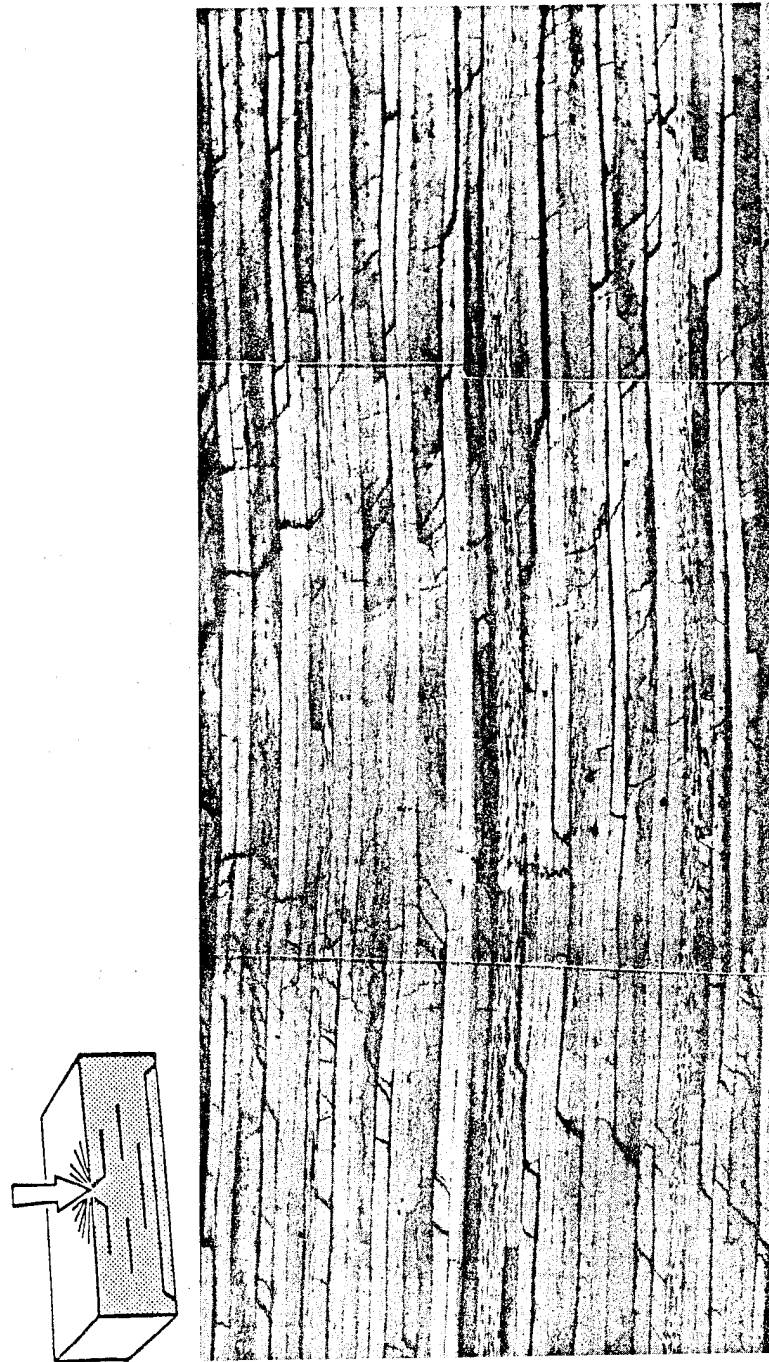


Figure A-11. Cycom 982

ORIGINAL PAGE
BLACK AND WHITE PHOTOGRAPH

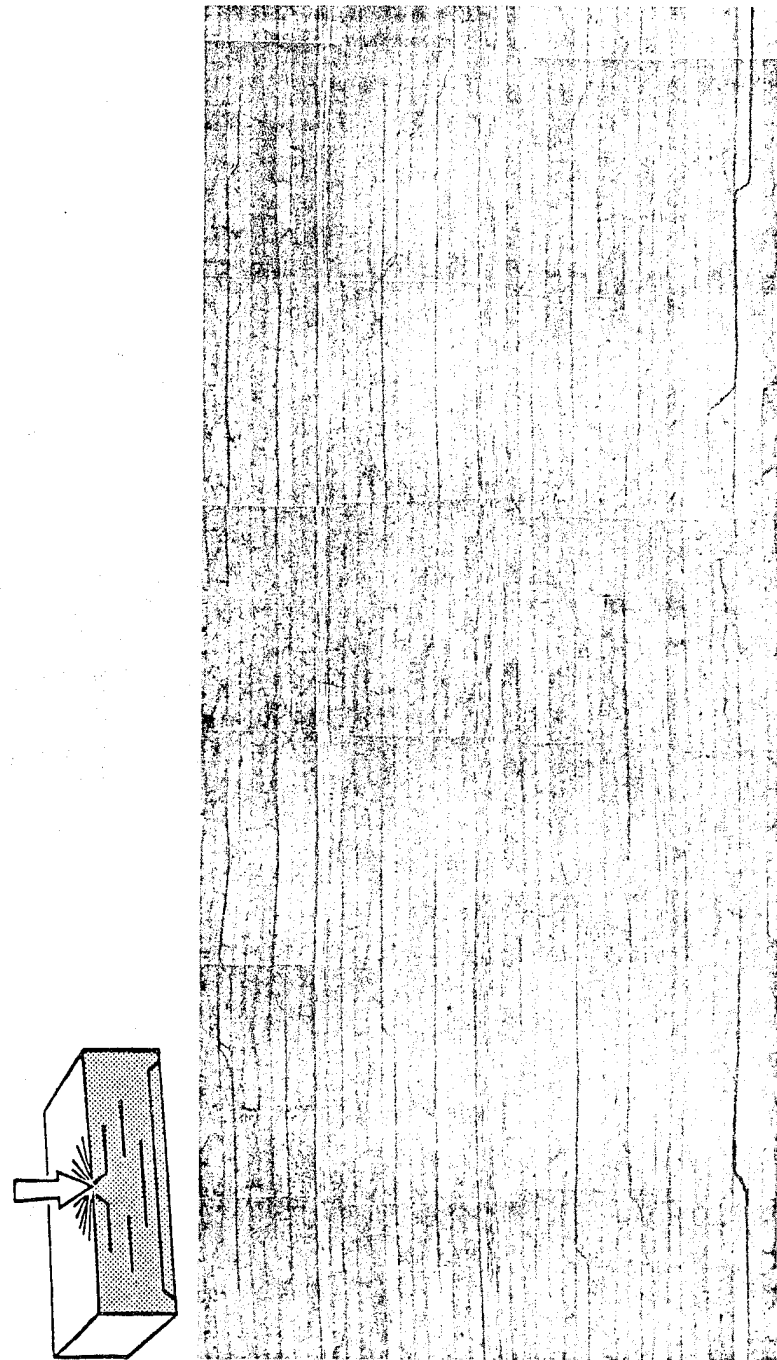


Figure A-12. Fibreddux 920

ORIGINAL PAGE
BLACK AND WHITE PHOTOGRAPH

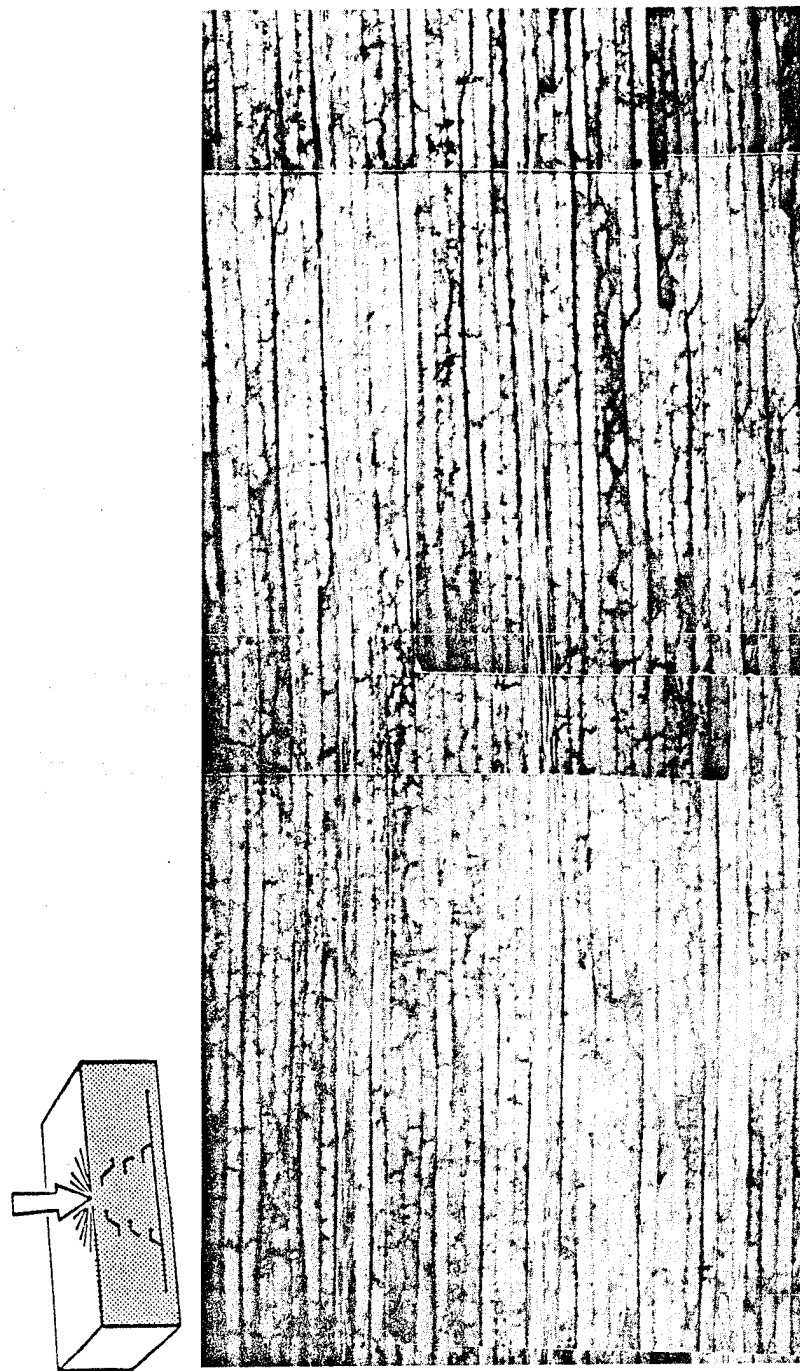


Figure A-13. Fibredux 920/AS4

ORIGINAL PAGE
BLACK AND WHITE PHOTOGRAPH

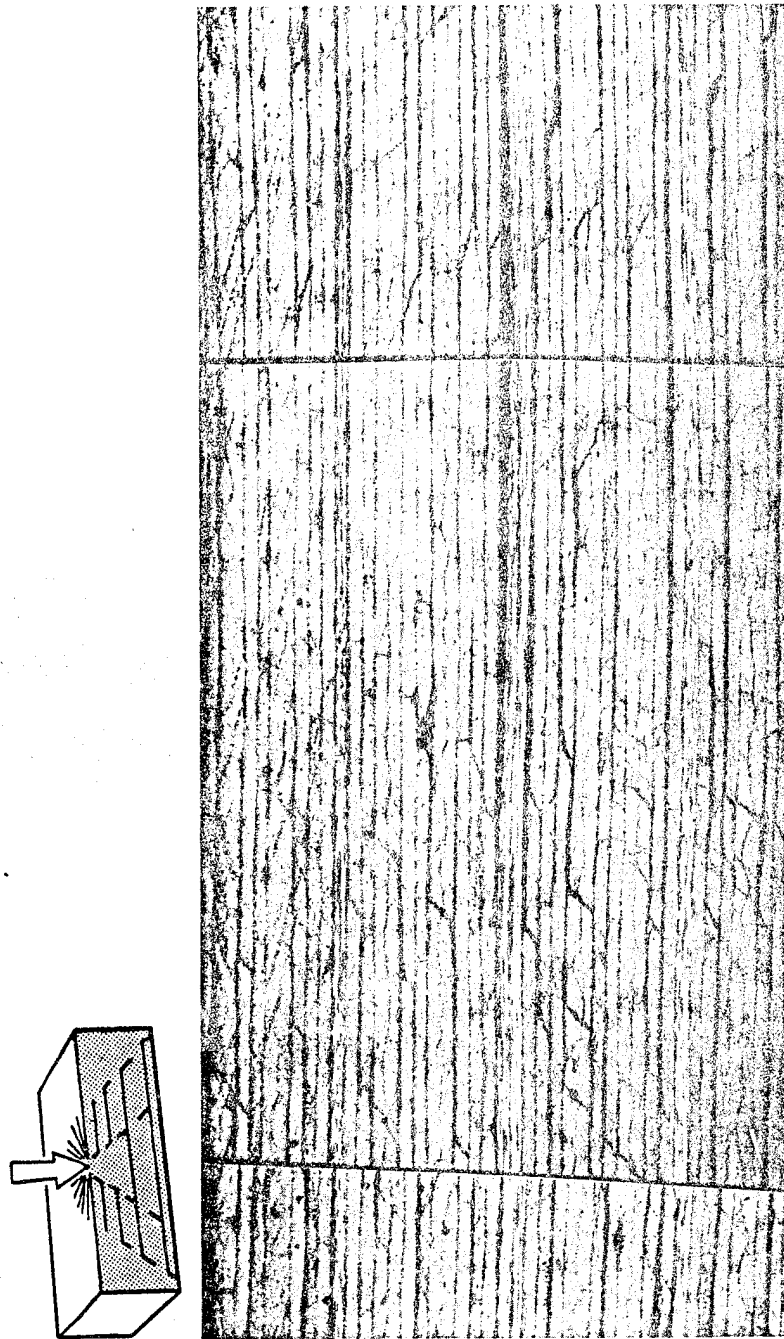


Figure A-14. Hercules 3501-6/AS4

ORIGINAL PAGE
BLACK AND WHITE PHOTOGRAPH

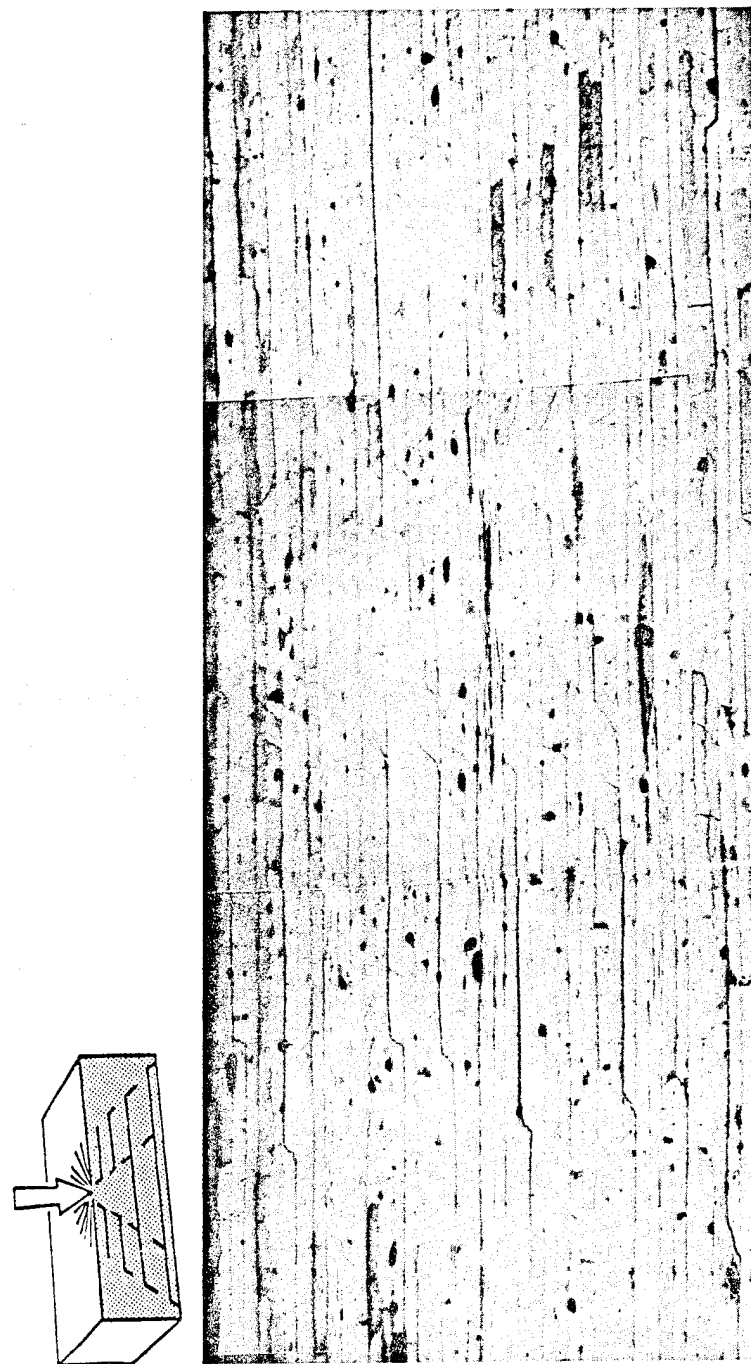


Figure A-15. Hexcel 1

ORIGINAL PAGE
BLACK AND WHITE PHOTOGRAPH

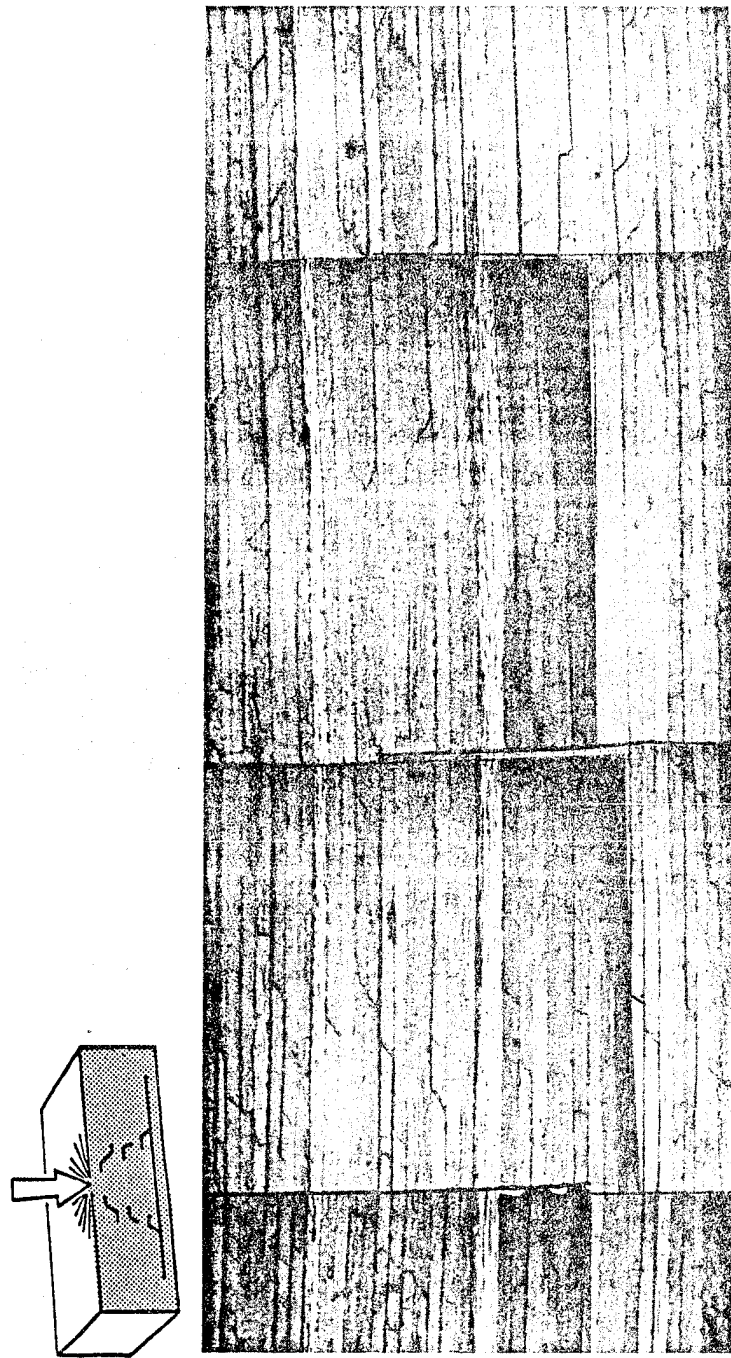
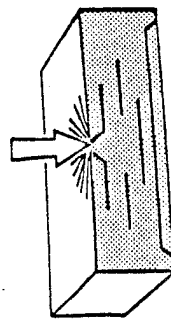


Figure A-16. Hexcel 2

ORIGINAL PAGE
BLACK AND WHITE PHOTOGRAPH



Figure A-17. HYE 976



ORIGINAL PAGE
BLACK AND WHITE PHOTOGRAPH

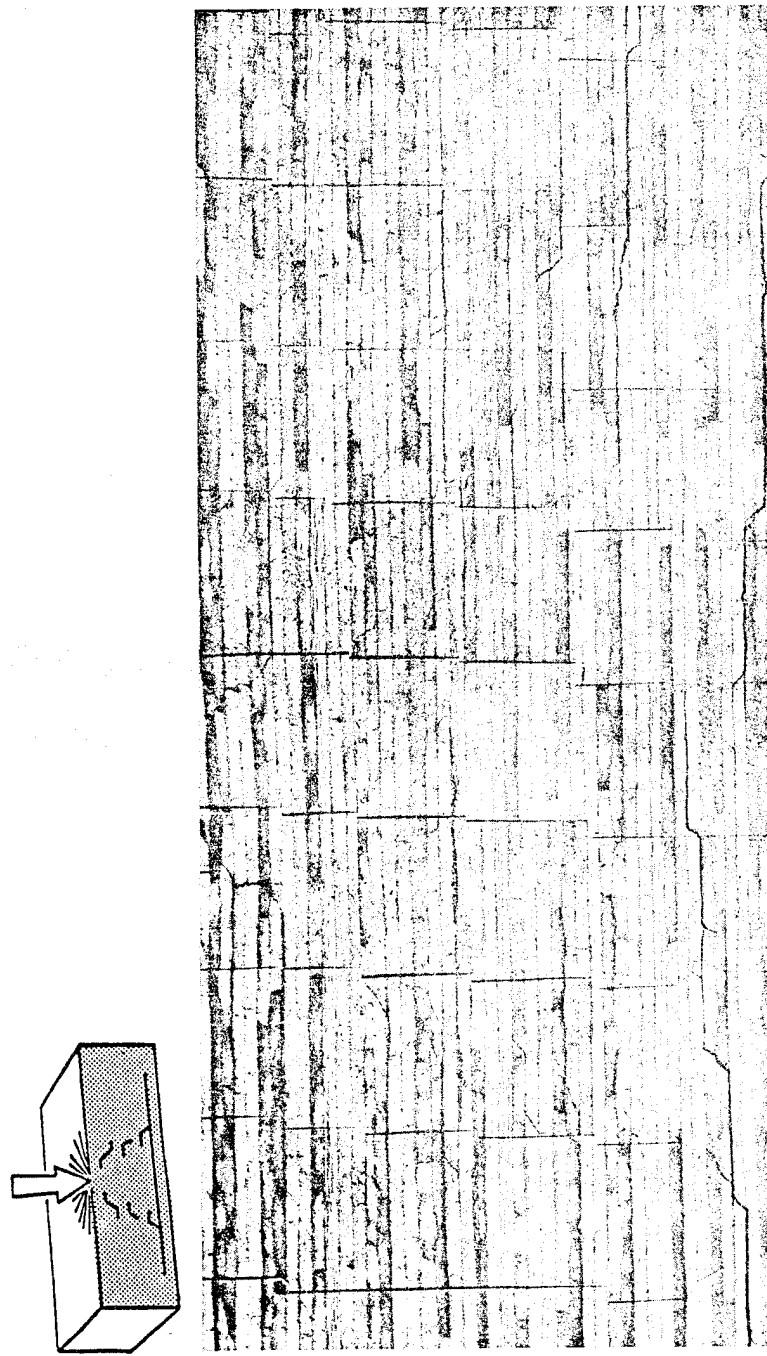


Figure A-18. Narmco 107

ORIGINAL PAGE
BLACK AND WHITE PHOTOGRAPH

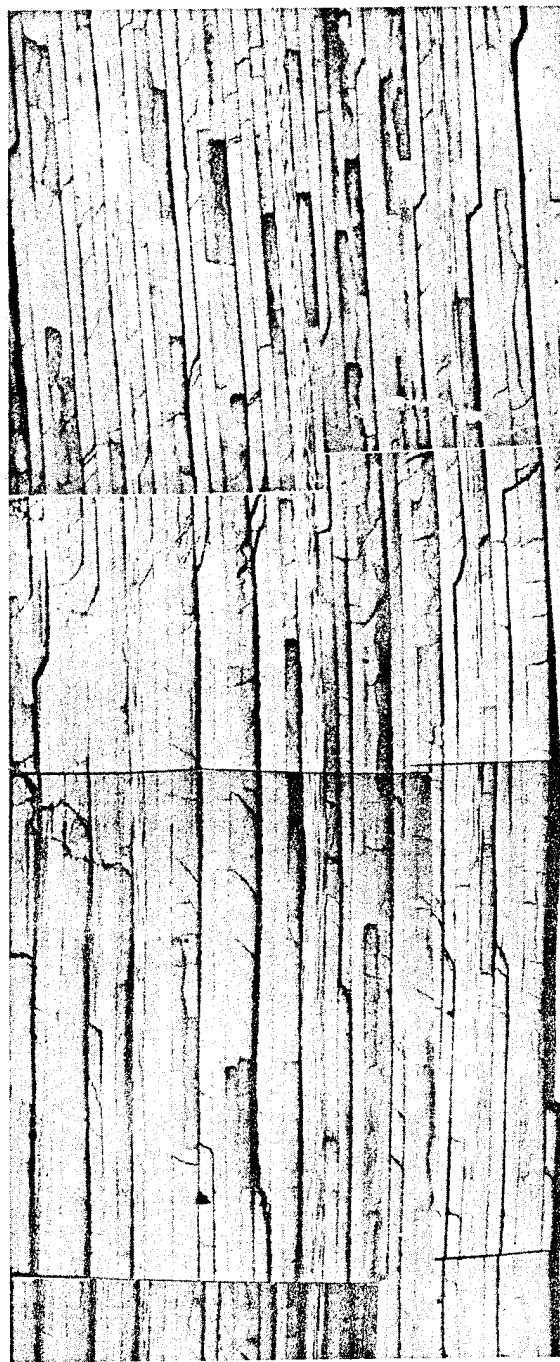
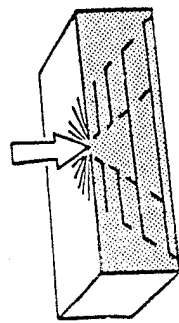


Figure A-19. Narmco X108

ORIGINAL PAGE
BLACK AND WHITE PHOTOGRAPH

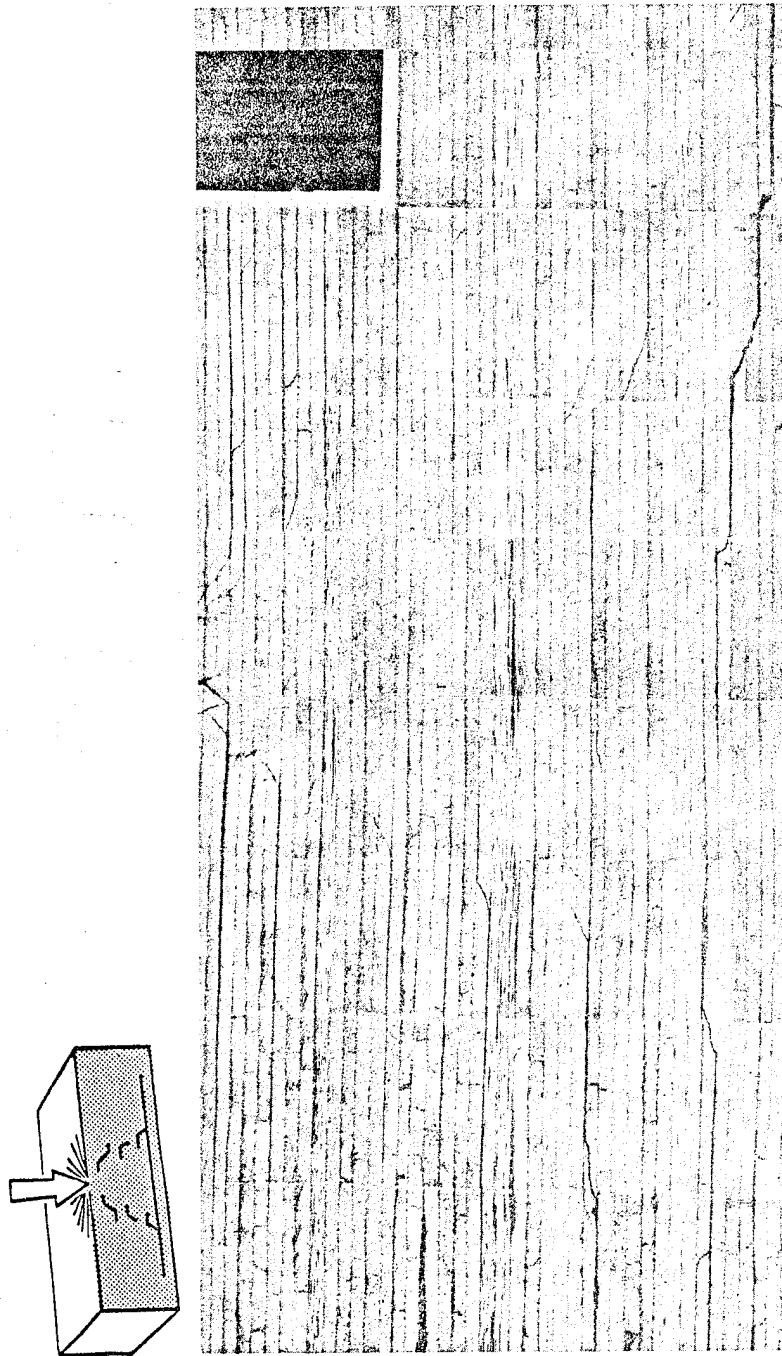


Figure A-20. Narmco X109

ORIGINAL PAGE
BLACK AND WHITE PHOTOGRAPH

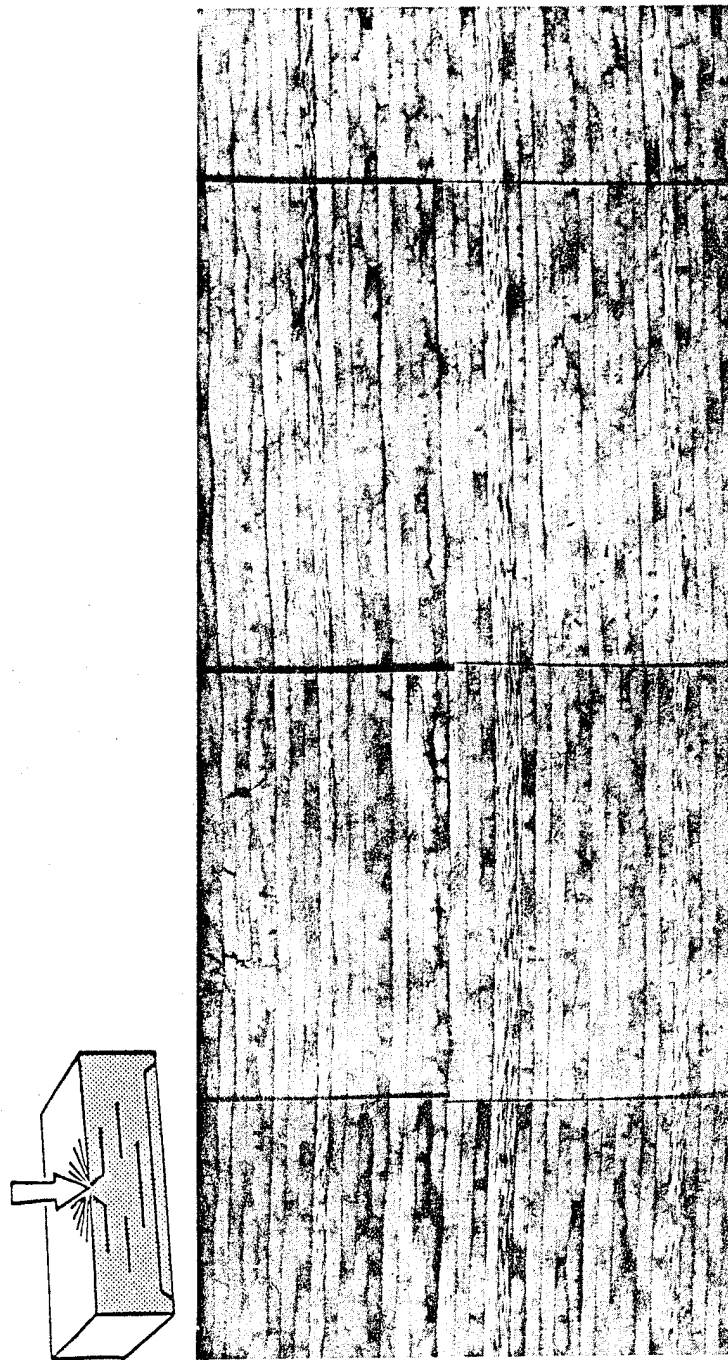


Figure A-21. Narmco X1114

ORIGINAL PAGE
BLACK AND WHITE PHOTOGRAPH

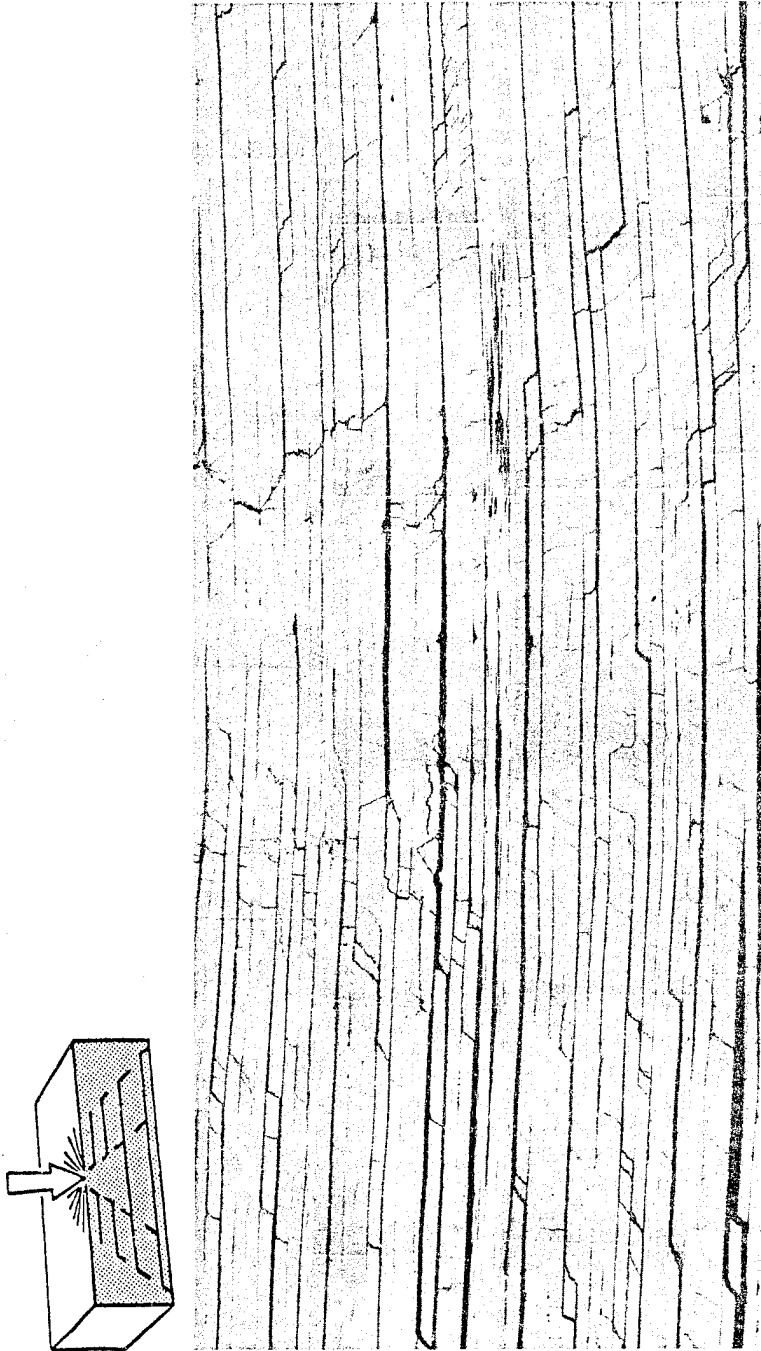


Figure A-22. Narmco 5208

ORIGINAL PAGE
BLACK AND WHITE PHOTOGRAPH

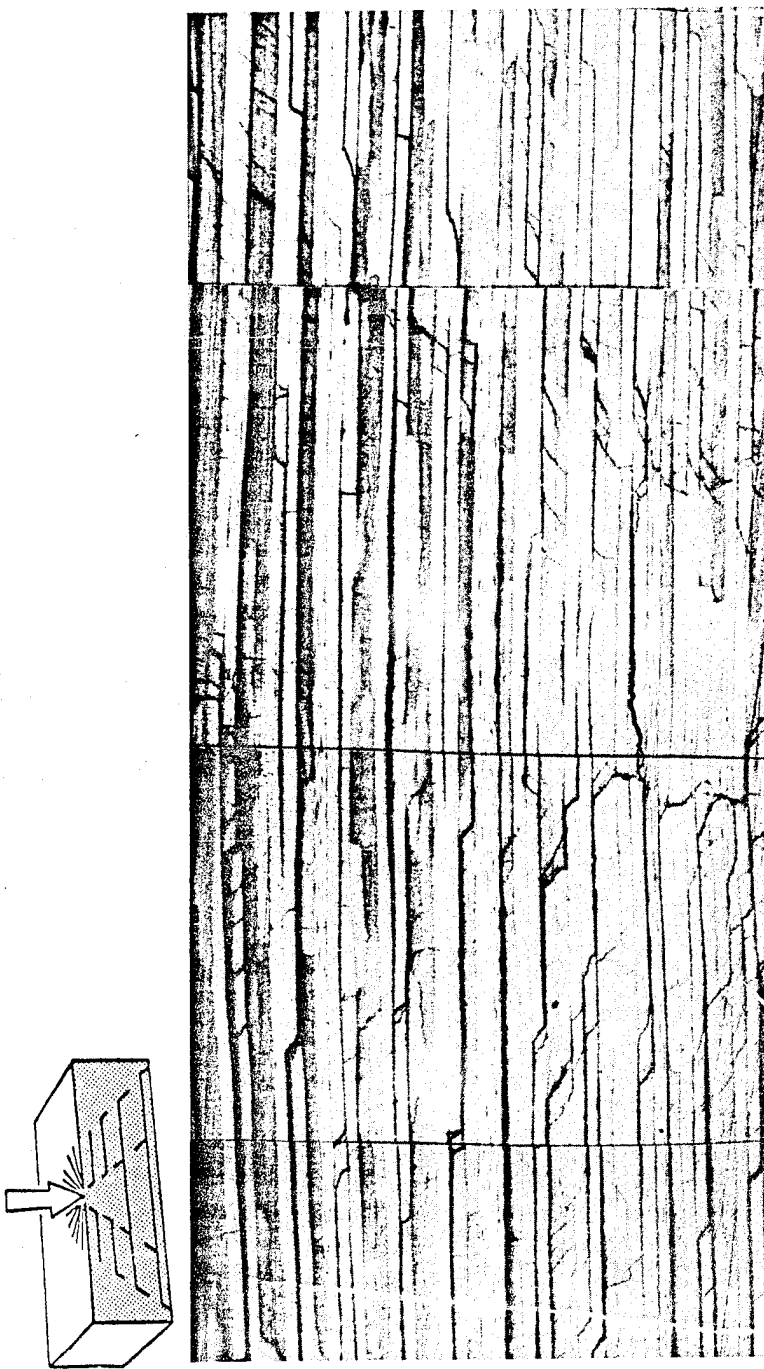


Figure A-23. Narmco 5208 (14-hr Cure)

ORIGINAL PAGE
BLACK AND WHITE PHOTOGRAPH

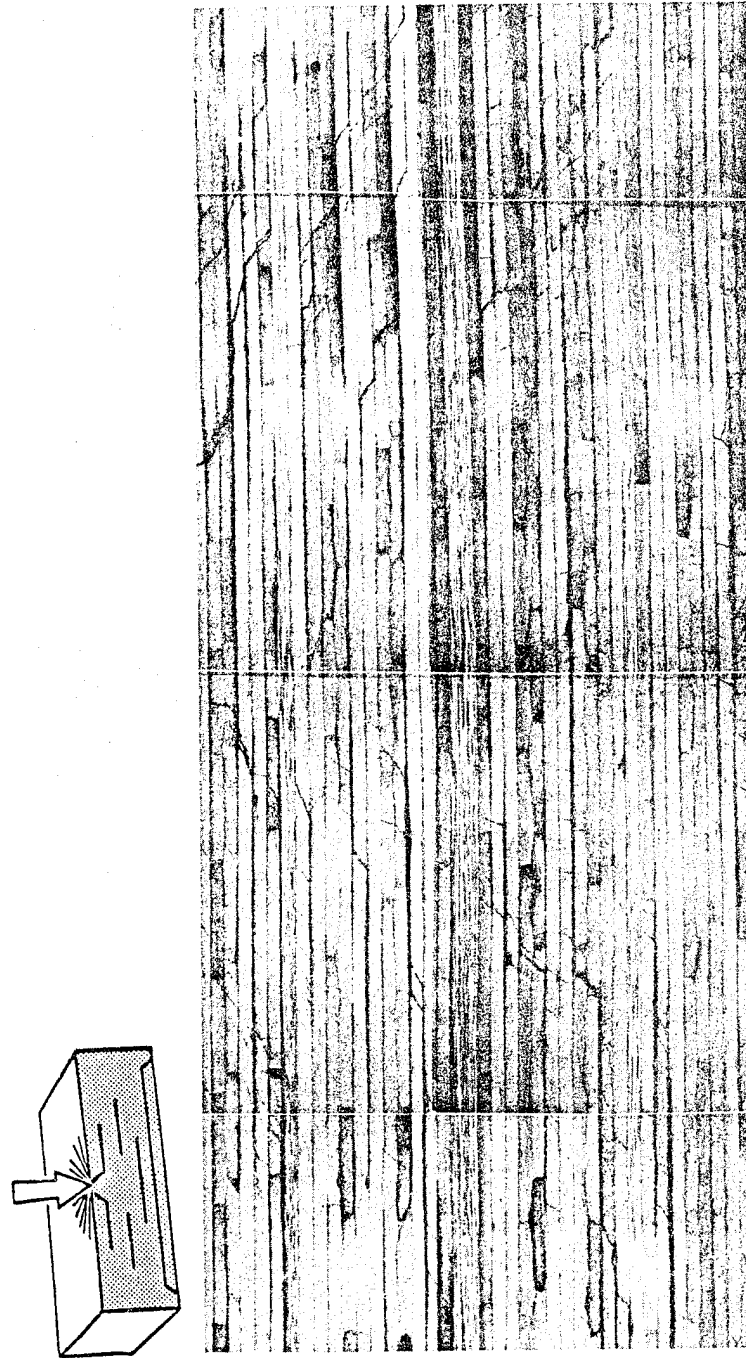


Figure A-24. Namco 5235

ORIGINAL PAGE
BLACK AND WHITE PHOTOGRAPH

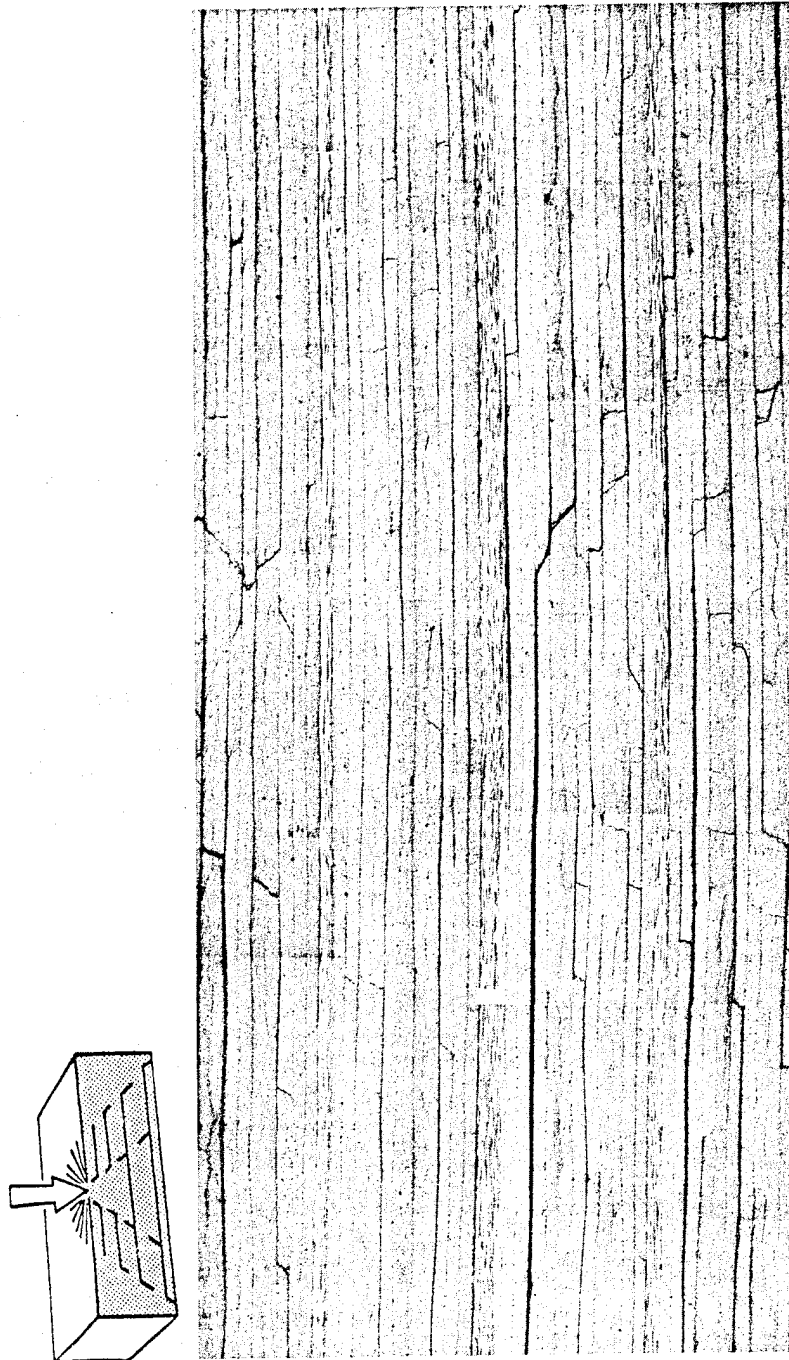


Figure A-25. U.S. Poly 1

ORIGINAL PAGE
BLACK AND WHITE PHOTOGRAPH

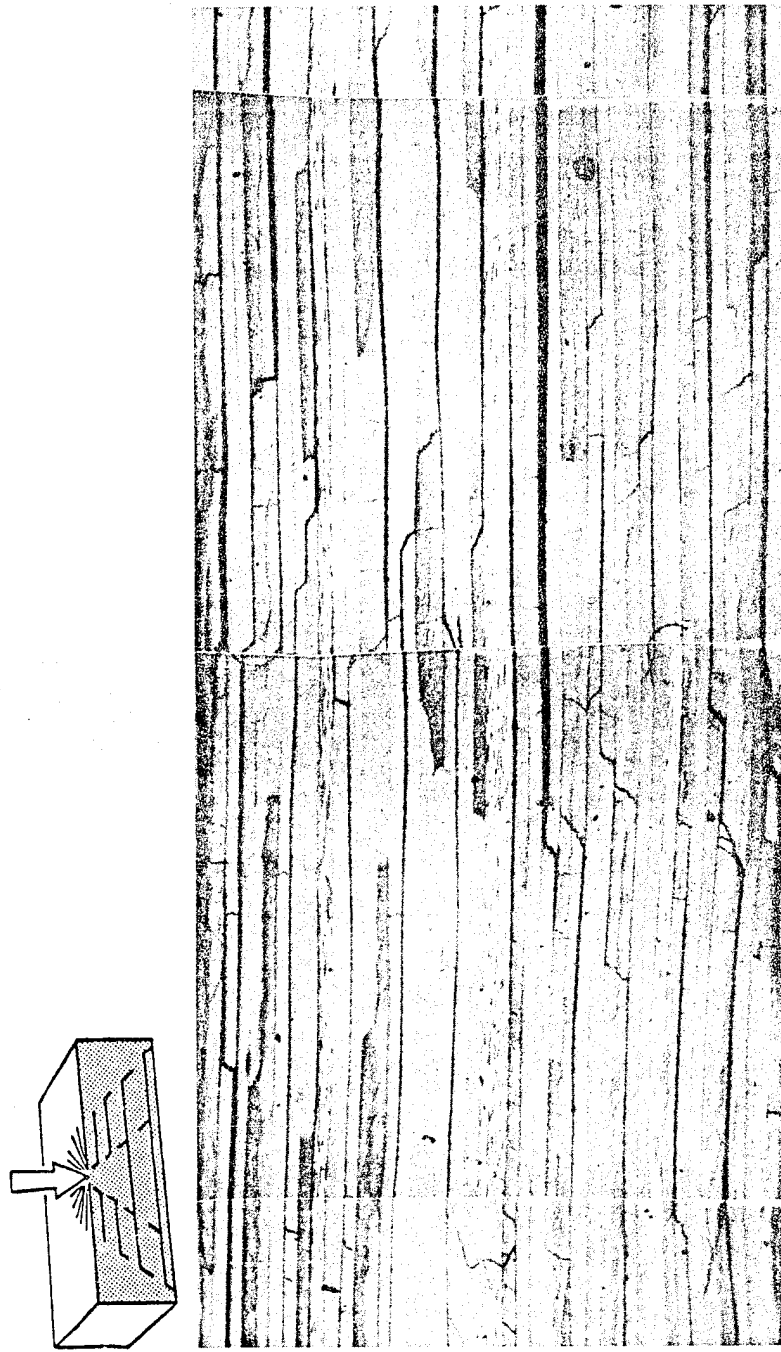


Figure A-26. U.S. Poly 2

REFERENCES

1. R. J. Palmer, "Investigation of the Effect of Resin Material on Impact Damage to Graphite/Epoxy Composites," Contract NASI-12675 Final Report, NASA CR-165677, March 1971.
2. A. G. Miller, P. E. Hertzberg, and V. W. Rantala, "Toughness Testing of Composite Materials," presented at SAMPE 12th National Technical Conference, October 1980.
3. G. E. Morris, "Determining Fracture Directions and Fracture Origins on Failed Graphite/Epoxy Surfaces," in Nondestructive Evaluation and Flaw Criticality for Composite Materials, ed. R. B. Pipes, American Society for Testing and Materials STP 696, 1979.
4. R. W. Hertzberg, Deformation and Fracture Mechanics of Engineering Materials, John Wiley and Sons, Inc., 1976.

Table 1. Specimen Generic Chemistry

Specimen	Cure temperature		Chemical composition before cure
	°C	°F	
Narmco 5208	177	350	MY720 aromatic amine
Hexcel 1	121	250	Bisphenol A—high-functionality epoxy catalyzed Di-Cy + elastomer
Hexcel 2	177	350	Bisphenol A and bisphenol F catalyzed Di-Cy + elastomer
Fibredux 920	121	250	Bisphenol A—aliphatic amine thermoplastic
HYE 976	177	350	High-functionality epoxy aromatic amine
Cycom 919	121	250	Bisphenol A—epoxy Novalac latent aliphatic amine elastomer
Cycom 937	177	350	Bisphenol A + specialty latent aromatic and aliphatic amines
Ciba 4	121	250	Bisphenol A—aliphatic amine thermoplastic
Ciba 3	177	350	Hydantoin—aromatic amine
Ciba 2	149	300	Hydantoin—aromatic amine
Ciba 1	177	350	Hydantoin—aromatic amine
Ciba 1M	177	350	Hydantoin—aromatic amine thermoplastic
BP-907	177	350	Bisphenol A—latent aliphatic amine vinyl resin
Air Logistics 1	149	300	Epoxy
U. S. Poly 1	177	350	Bisphenol A + specialty aromatic amine elastomer
U. S. Poly 2	149	300	Bisphenol A + specialty aromatic amine elastomer
Narmco X1114	121	250	Bisphenol A—nonaromatic amine elastomers
Narmco X109	177	350	Bisphenol A—nonaromatic amine elastomers
Narmco 107	177	350	Bisphenol A—nonaromatic amine elastomers
Narmco X108	177	350	Bisphenol A—aromatic amine elastomer
Narmco 5235	177	350	Epoxy + aromatic amine
Hercules 3501-5A/AS4	177	350	High-functionality epoxy aromatic amine

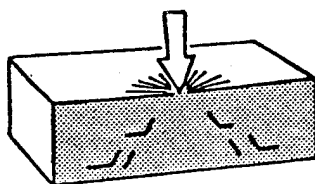
Table 2. Specimen Characteristics as Delivered

Specimen	Impact velocity		Cure temperature		Tg		Fracture mechanism
	m/s	ft/s	°C	°F	°C	°F	
Cycom 937	114.3	375	177	350	126.1	259.0	3
Narmco 5208	106.4	349	177	350	171.7	341.0	3
U. S. Poly 2	107.3	352	149	300	118.3	245.0	3
BP-907-LR (low resin)	105.2	345	177	350	101.4	214.5	4
Narmco X109	100.9	331	177	350	95.9	204.7	2
Fibredux 920/AS4	105.8	347	121	250	95.0	203.0	2
Narmco 107	103.6	340	177	350	114.3	237.7	2
Ciba 4	103.3	339	121	250	36.6	99.6	2
					49.2	120.6	
					62.2	144.0	
					75.3	167.6	
Ciba 3	107.9	354	121	250	88.1	190.5	3
Ciba 2	107.6	353	149	300	93.1	199.5	3
Ciba 1	107.9	354	177	350	123.6	254.5	3
Ciba 1M	108.8	357	177	350	117.8	244.0	3
Air Logistics 1	106.1	348	149	300	45.6	114.0	1
HYE 976	108.5	356	177	350	158.1	316.5	4
					210.6	411.0	
Hexcel 2	77.4	254	177	350	105.6	222.0	2
					134.4	274.0	
Hexcel 1	104.2	342	121	250	79.7	175.5	3
Cycom 919	108.5	356	177	350	160.6	321.0	3
Narmco X108	108.5	356	177	350	160.6	321.0	3
Narmco 5208 14-hr cure	108.2	355	177	350	176.7	350.0	3
Narmco 5235	87.8	288	177	350	195.8	384.5	4
Hercules 3501-6/AS4	105.8	347	177	350	162.8	325.0	3
BP-907	105.8	347	177	350	106.9	224.5	2
Narmco X1114	104.2	342	121	250	82.0	179.6	4
Cycom 982	109.7	360	177	350	177.8	352.0	4
U. S. Poly 1	105.2	345	177	350	54.2	129.5	3
Ciba Fibredux 920	108.2	355	121	250	98.1	208.5	4

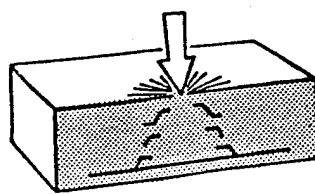
Table 3. Residual Impact Properties

Specimen	Thickness		Width		PI		PF	
	mm	in	mm	in	kg	lb	kg	lb
Ciba 3	6.6040	0.2600	25.019	0.985	243.1	536.0	295.9	652.3
Ciba 4	7.6962	0.3030	25.400	1.000	616.9	1360	323.9	714
U. S. Poly 1	6.2865	0.2475	25.273	0.995	345.2	761	115.2	254
U. S. Poly 2	5.9563	0.2345	25.019	0.985	174.6	385	223.2	492.1
Cycom 937	6.9469	0.2735	24.892	0.9800	469.5	1035	208.7	460
Cycom 919	6.7996	0.2677	24.511	0.9650	326.24	719.23	366.7	808.5
Hercules 6	6.1671	0.2428	25.146	0.9900	233.4	514.6	264.9	583.9
Narmco 107	8.1178	0.3196	25.400	1.000	438.6	966.9	538.4	1187
Narmco X108	6.3754	0.2517	25.400	1.000	175.57	387.07	201.1	443.3
Narmco X109	7.5184	0.2960	24.892	0.9800	494.0	1089	217.9	480.3
Narmco X1114	7.2288	0.2846	26.416	1.040	533.0	1175	425.2	937.5
Narmco 5235	7.7648	0.3057	25.400	1.000	526.2	1160	357.2	787.5
Hexcel 1	6.7310	0.2650	24.892	0.9800	467.7	1031	258.5	570
Hexcel 2	7.2390	0.2850	24.892	0.9800	416.6	918.5	248.1	546.9
Fibredux 920	6.3830	0.2513	24.765	0.9750	400.1	882	288.9	636.9
BP-907-LR	6.7615	0.2662	25.146	0.9900	487.2	1074	251.2	553.8
BP-907	7.8308	0.3083	25.400	1.000	453.6	1000	49.4	108.9
Narmco 5208 14-hr	6.2357	0.2455	24.892	0.9800	154.2	340	159.4	351.5
Ciba 920	7.1120	0.2800	—	—	349.3	770	379.2	835.9
Air Logistics 1	6.2992	0.2480	—	—	363.7	801.7	190.5	420

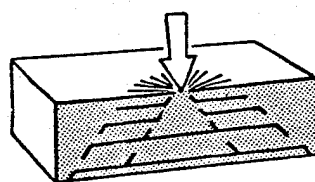
ORIGINAL PAGE IS
OF POOR QUALITY



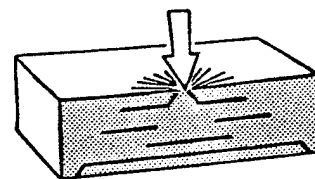
Mechanism 1: Tension, no delamination or shear



Mechanism 2: Tension and shear, tension dominated



Mechanism 3: Tension and shear, shear dominated



Mechanism 4: Shear, small amounts of tension

Figure 1. Fracture Mechanisms

OPTIONAL PAGE OF
OF POOR QUALITY

AMCY937 ○
NARM5208 □
USPOLY 2 ◇
BP 907LR ◁
NARMX109 △
FD920
NARM107
CIBA 4
CIBA 3
CIBA 2
CIBA 1
CIBA 1M
AIRLOG 1 ◀
HYE 976 □
HEXCEL 2 ▲
HEXCEL 1 ◇
AMCY919 △
NARMX108 □
5208 14H
NARM5239 □
HER350
BP 907
NARMX111
CYCOM982
USPOLY 1 ◁
CIBA FD920 ◁

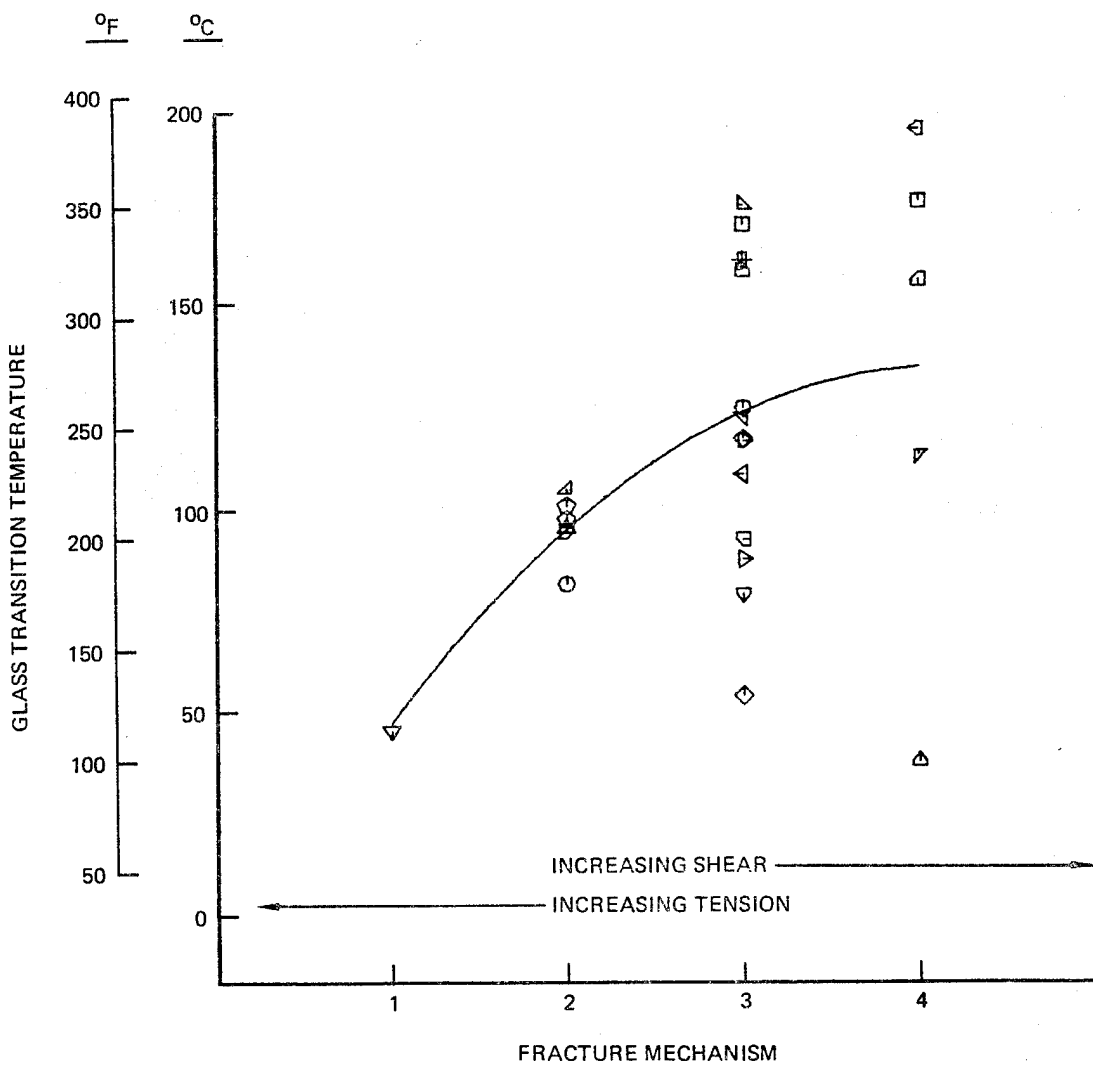


Figure 2. Fracture Mechanism Versus Glass Transition Temperature, As-Received Specimens

ORIGINAL PAGE IS
OF POOR QUALITY

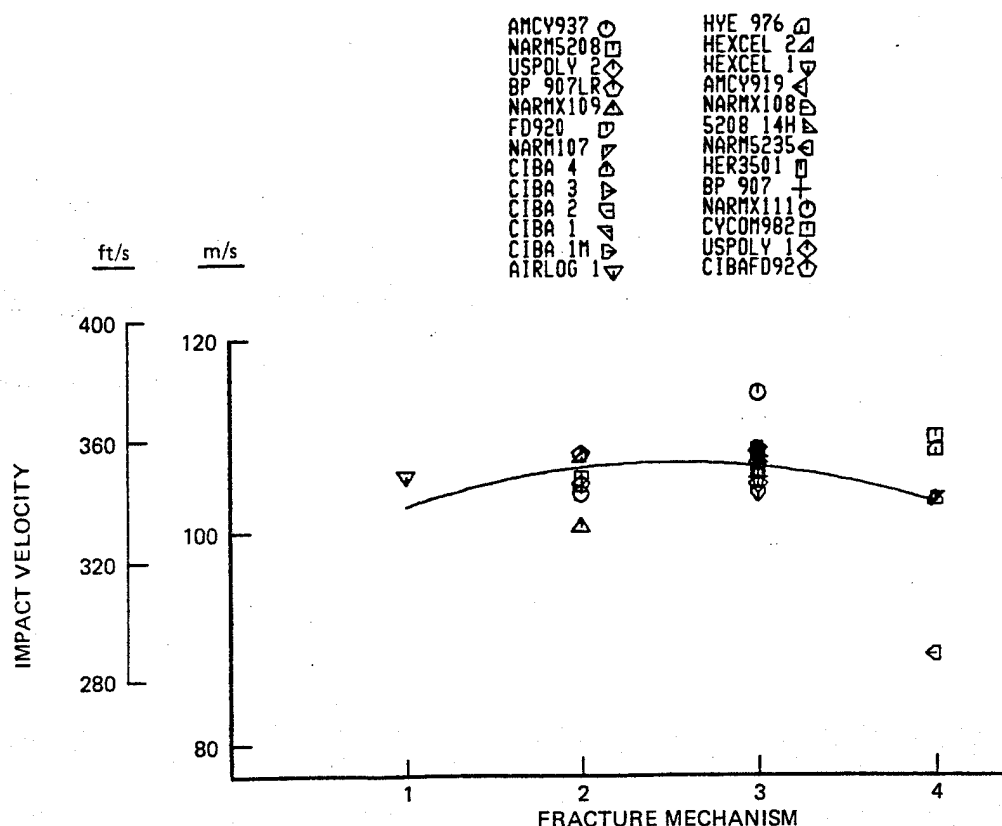


Figure 3. Fracture Mechanism Versus Impact Velocity, As-Received Specimens

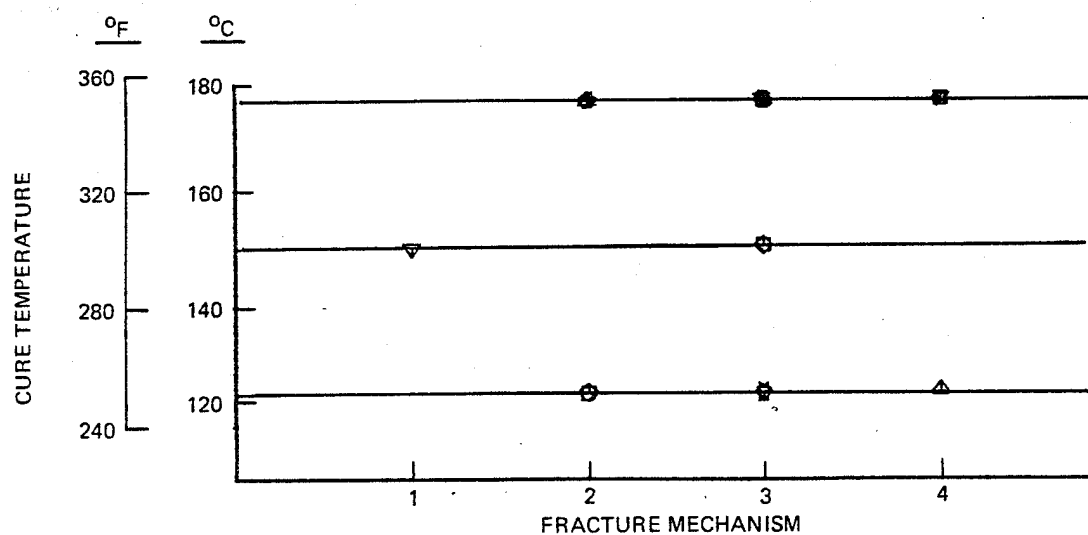


Figure 4. Fracture Mechanism Versus Cure Temperature, As-Received Specimens

CRITICAL PAGE 10
OF POOR QUALITY

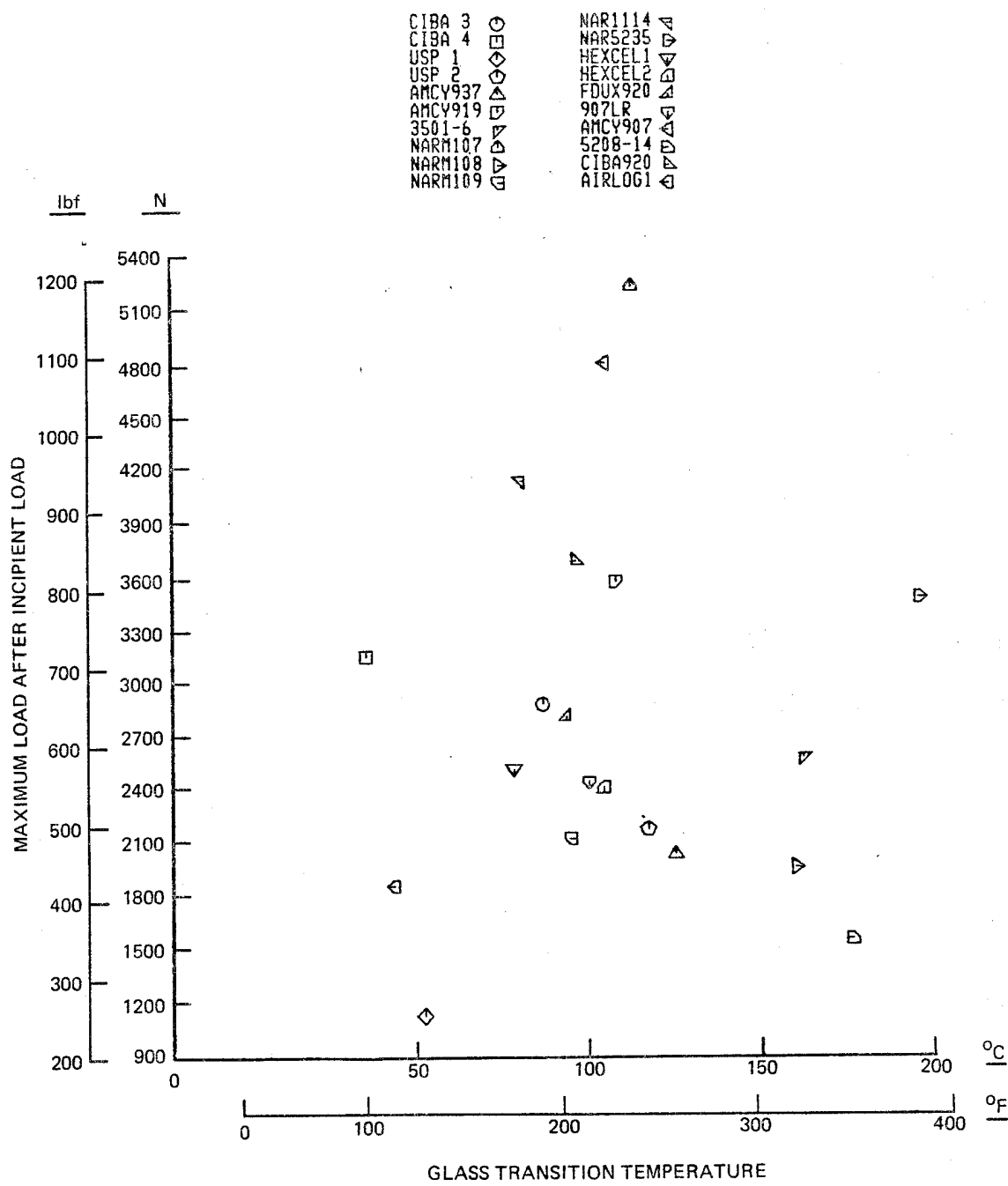


Figure 5. Maximum Load After Incipient Load Versus Glass Transition Temperature,
Impacted Specimens

INCIDENT LOAD
OF POOR QUALITY

CIBA 3	○	NAR1114	△
CIBA 4	□	NAR5235	□
USP 1	○	HEXCEL 1	△
USP 2	○	HEXCEL 2	○
AMCY937	△	FDUX920	△
AMCY919	□	907LR	○
3501-6	△	AMCY907	○
NARM107	□	S208-14	△
NARM108	△	CIBA920	○
NARM109	□	AIRLOGI	□

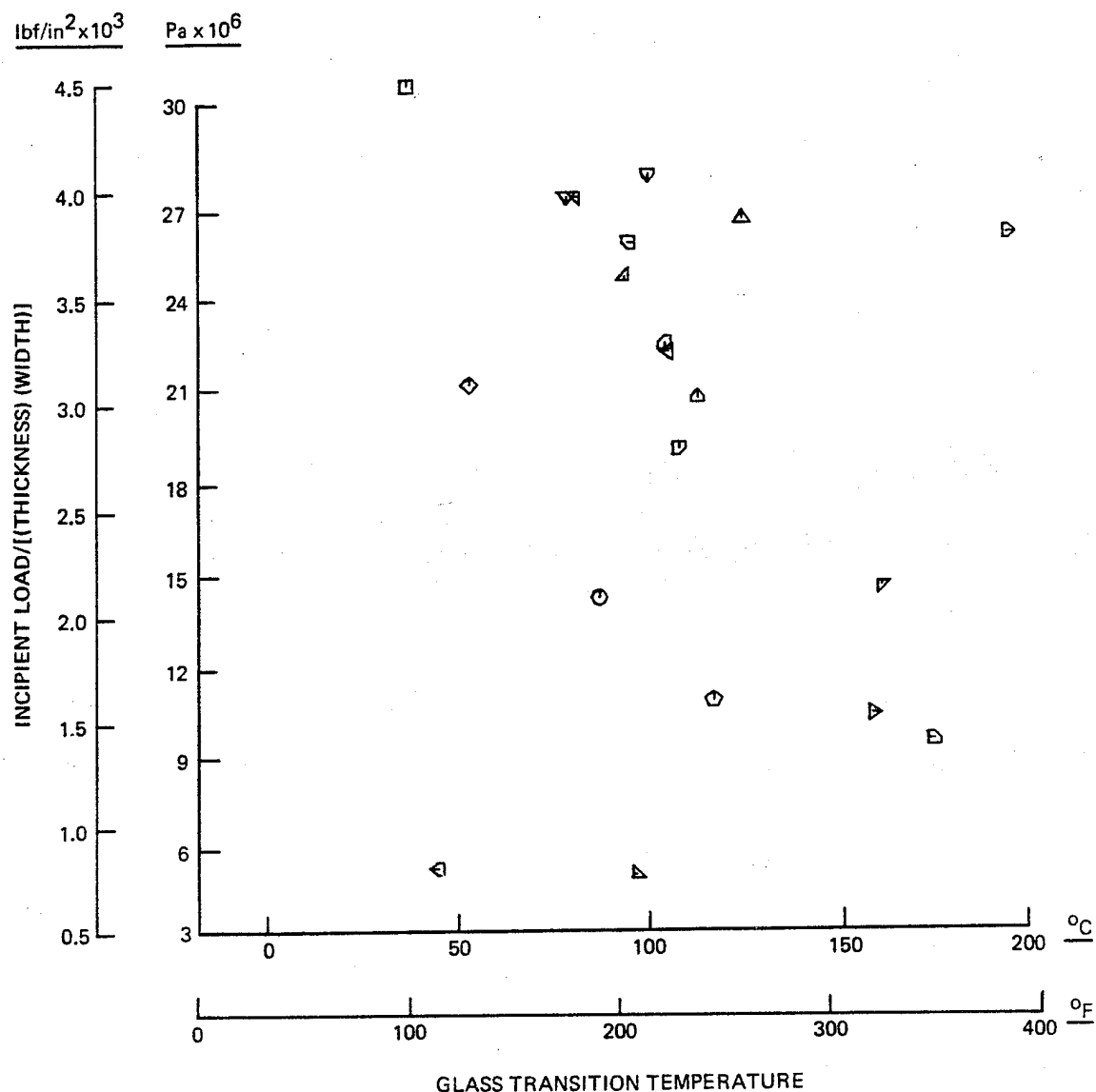


Figure 6. Incipient Load/[(Thickness) (Width)] Versus Glass Transition Temperature,
Impacted Specimens



Figure 7. Neat Resin Fracture, Narmco 5208 (200X)



Figure 8. Neat Resin Fracture, Cycom 937 (200X)

ORIGINAL PAGE
BLACK AND WHITE PHOTOGRAPH

ORIGINAL PAGE
BLACK AND WHITE PHOTOGRAPH

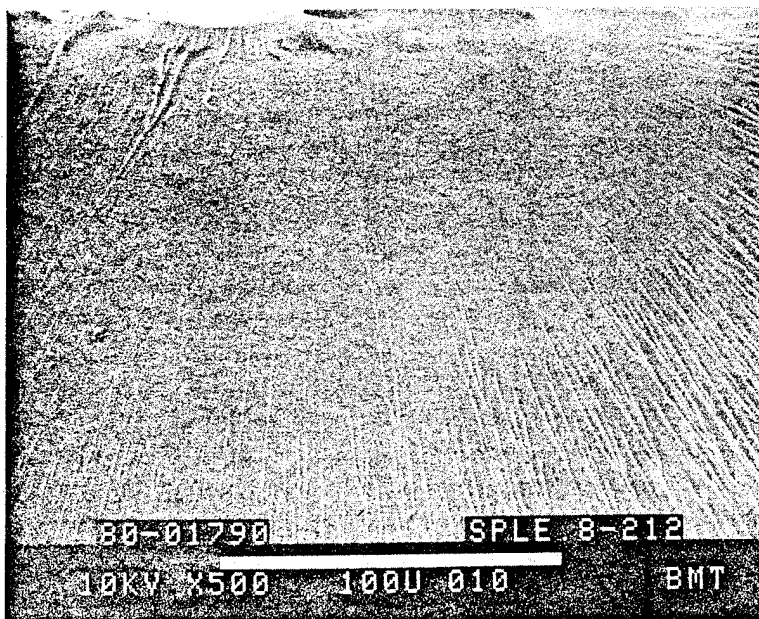


Figure 9. Fracture Origin, Neat Resin, Narmco 5208 (500X)

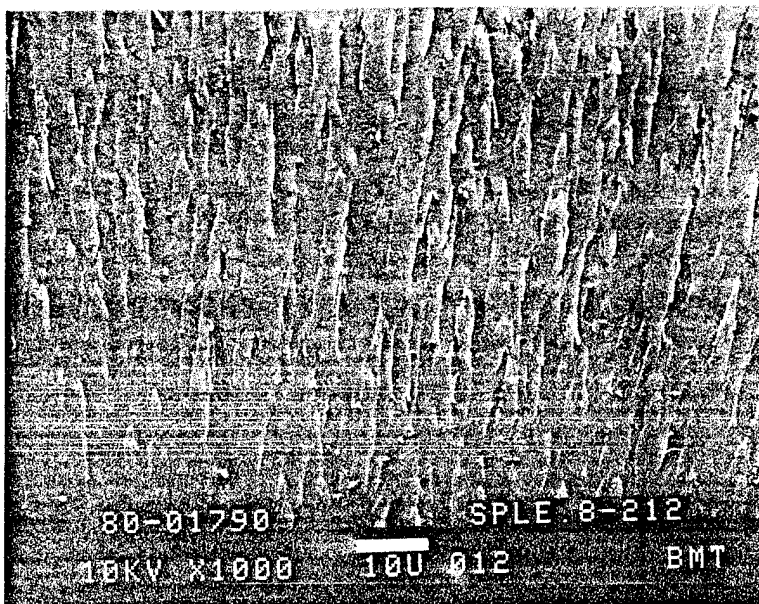


Figure 10. Crack Propagation, Neat Resin, Narmco 5208 (1000X)

CRICKMAN PAGE
BLACK AND WHITE PHOTOGRAPH

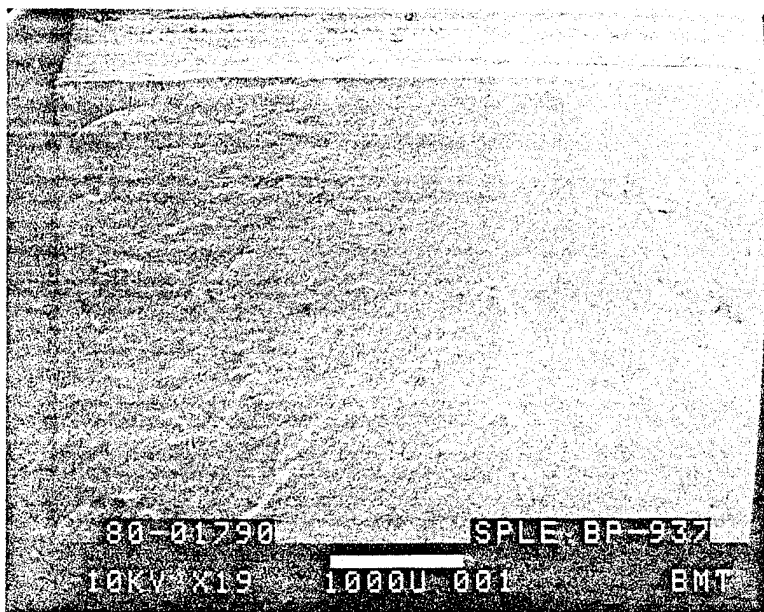


Figure 11. Fracture Origin, Neat Resin, Cycom 937 (10,000X)

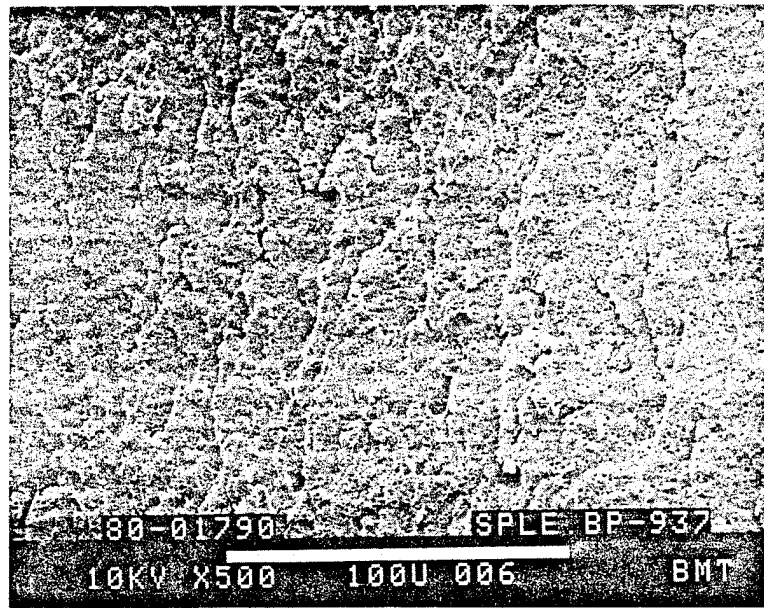


Figure 12. Crack Propagation Zone, Neat Resin, Cycom 937
(50,000X)

ORIGINAL PAGE
BLACK AND WHITE PHOTOGRAPH

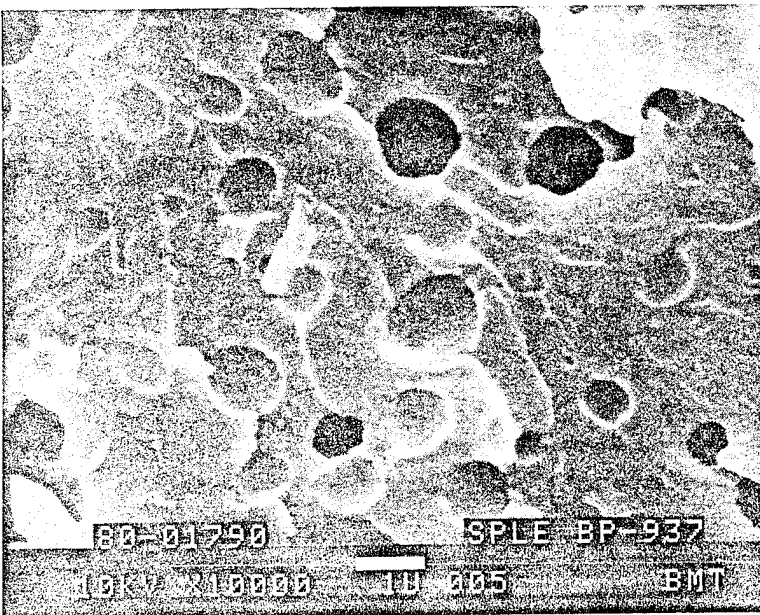


Figure 13. Elastomer Deformation Pits, Cycom 937 (19X)



Figure 14. Elastomer Deformation Pits, Cycom 937 (500X)

ORIGINAL PAGE
BLACK AND WHITE PHOTOGRAPH



Figure 15. Interlaminar Fracture, Cycom 937 (100X)

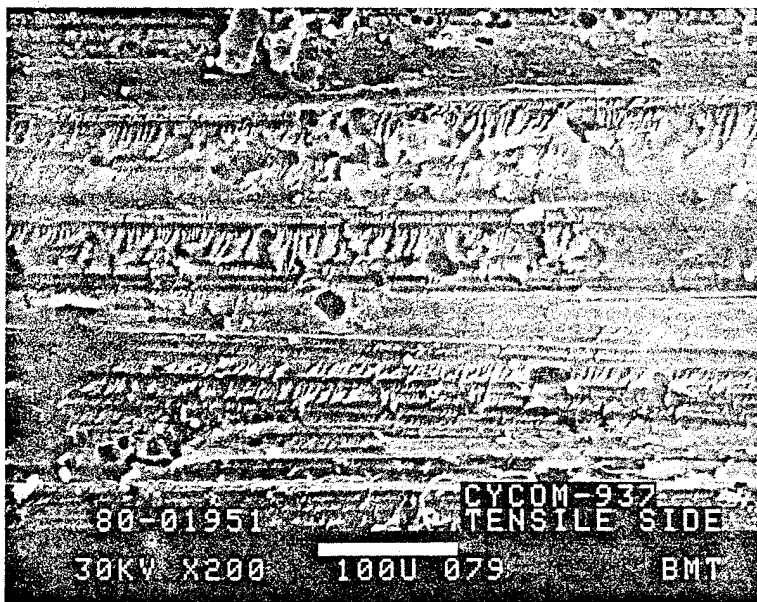
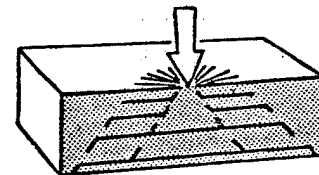


Figure 16. Interlaminar Fracture, Cycom 937 (200X)

CYCOM 937
BLACK AND WHITE PHOTOGRAPH



Figure 17. Interlaminar Fracture, Cycom 937 (500X)

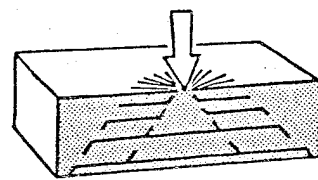


Figure 18. Interlaminar Fracture, Cycom 937 (2000X)

ORIGINAL PAGE
BLACK AND WHITE PHOTOGRAPH



Figure 19. Resin-Fiber Bonding, Cycom 937 (2500X)

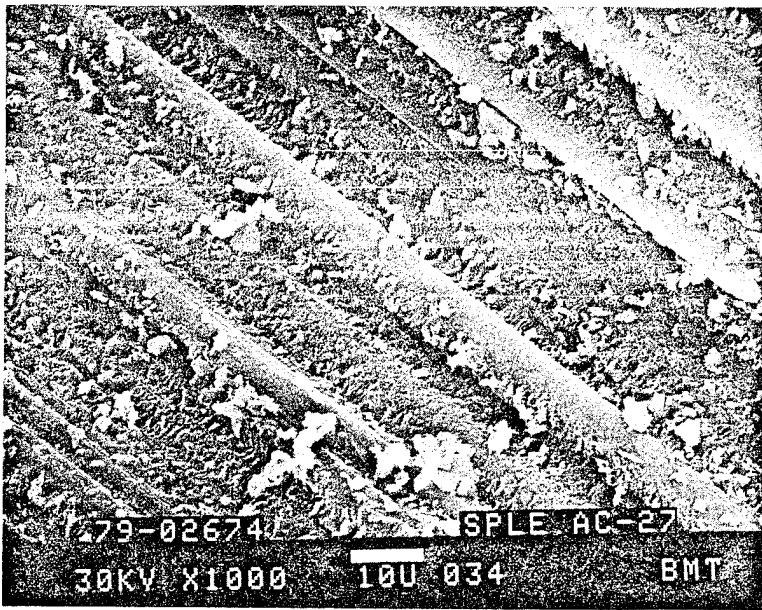
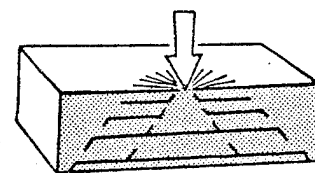


Figure 20. Static Notched Tension Failure, Origin, Cycom 937 (1000X)

ORIGINAL PAGE
BLACK AND WHITE PHOTOGRAPH

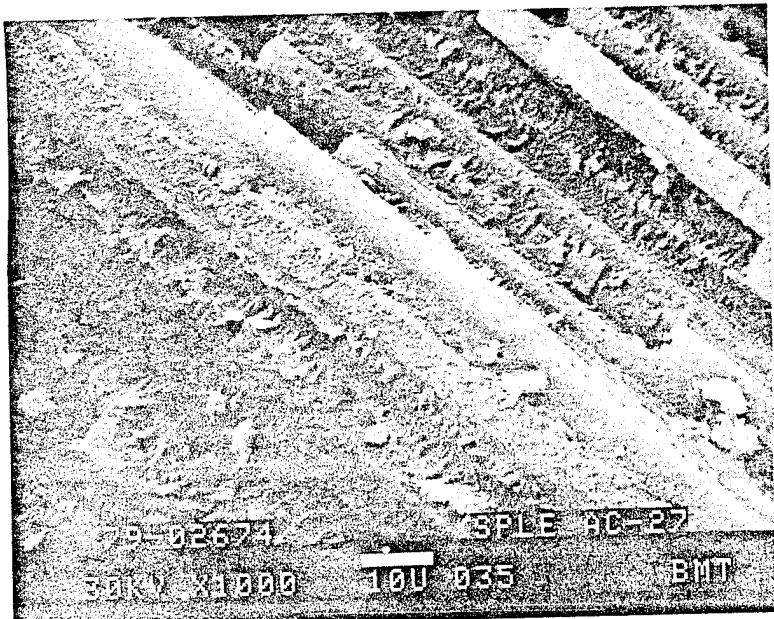


Figure 21. Static Notched Shear Failure, Propagation Zone, Cycom 937 (1000X)

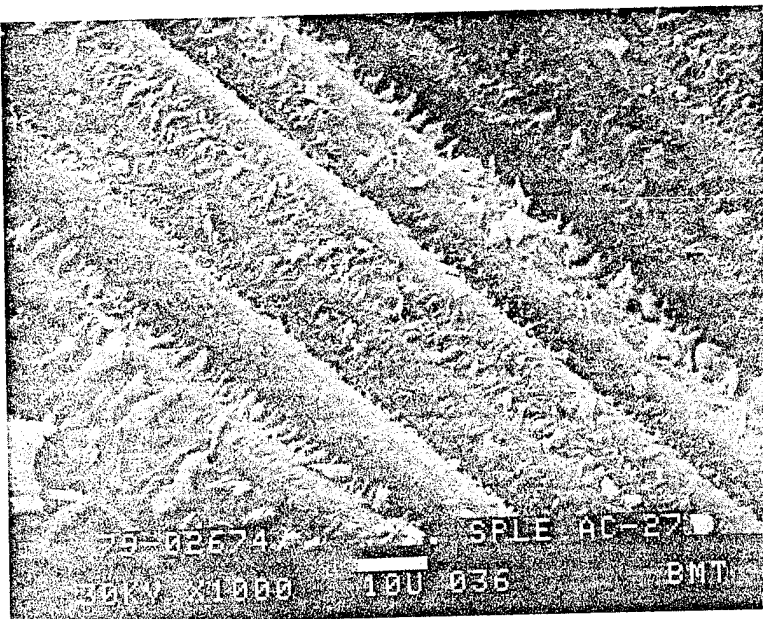


Figure 22. Static Notched Shear Failure, Different Area, Cycom 937 (1000X)

ORIGINAL PAGE
BLACK AND WHITE PHOTOGRAPH

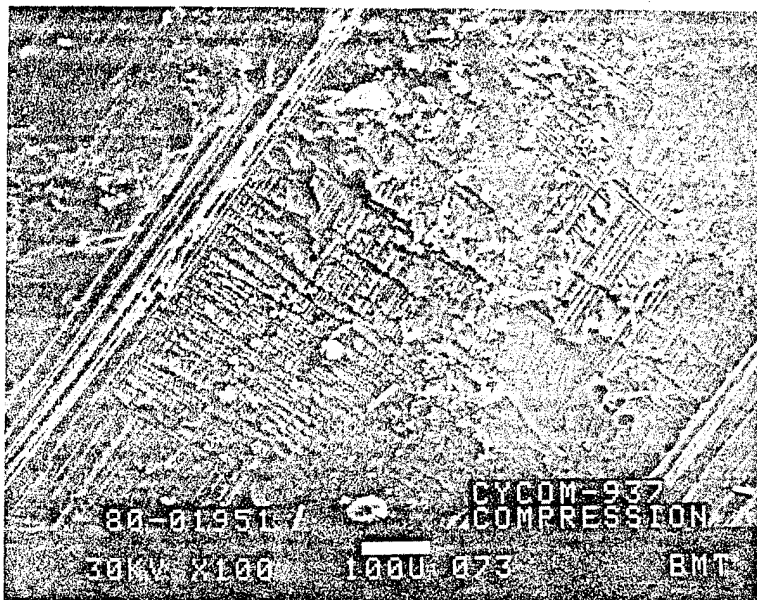


Figure 23. Compression-Loaded Interlaminar Shear Failure, Cycom 937 (100X)

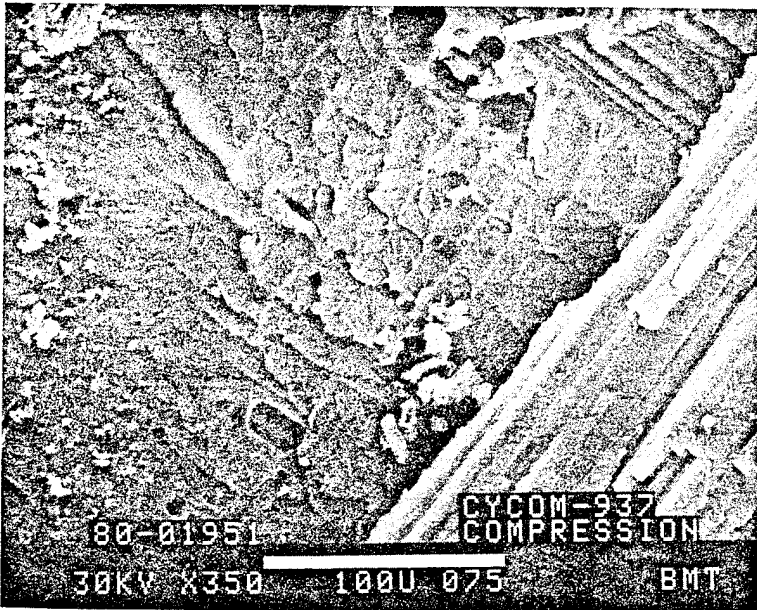
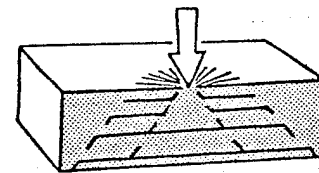


Figure 24. Compression Shear Delamination (Note Voids), Cycom 937 (350X)

ORIGINAL PAGE
BLACK AND WHITE PHOTOGRAPH



Figure 25. Static Notched Shear Failure, Propagation Zone, Cycom 937 (500X)

Note: Voids are not crack origins.

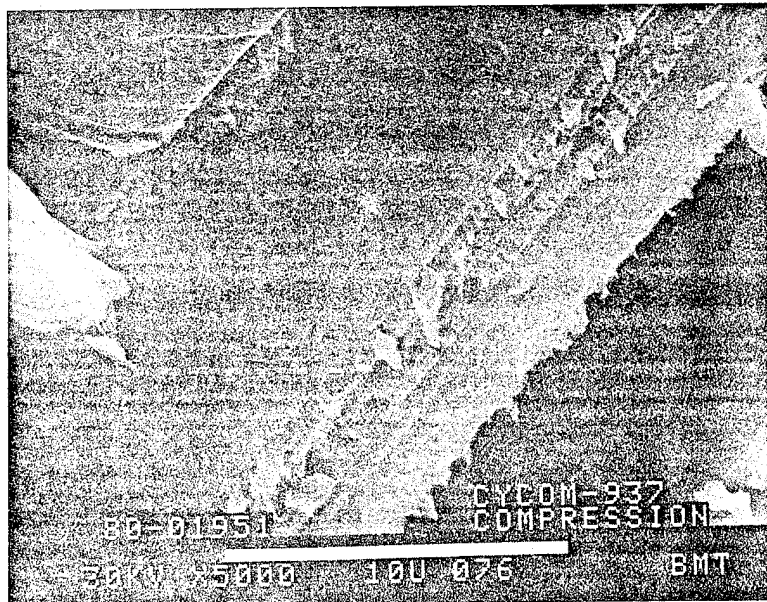
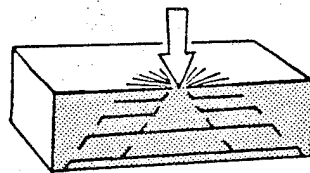


Figure 26. Fiber-Matrix Bonding, Compression Shear, Cycom 937 (5000X)

ORIGINAL PAGE
BLACK AND WHITE PHOTOGRAPH



Figure 27. Static Notched Tension Failure, Origin, Cycom 937 (1000X)



Figure 28. Static Notched Tension Failure, Propagation Zone, Cycom 937 (1000X)

ORIGINAL PAGE
BLACK AND WHITE PHOTOGRAPH

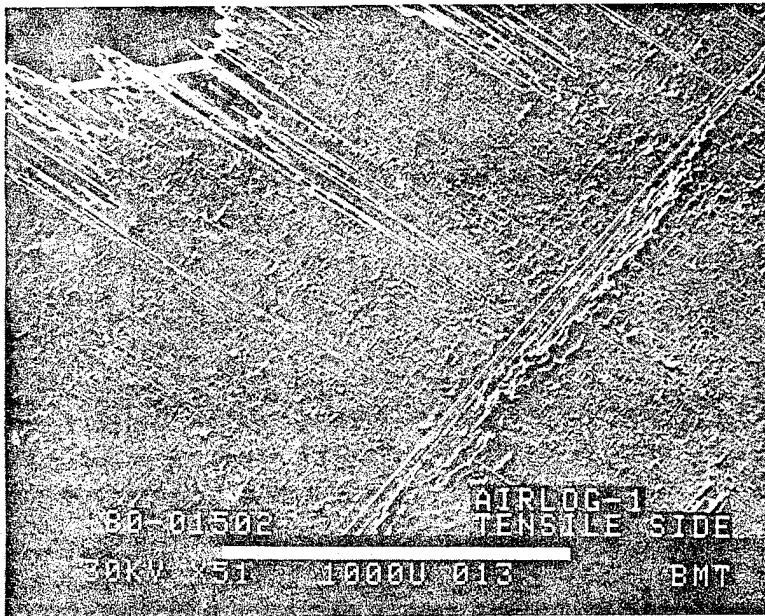
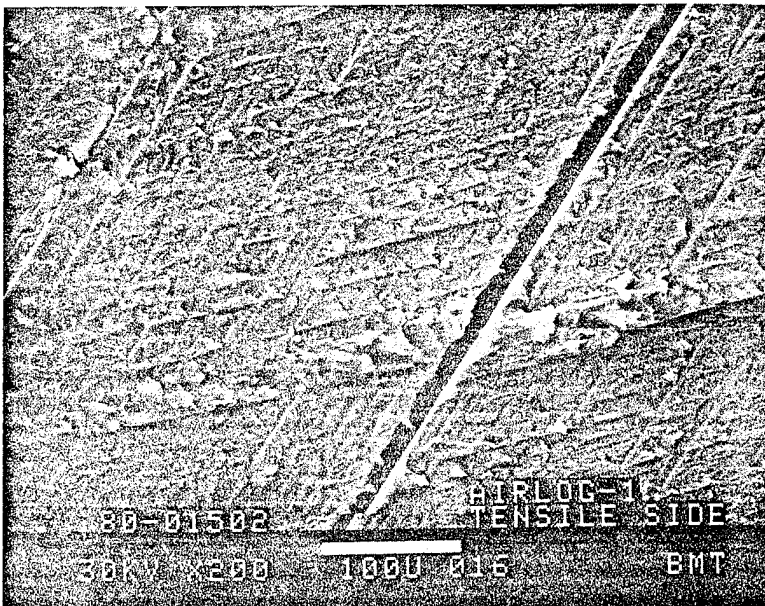
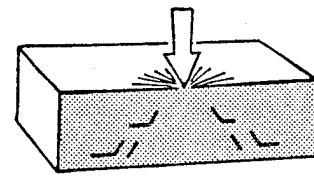


Figure 29. Delamination Face, -45-deg Ply, Air Logistics 1 (51X)



Note plastic flow.

Figure 30. Delamination Face, -45-deg Ply, Air Logistics 1 (200X)

ORIGINAL PAGE
BLACK AND WHITE PHOTOGRAPH

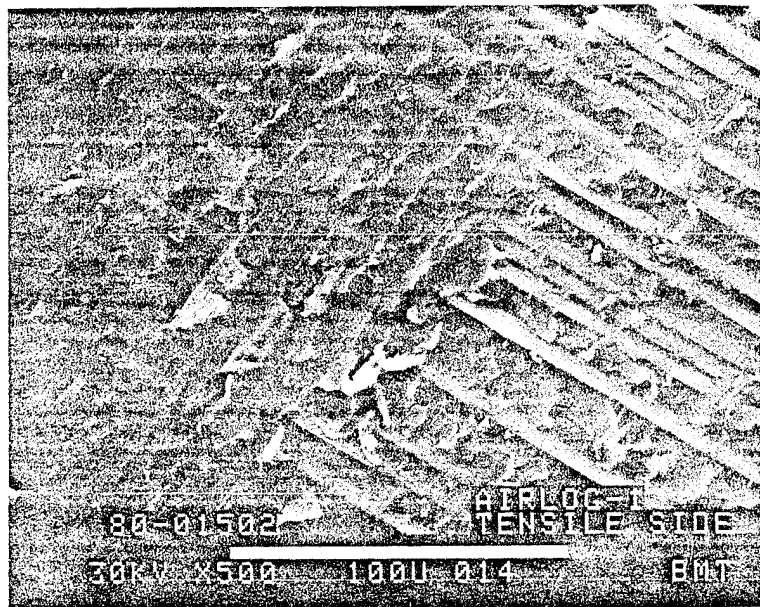


Figure 31. Plastic Deformation of Resin Around Fibers, Air Logistics 1 (500X)

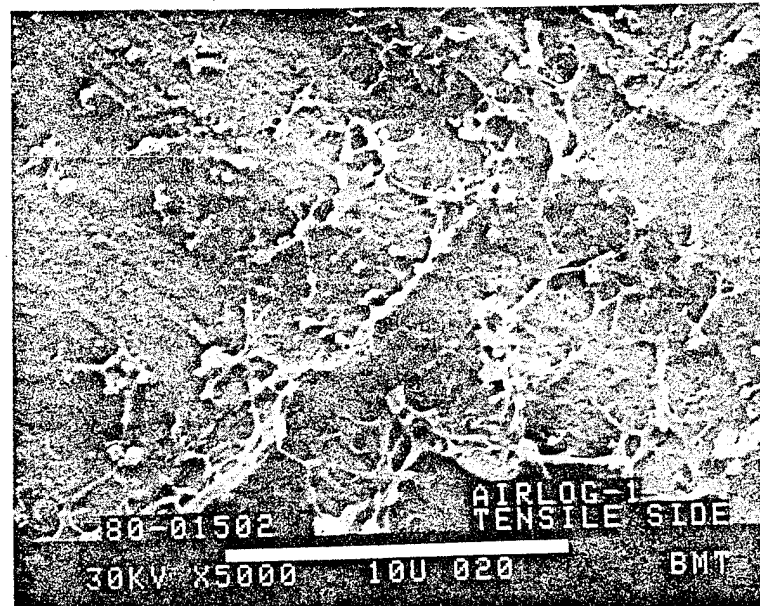
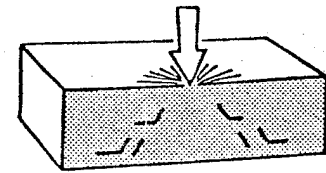


Figure 32. Extreme Resin Deformation, Air Logistics 1 (5000X)

ORIGINAL PAGE
BLACK AND WHITE PHOTOGRAPH

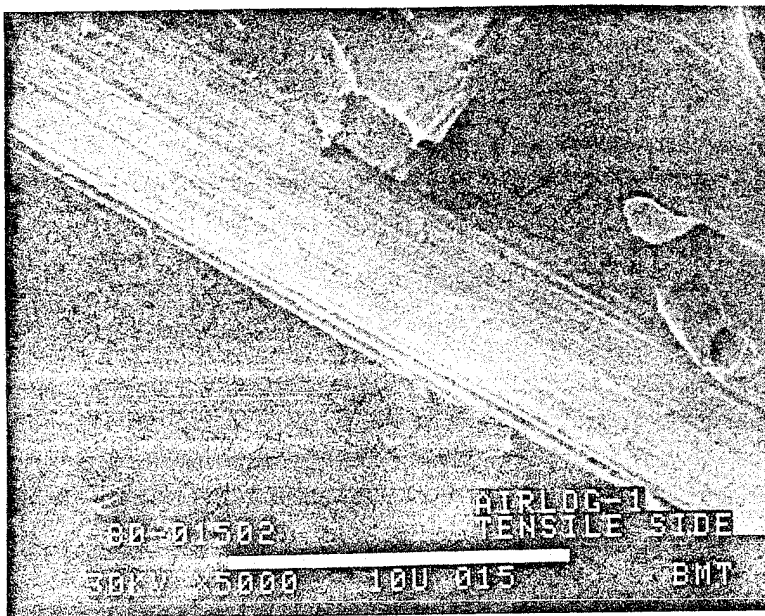


Figure 33. Fiber-Matrix Bonding, Air Logistics 1 (5000X)

Note resin layer on fiber surface

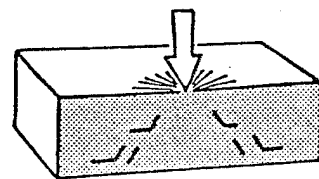
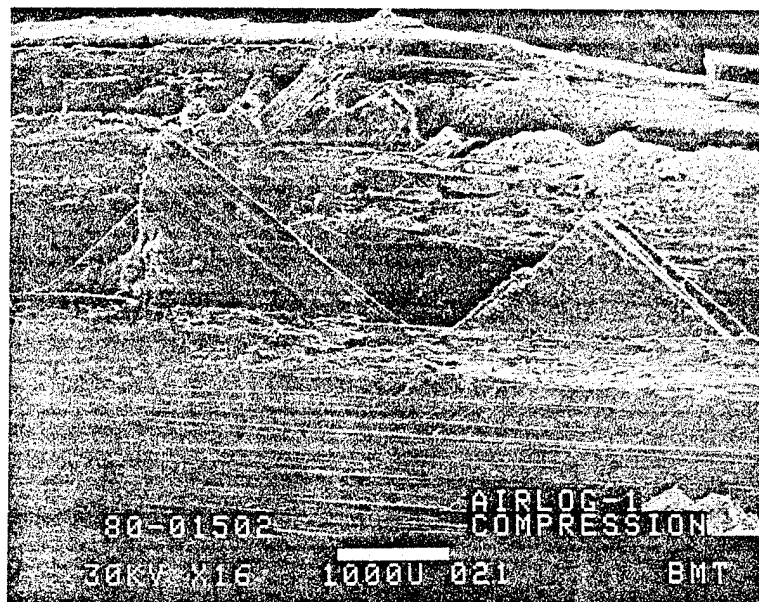


Figure 34. Covering Resin Layer, Air Logistics 1 (10,000X)

ORIGINAL PAGE
BLACK AND WHITE PHOTOGRAPH



Note flat, smooth ply boundaries.

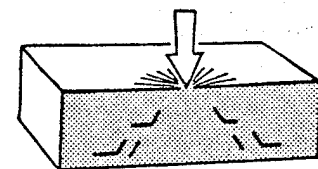
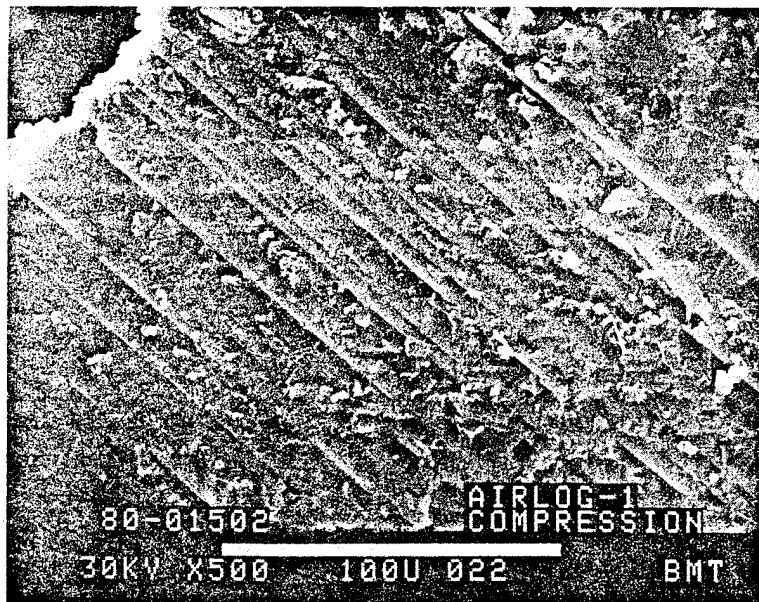


Figure 35. Compression Fracture, Air Logistics 1 (16X)



Note plastic flow between fibers.

Figure 36. Compression Shear, Air Logistics 1 (500X)

~~ORIGINAL PAGE~~
~~BLACK AND WHITE PHOTOGRAPH~~

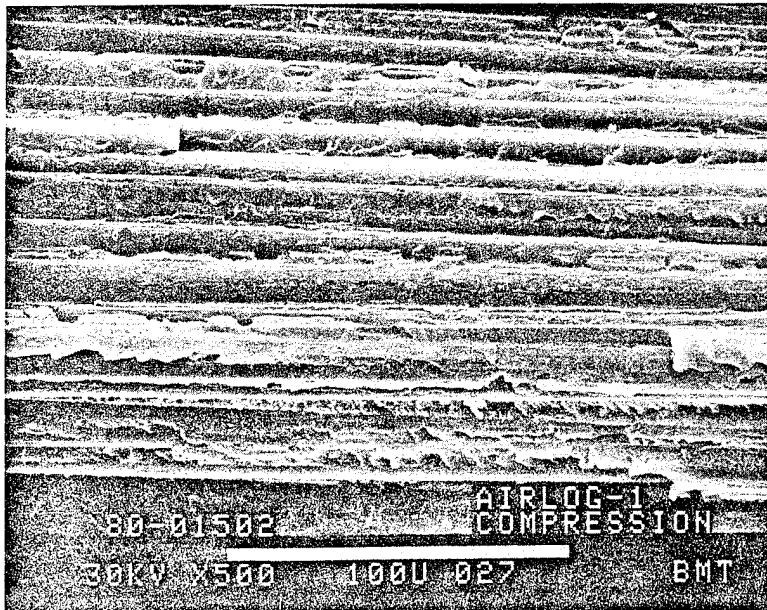


Figure 37. Transverse Compression Intraply Failure, Air Logistics 1 (500X)

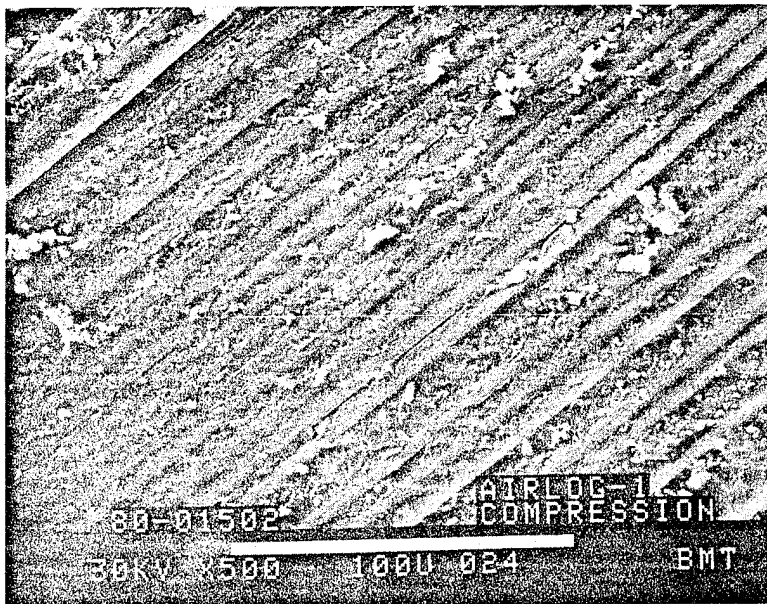
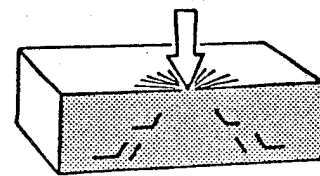


Figure 38. Compression Shear With Large Plastic Flow, Air Logistics 1 (500X)

~~ORIGINAL PAGE~~
~~BLACK AND WHITE PHOTOGRAPH~~

ORIGINAL PAGE
BLACK AND WHITE PHOTOGRAPH

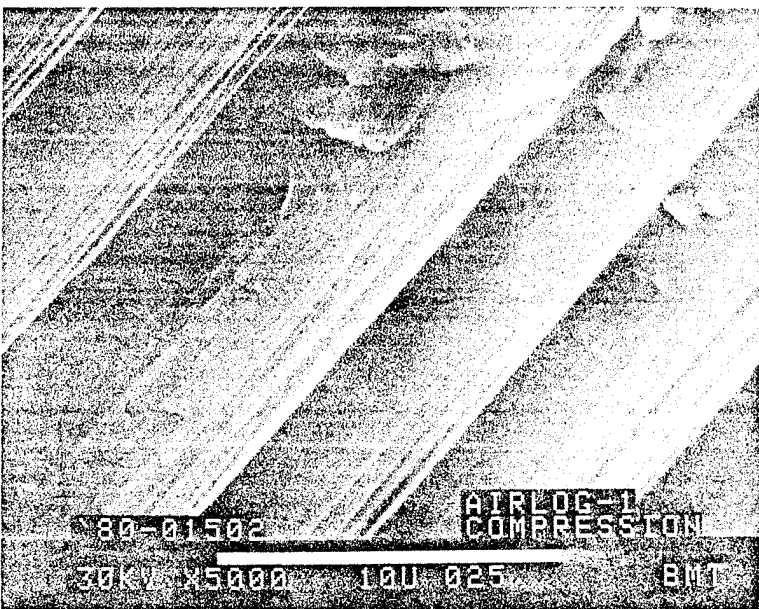


Figure 39. Fiber-Matrix Bond, Compression Side, Air Logistics 1 (5000X)

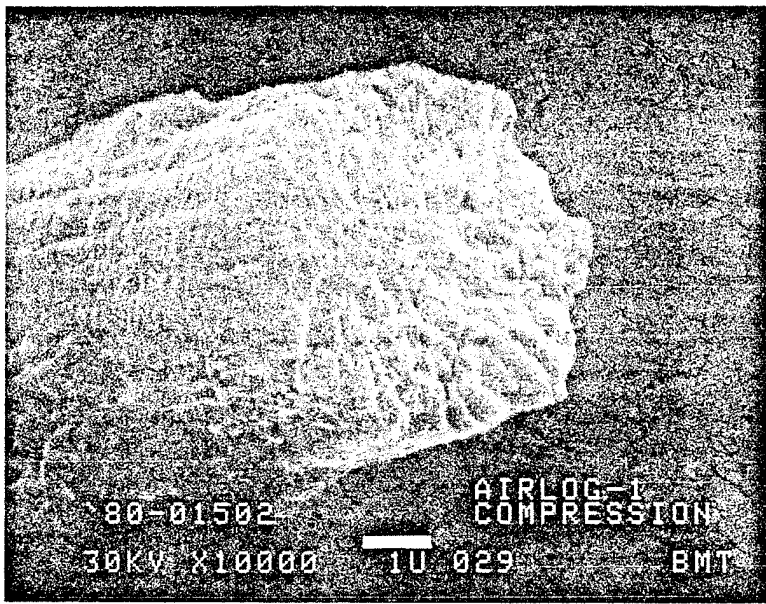
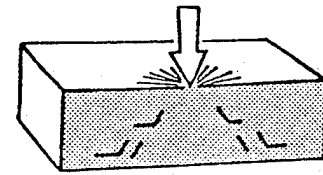


Figure 40. Fiber-Matrix Bond, Compression Side, Air Logistics 1 (10,000X)

Note cohesive failure.

ORIGINAL PAGE
BLACK AND WHITE PHOTOGRAPH

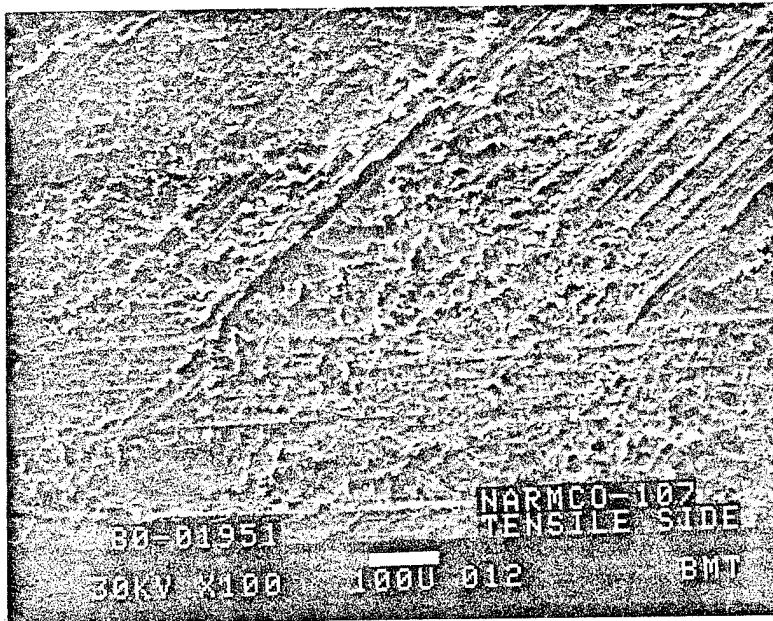


Figure 41. Plastic Flow, Shear Interlaminar Failure, Narmco 107 (100X)

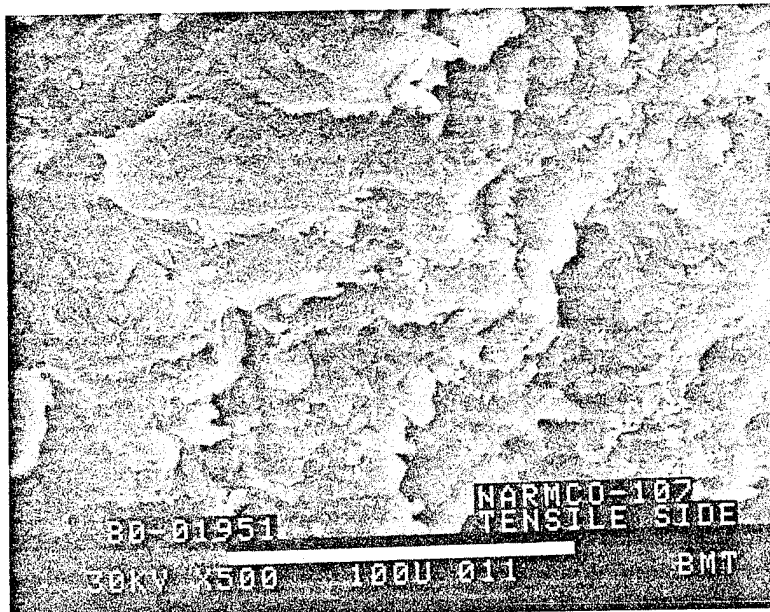
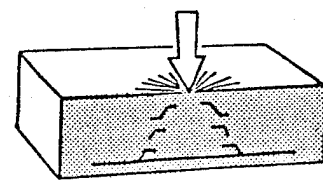


Figure 42. Plastic Flow, Shear Interlaminar Failure, Narmco 107 (500X)

ORIGINAL PAGE
BLACK AND WHITE PHOTOGRAPH



Note flow lines in resin

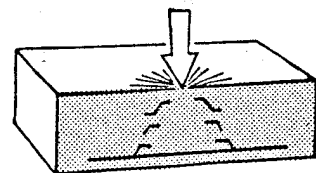


Figure 43. Flow of Resin Under Shear Loads, Narmco 107 (5000X)



Figure 44. Hairy Appearance, Possible Elastomer Formation,
Narmco 107 (10,000X)

ORIGINAL PAGE
BLACK AND WHITE PHOTOGRAPH

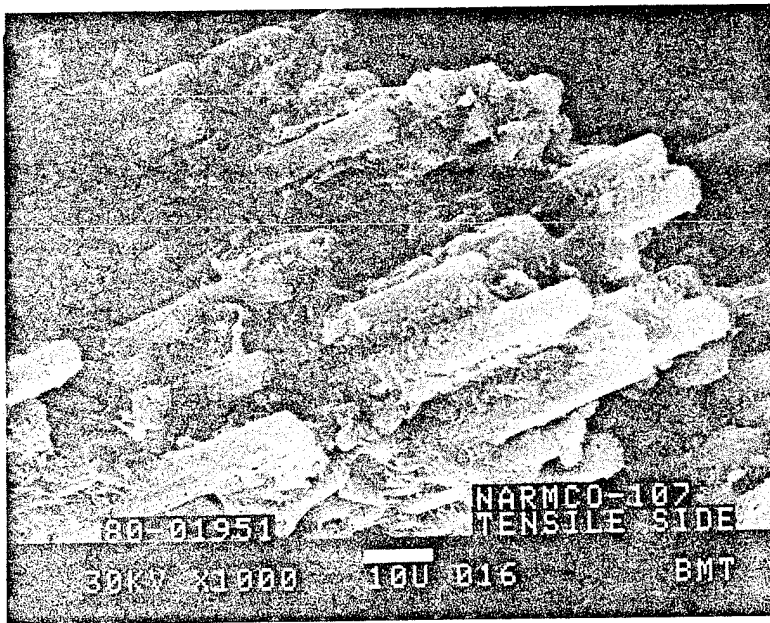
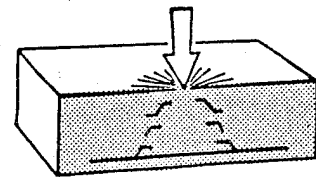


Figure 45. Resin-Fiber Bonds, Narmco 107 (1000X)



Note resin deformation.

Figure 46. Resin-Fiber Bonds, Narmco 107 (10,000X)

ORIGINAL PAGE
BLACK AND WHITE PHOTOGRAPH



Figure 47. Compression-Loaded Shear, Narmco 107 (100X)

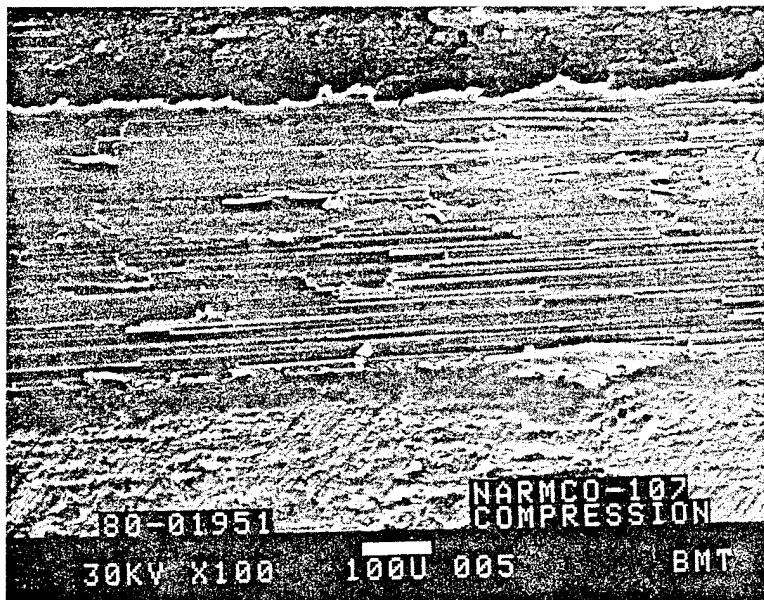
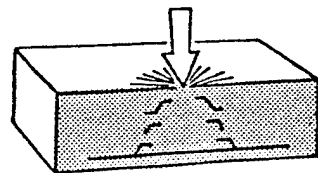


Figure 48. Transverse Fracture from Compression Side, Narmco 107 (100X)

ORIGINAL PAGE
BLACK AND WHITE PHOTOGRAPH

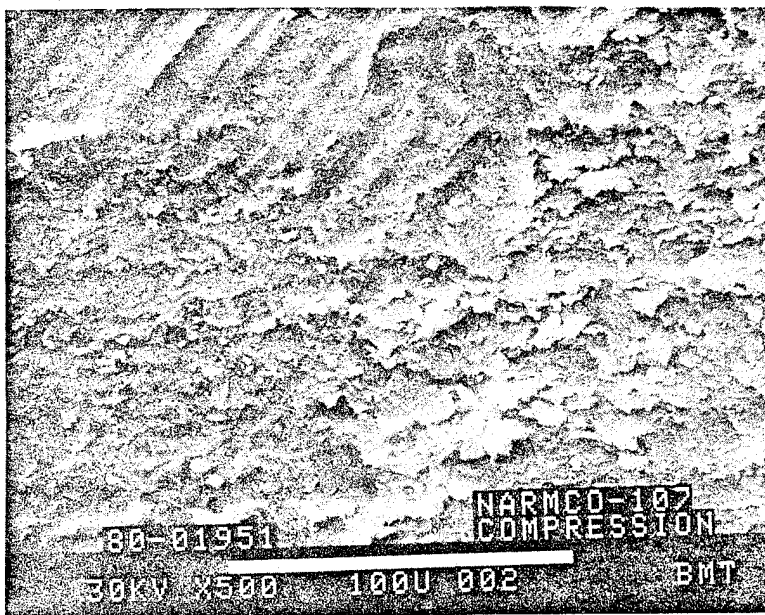


Figure 49. Compression Shear, Narmco 107 (500X)

Note: Same area as figure 47.

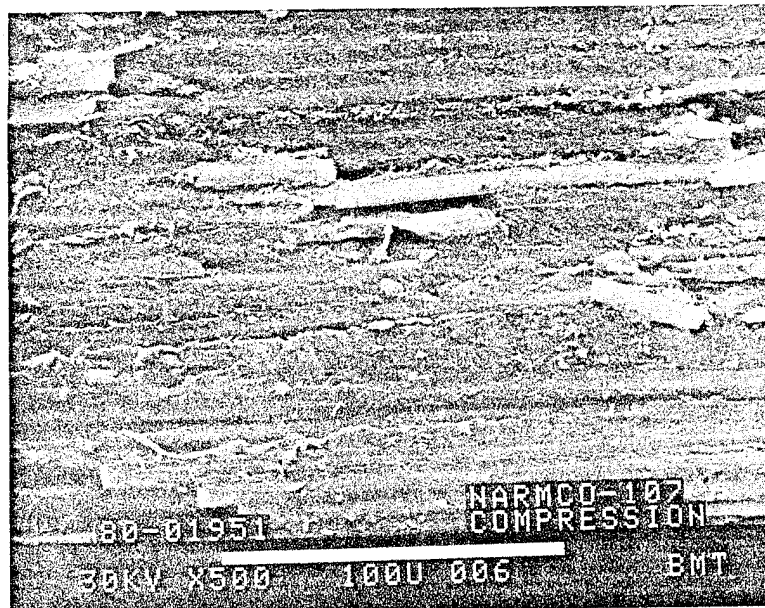
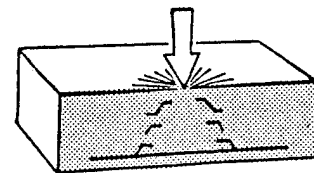


Figure 50. Transverse Fracture of 90-deg Ply, Narmco 107 (500X)

Note: Same area as figure 48.

ORIGINAL PAGE
BLACK AND WHITE PHOTOGRAPH



Figure 51. Transverse Ply Fracture, Compression Side, Narmco 107 (1000X)

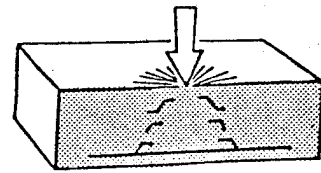


Figure 52. Hairy Skin Fracture Appearance, Shear-Loaded, Narmco 107 (5000X)

ORIGINAL PAGE
BLACK AND WHITE PHOTOGRAPH



Figure 53. Compression Shear Hairs, Narmco 107 (20,000X)

Note that hairs are part of larger resin blocks.

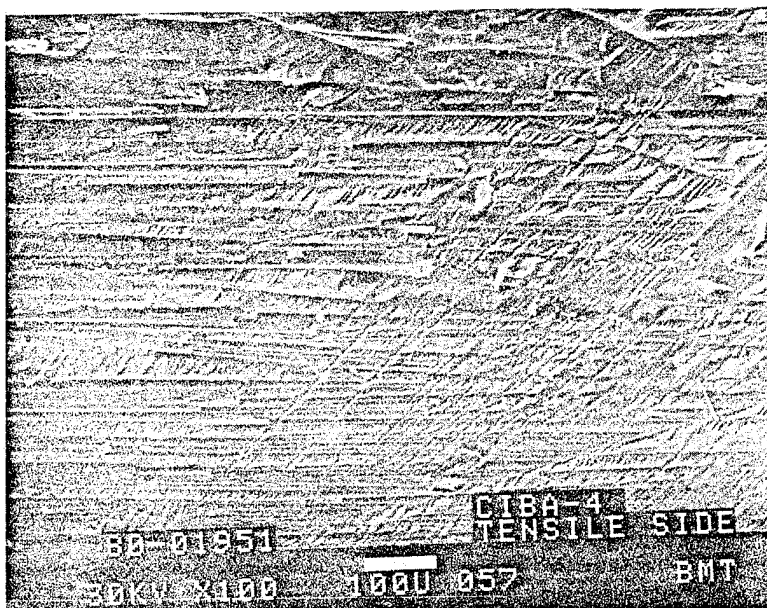
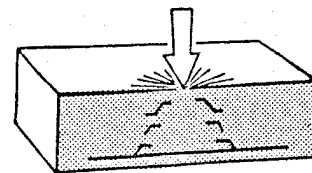


Figure 54. Delamination Fracture, Tension Side, Ciba 4 (100X)

ORIGINAL PAGE
BLACK AND WHITE PHOTOGRAPH

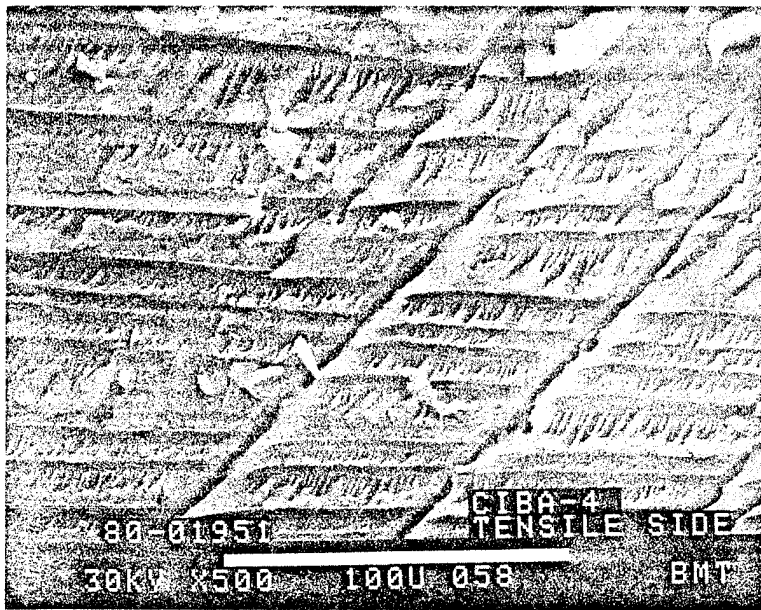


Figure 55. Apparent Brittle Fracture, Delamination Face, Ciba 4 (500X)

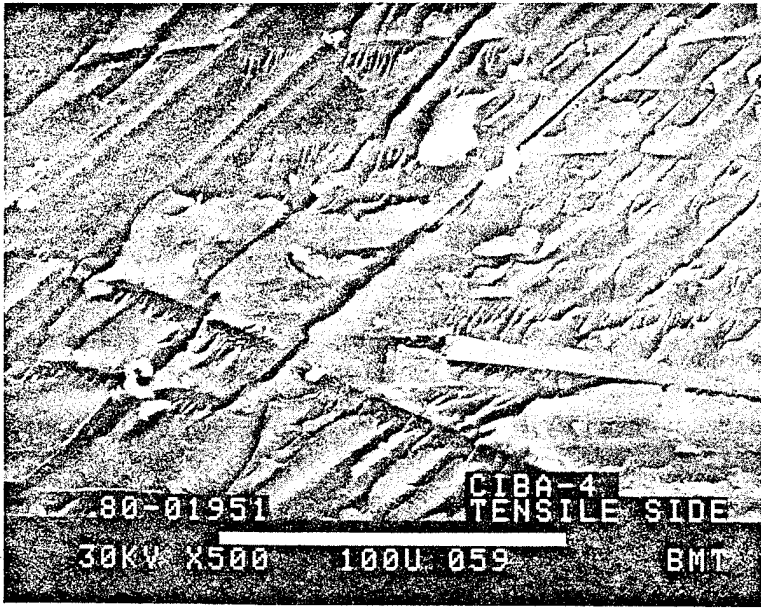
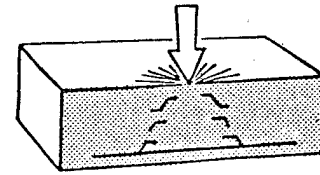


Figure 56. Apparent Brittle Fracture, Ciba 4 (500X)

ORIGINAL PAGE
BLACK AND WHITE PHOTOGRAPH



Figure 57. Notched Shear Static Failure, Narmco 5208 (900X)



Figure 58. Notched Shear Static Failure, Different Area, Narmco 5208 (1000X)

ORIGINAL PAGE
BLACK AND WHITE PHOTOGRAPH

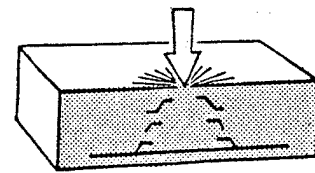


Figure 59. Resin Tension Fracture, Ciba 4 (2000X)

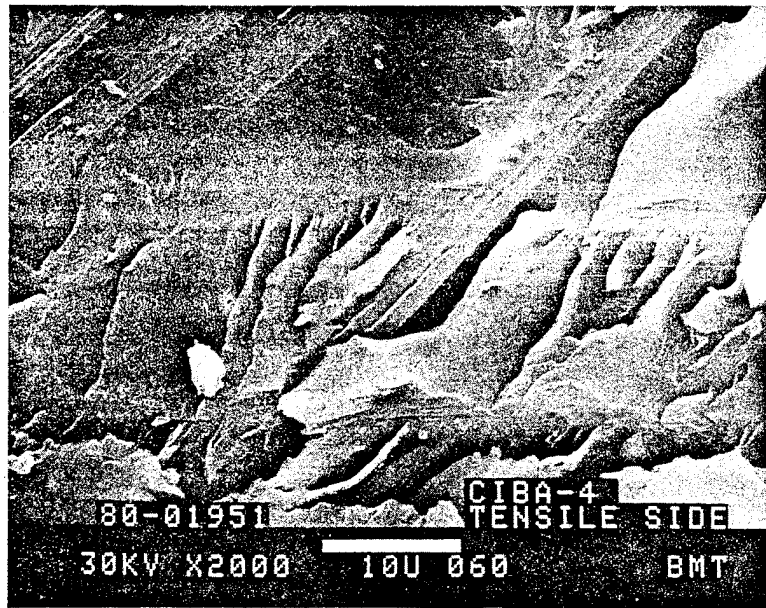


Figure 60. Resin Tension Fracture, Different Area, Ciba 4 (2000X)

ORIGINAL PAGE
BLACK AND WHITE PHOTOGRAPH

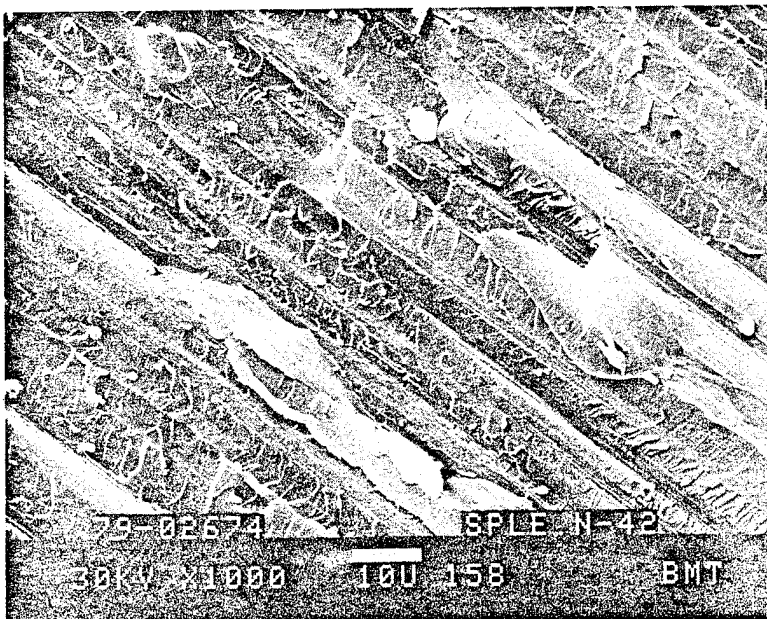


Figure 61. 90-deg Tension Failure Near Origin, Narmco 5208 (1000X)

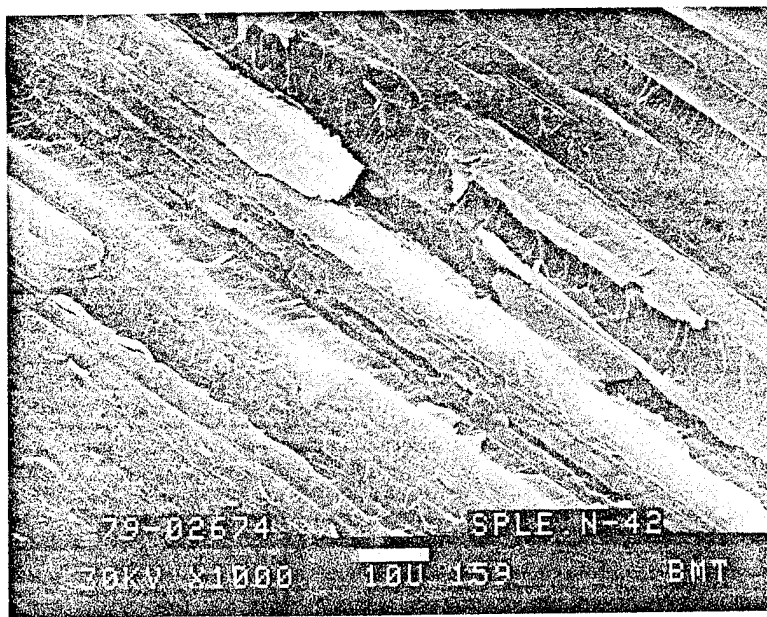


Figure 62. 90-deg Tension Failure, Propagation Zone, Narmco 5208 (1000X)

C-2

ORIGINAL FREE
BLACK AND WHITE PHOTOGRAPH



Figure 63. Fiber-Matrix Bond, Ciba 4 (10,000X)

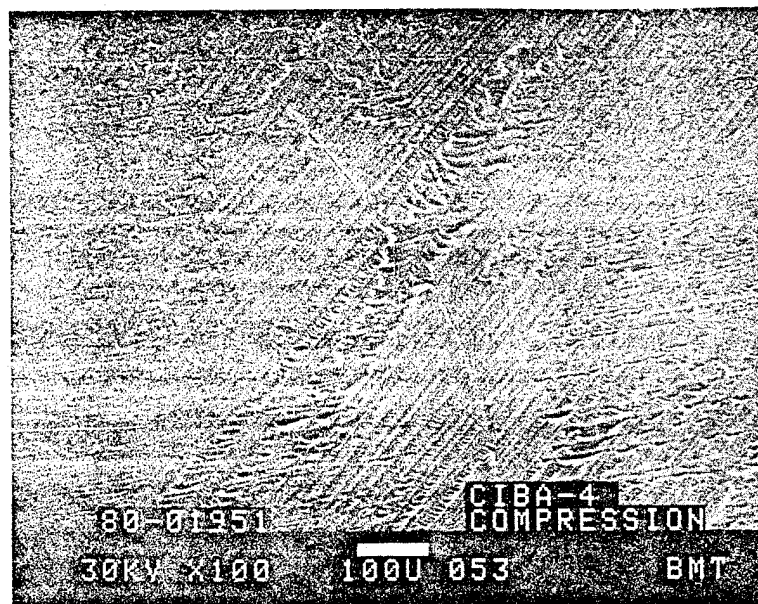
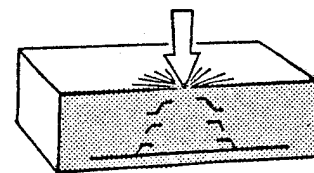


Figure 64. Compression-Loaded Interlaminar Fracture, Ciba 4 (100X)

ORIGINAL PAGE
BLACK AND WHITE PHOTOGRAPH

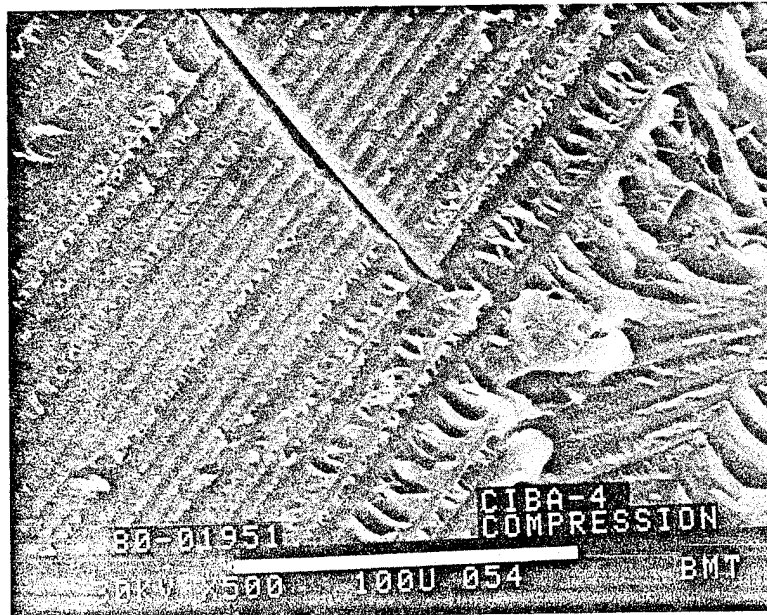


Figure 65. Compression-Loaded Interlaminar Shear Failure, Ciba 4 (500X)

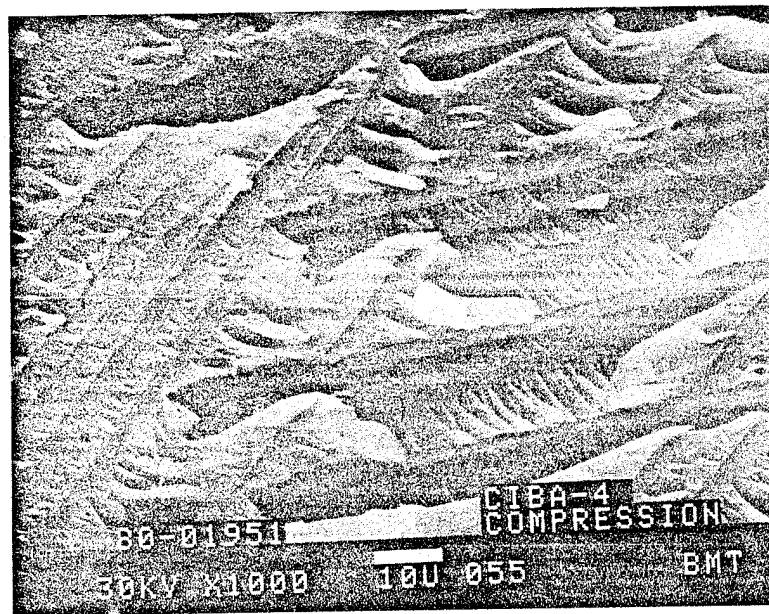
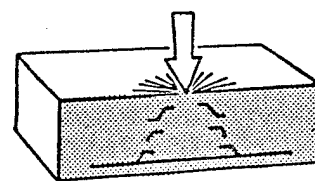


Figure 66. Compression-Loaded Interlaminar Shear Failure, Ciba 4 (1000X)

ORIGINAL PAGE
BLACK AND WHITE PHOTOGRAPH

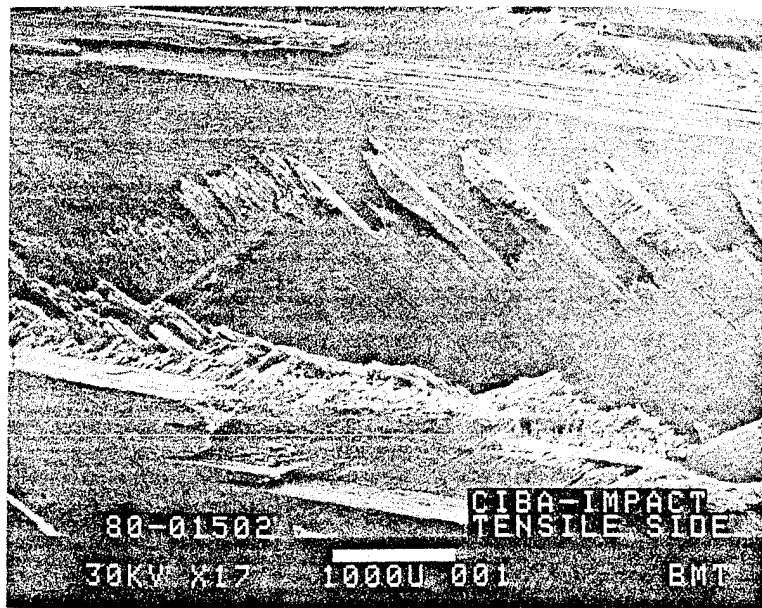


Figure 67. Tension Failure, Ciba 1M (17X)

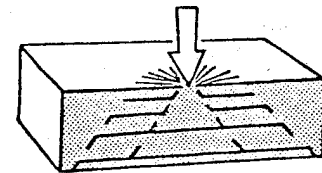
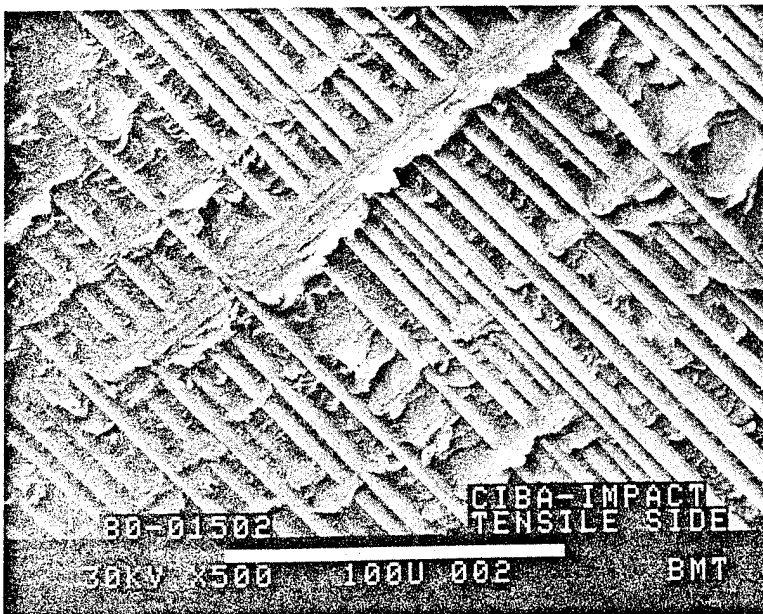


Figure 68. Typical Crossply Failure, Significant Pullout, Ciba 1M (200X)

ORIGINAL PAGE
BLACK AND WHITE PHOTOGRAPH

ORIGINAL PAGE
BLACK AND WHITE PHOTOGRAPH



Note rounded cleavage facets

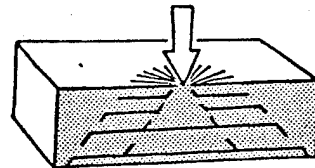


Figure 69. Delamination Face, Ciba 1M (500X)

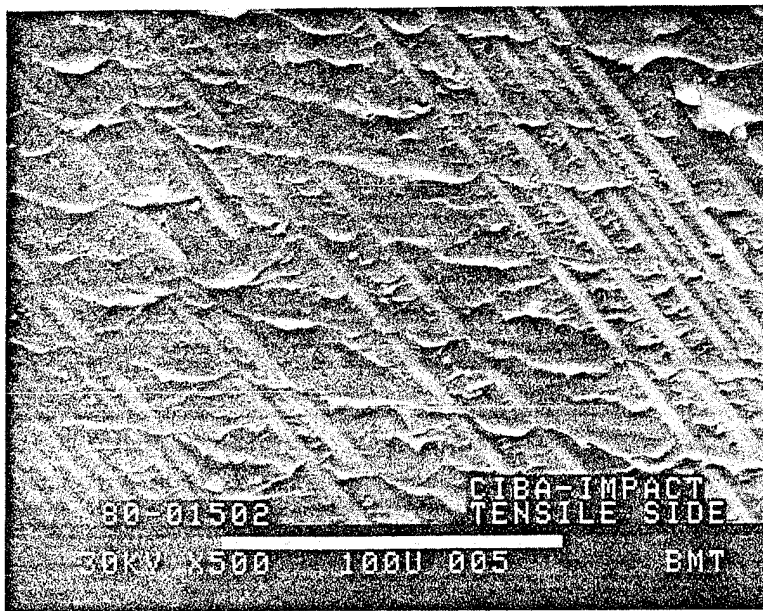
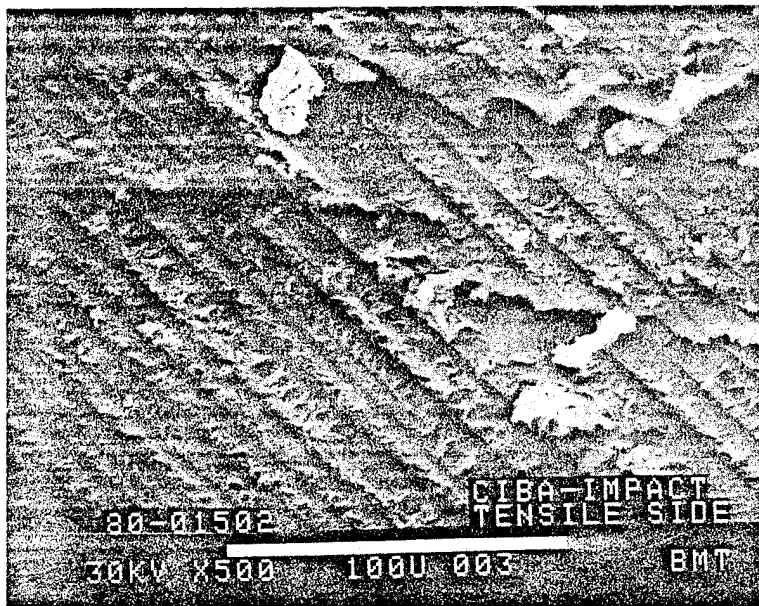


Figure 70. Delamination Face, More Pronounced, Ciba 1M (500X)

ORIGINAL PAGE
BLACK AND WHITE PHOTOGRAPH



Note thick resin layers.

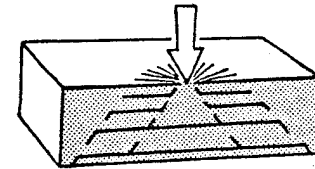


Figure 71. Resin Side of Fracture Delamination Face, Ciba 1M (500X)

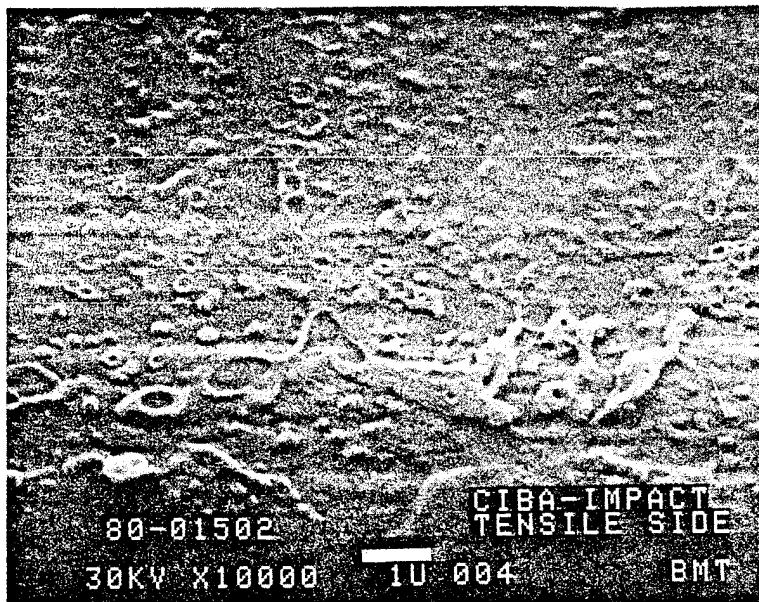


Figure 72. Fiber-Matrix Bonding, Ciba 1M (10,000X)

ORIGINAL PAGE
BLACK AND WHITE PHOTOGRAPH

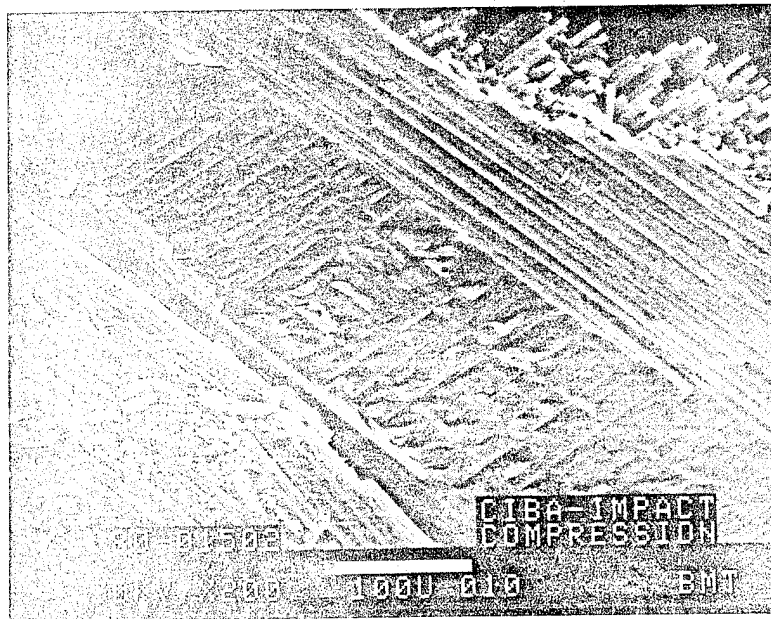


Figure 73. Neutral Axis, Ciba 1M (200X)

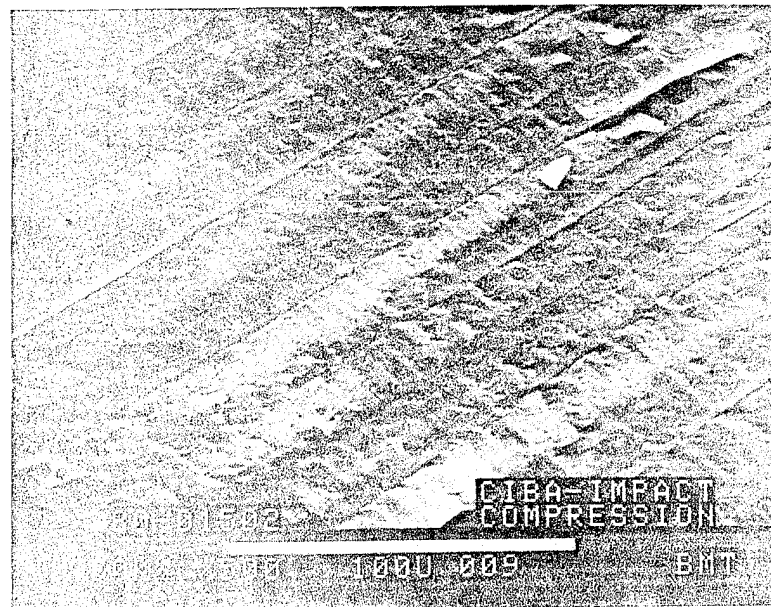
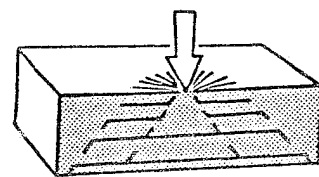
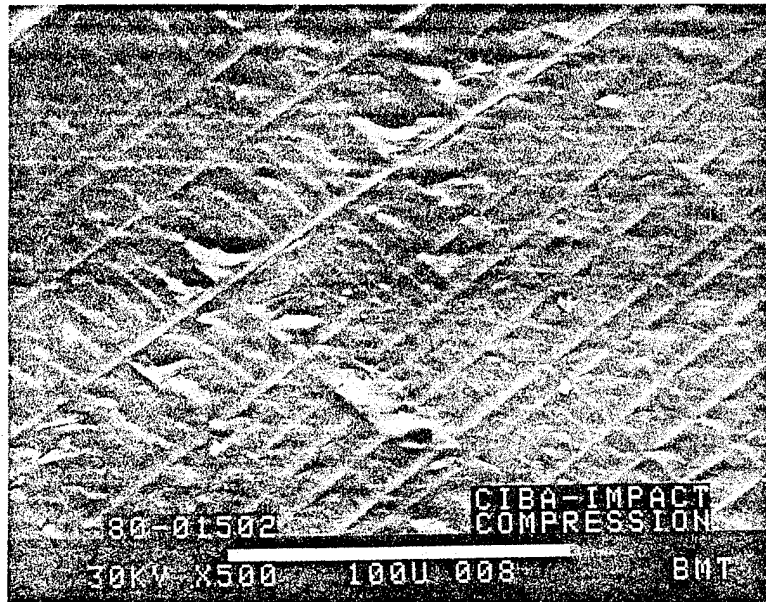


Figure 74. Neutral Axis, Ciba 1M (500X)

ORIGINAL PAGE
BLACK AND WHITE PHOTOGRAPH



Note: Similar area to figure 74.

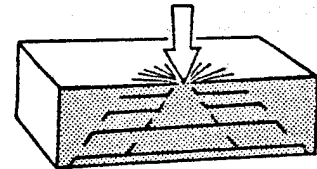


Figure 75. Neutral Axis, Ciba 1M (500X)

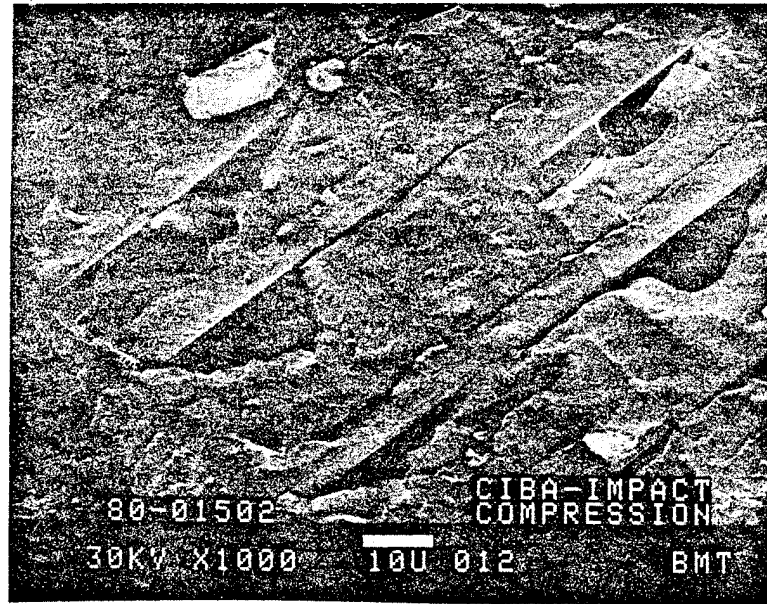


Figure 76. Influence of Voids on Fracture, Ciba 1M (1000X)

ORIGINAL PAGE
BLACK AND WHITE PHOTOGRAPH

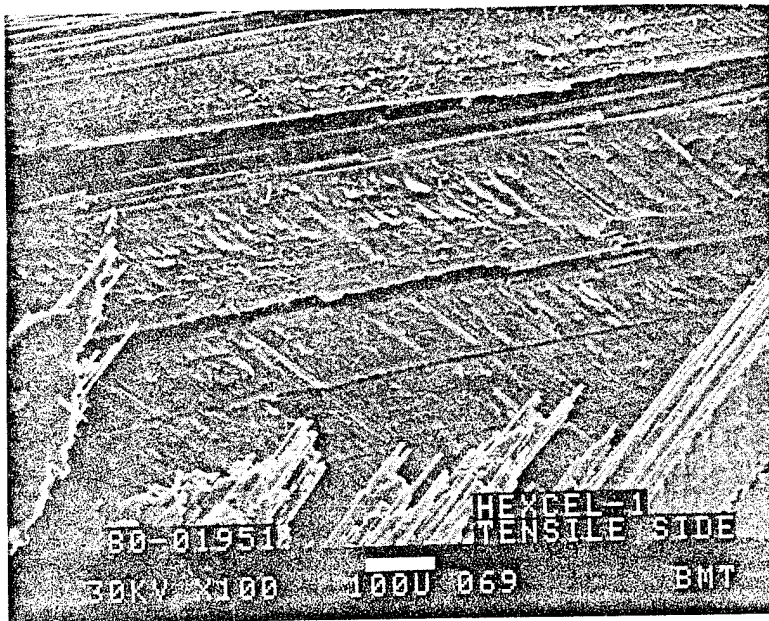


Figure 77. Delamination Plane with Transverse Cracks, Hexcel 1
(100X)

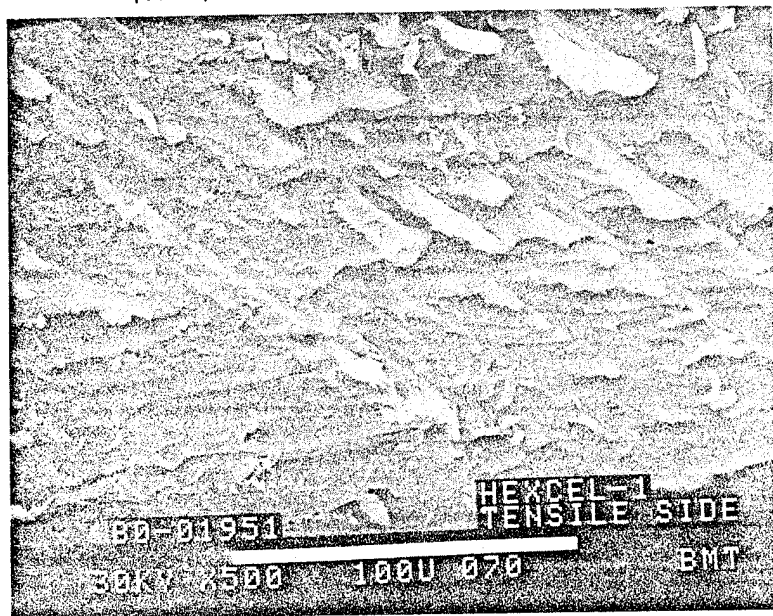
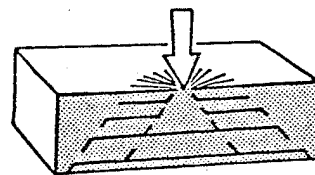


Figure 78. Plastic Flow on Shear Interlaminar Plane, Hexcel 1
(500X)

ORIGINAL PAGE
BLACK AND WHITE PHOTOGRAPH



Figure 79. Good Resin Ductility, Transverse Tension Loading,
Hexcel 1 (4000X)

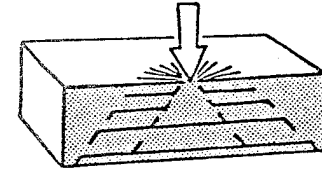


Figure 80. Resin Flow With Pits, Hexcel 1 (10,000X)

BLACK AND WHITE PHOTOGRAPH



Figure 81. Resin Plastic Flow, Compression-Loaded Shear, Mexcel 1
(6000X)

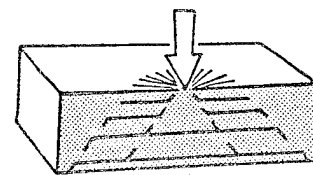


Figure 82. Resin Ductility, Mexcel 1 (6000X)

Note pits conform to resin flow

BLACK AND WHITE

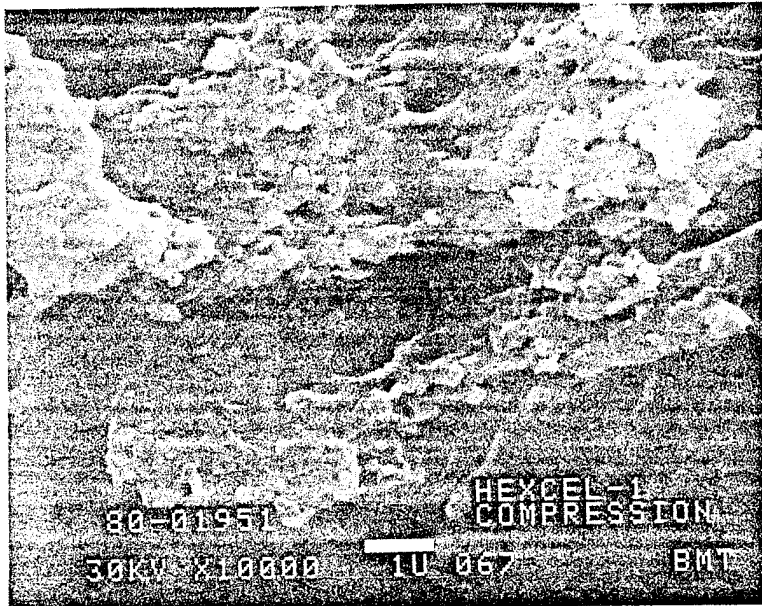


Figure 83. Resin Flow, Hexcel 1 (10,000X)

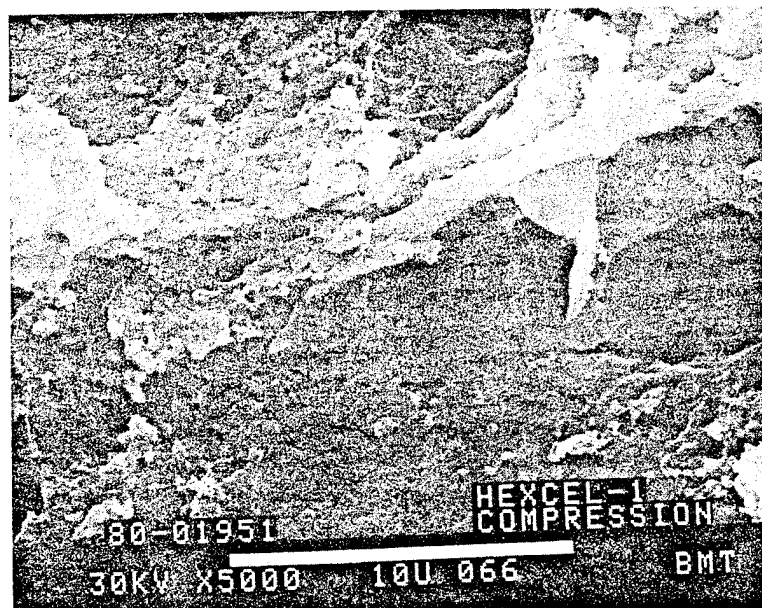


Figure 84. Resin Flow, Different Area, Hexcel 1 (5000X)

ORIGINAL PAGE
BLACK AND WHITE PHOTOGRAPH

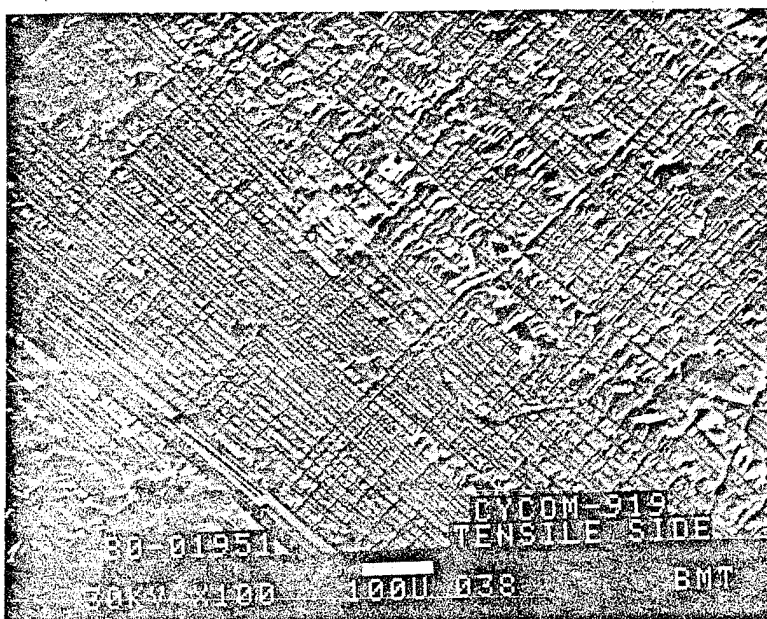


Figure 85. Apparent Brittle Fracture, Cycom 919 (100X)

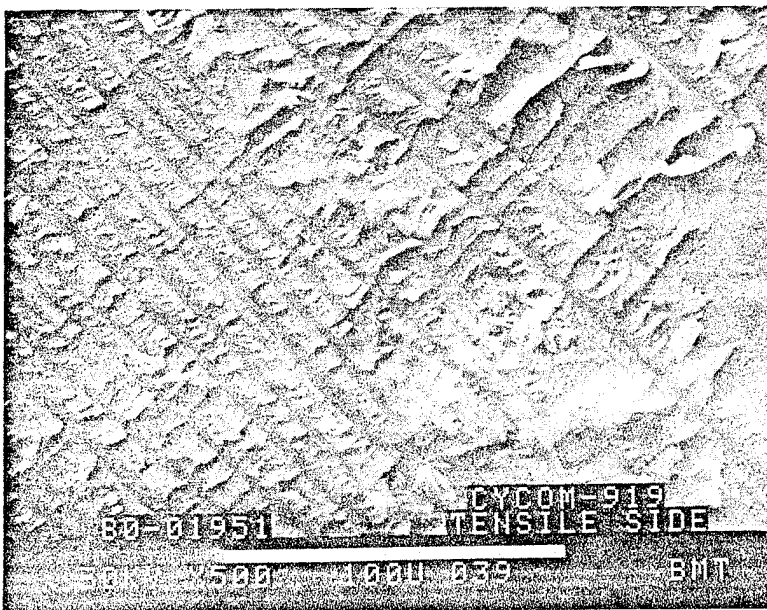


Figure 86. Apparent Brittle Fracture, Cycom 919 (500X)

ORIGINAL PAGE
BLACK AND WHITE PHOTOGRAPH



Figure 87. Hairy Appearance, Resin Whiskers, Cycom 937 (5000X)

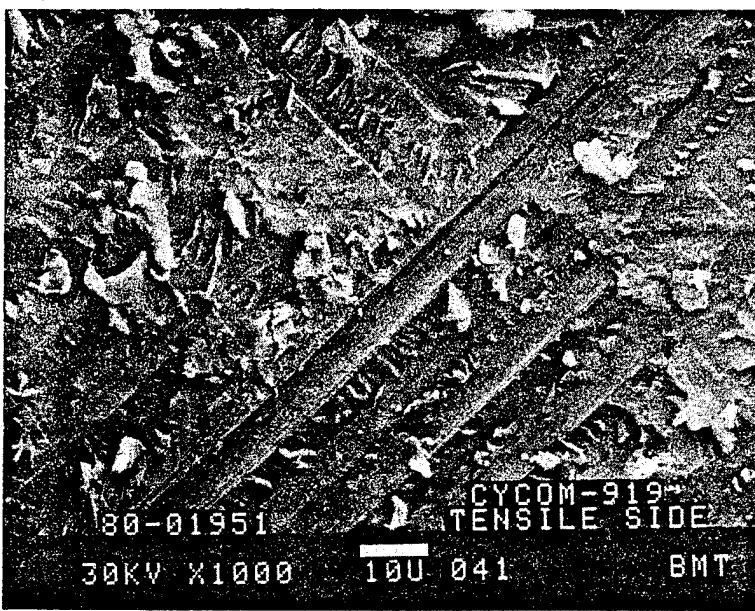


Figure 88. Feathered Hackles Indicating Plastic Flow, Cycom 919 (1000X)

ORIGINAL PAGE
BLACK AND WHITE PHOTOGRAPH

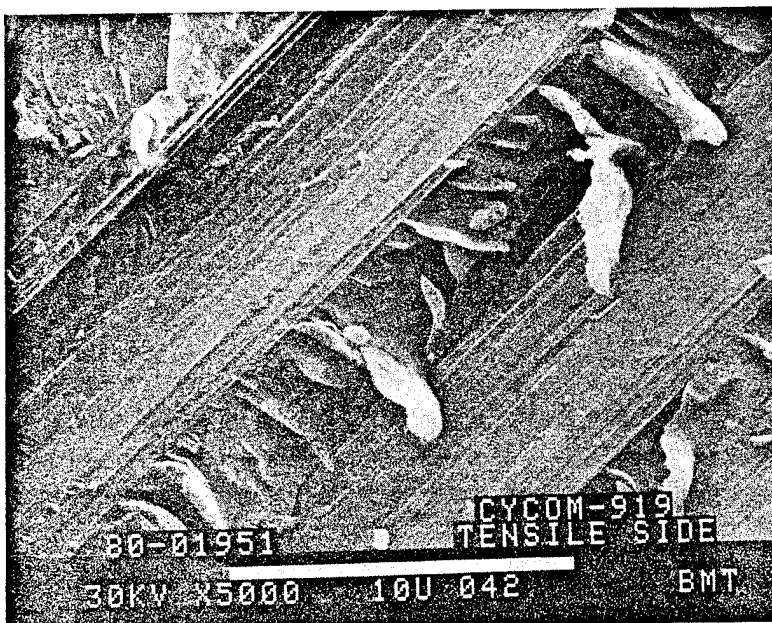


Figure 89. Resin-Fiber Bond, Cycom 919 (5000X)

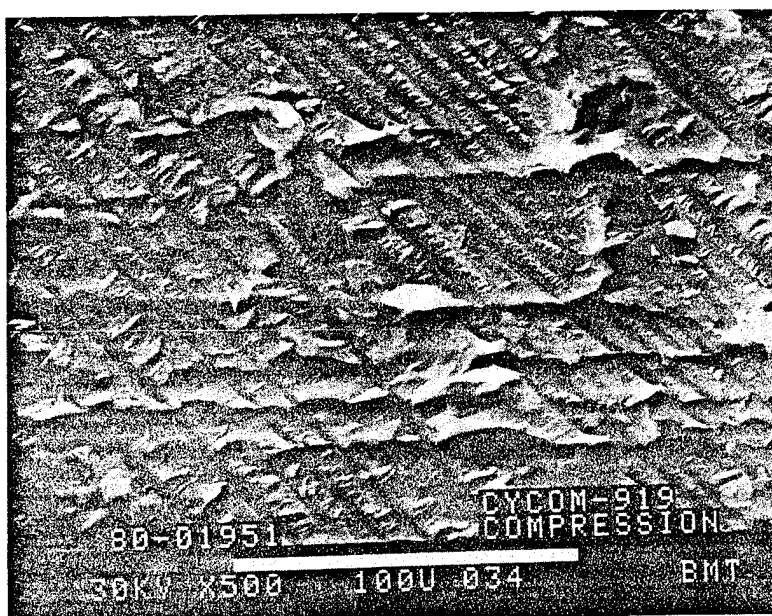


Figure 90. Compression-Loaded Shear, Cycom 919 (5000X)

ORIGINAL PAGE
BLACK AND WHITE PHOTOGRAPH



Figure 91. Resin-Fiber Bond, Cycom 919 (5000X)

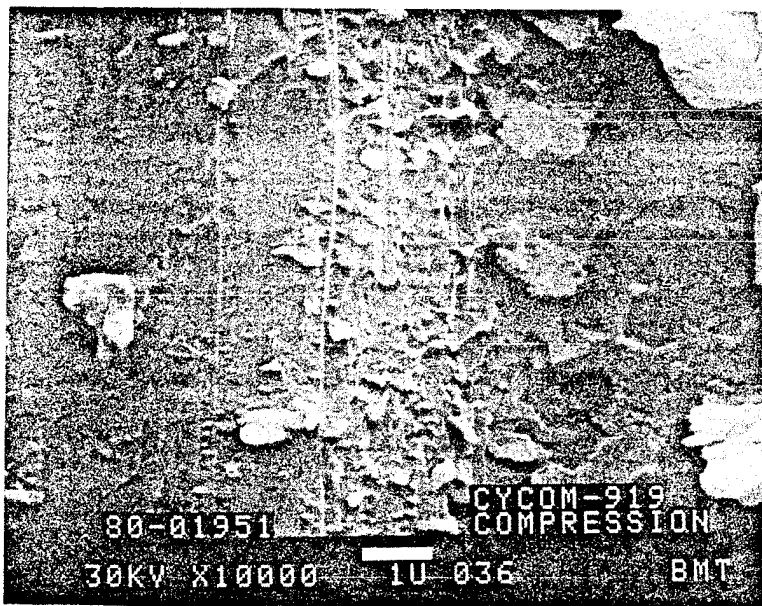


Figure 92. Resin-Fiber Bond, Exposed Fibers, Cycom 919 (10,000X)

ORIGINAL PAGE
BLACK AND WHITE PHOTOGRAPH

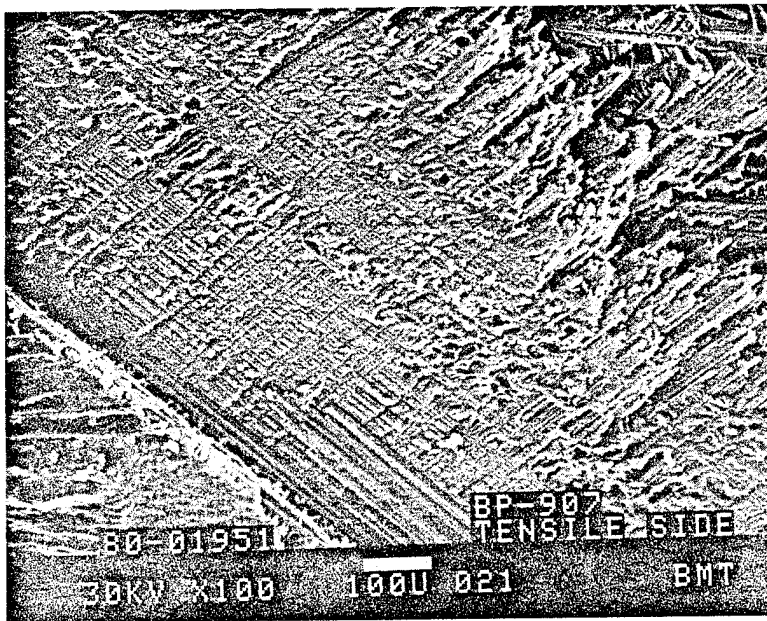


Figure 93. Delamination Face, BP-907 (100X)

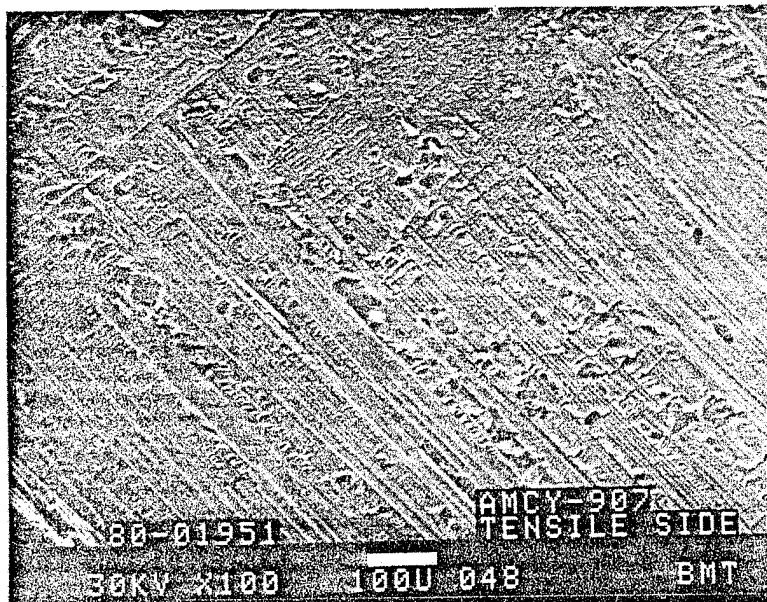
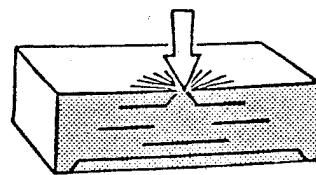
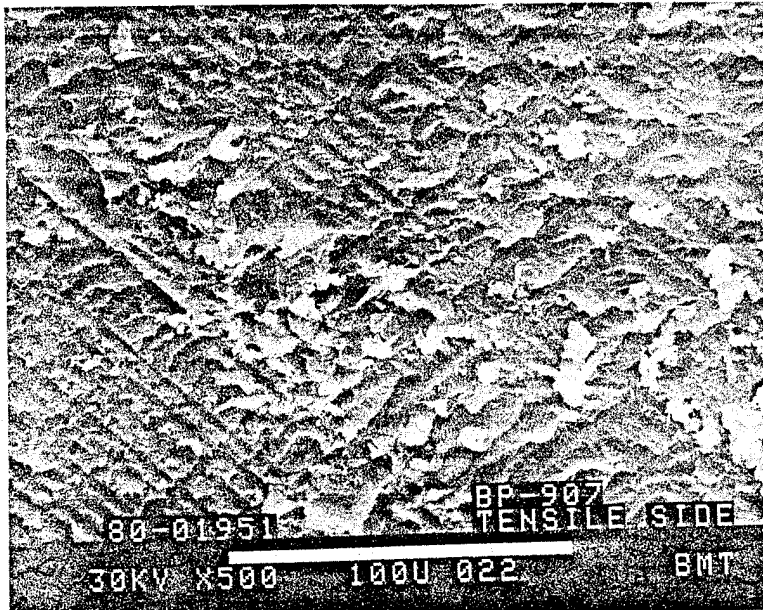


Figure 94. Similar Delamination Face, BP-907-LR (100X)

ORIGINAL PAGE
BLACK AND WHITE PHOTOGRAPH



Note: Same area as figure 93.

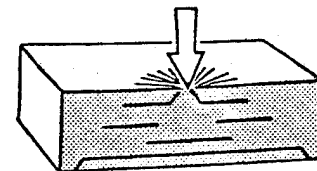
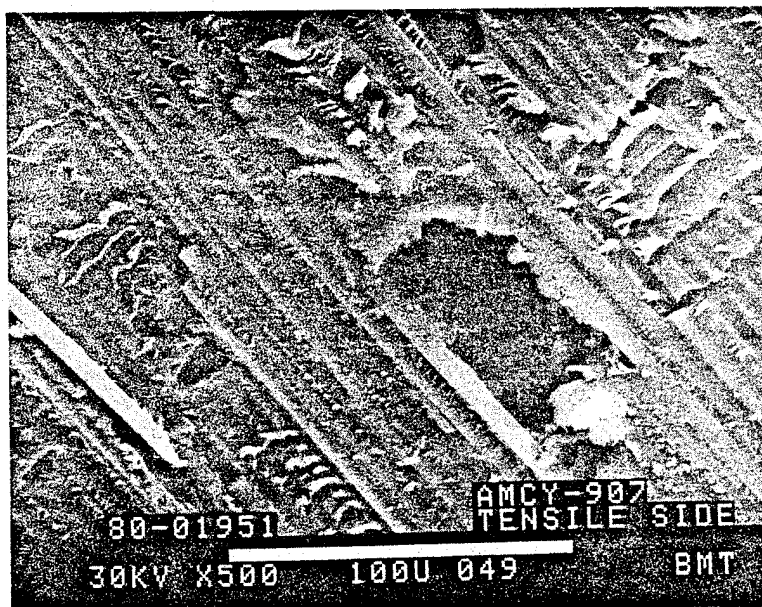


Figure 95. Delamination Face, BP-907 (500X)



Note: Same area as figure 94.

Figure 96. Delamination Face, BP-907-LR (500X)

ORIGINAL PAGE
BLACK AND WHITE PHOTOGRAPH



Figure 97. Ductile Resin Failure, BP-907 (2000X)

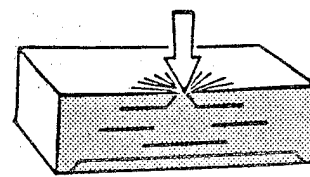


Figure 98. Brittle Cleavage Failure, BP-907-LR (2000X)

ORIGINAL PAGE
BLACK AND WHITE PHOTOGRAPH

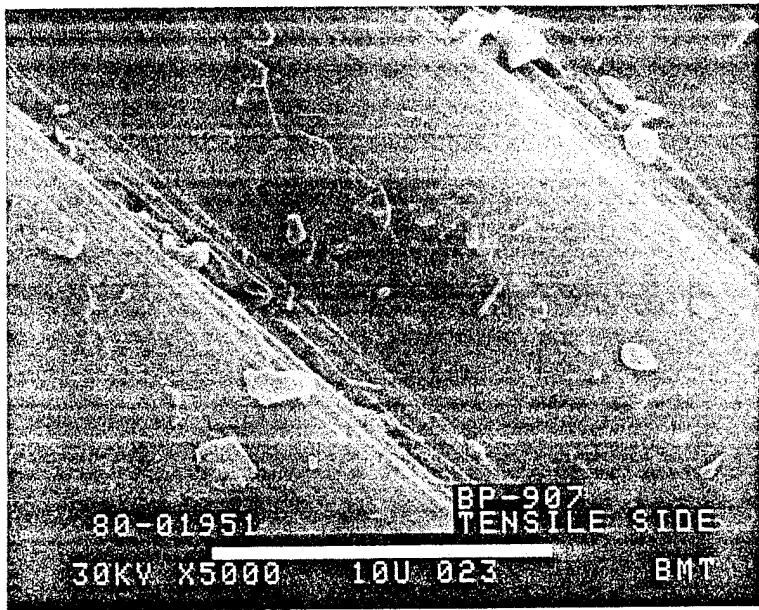


Figure 99. Microscopic Fracture Mechanism, BP-907 (5000X)

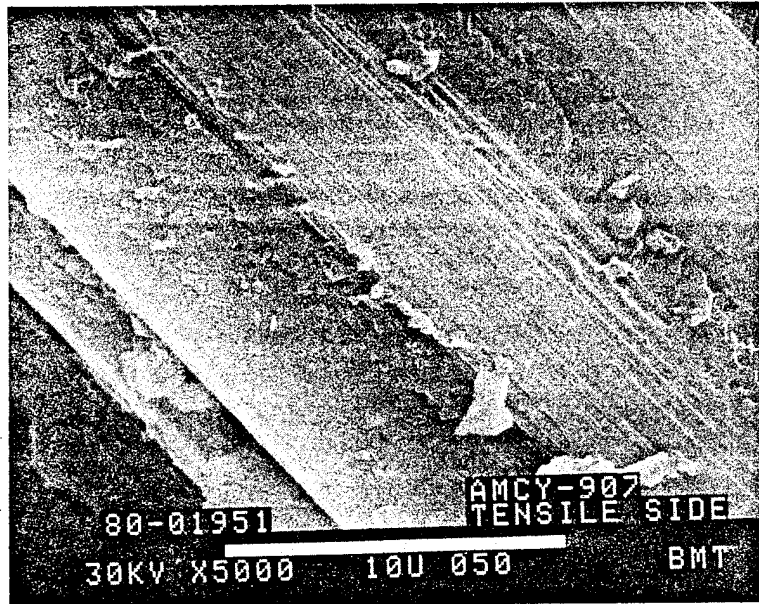
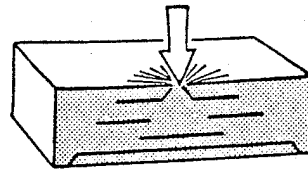


Figure 100. Microscopic Fracture Mechanism, BP-907-LR (5000X)

ORIGINAL PAGE
BLACK AND WHITE PHOTOGRAPH



Note large elongated resin blocks.

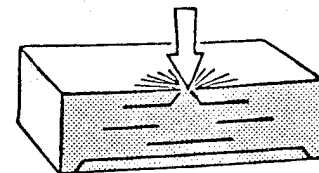
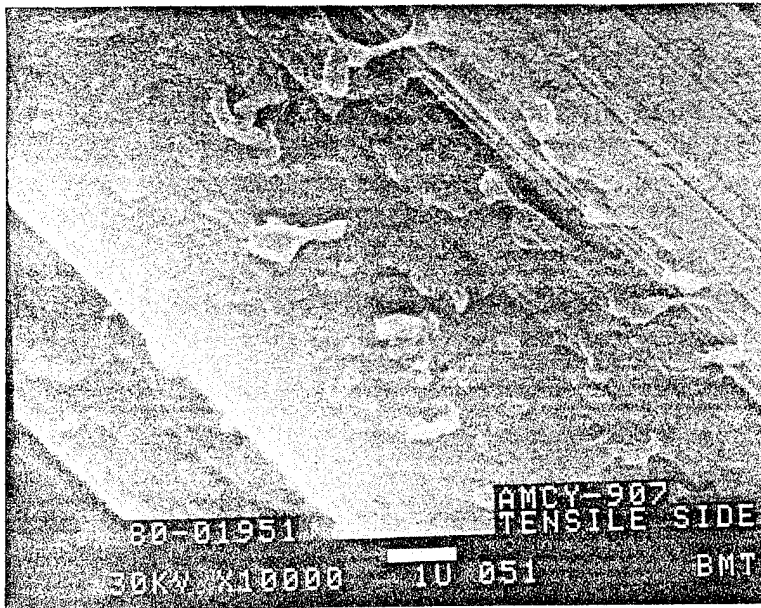


Figure 101. Resin-Fiber Bond, BP-907 (10,000X)



Note lack of large ductile flow.

Figure 102. Resin-Fiber Bond, BP-907-LR (10,000X)

ORIGINAL PAGE
BLACK AND WHITE PHOTOGRAPH



Figure 103. Compression-Loaded Shear Delamination, BP-907
(1000X)

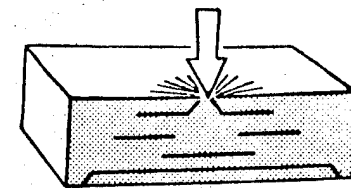
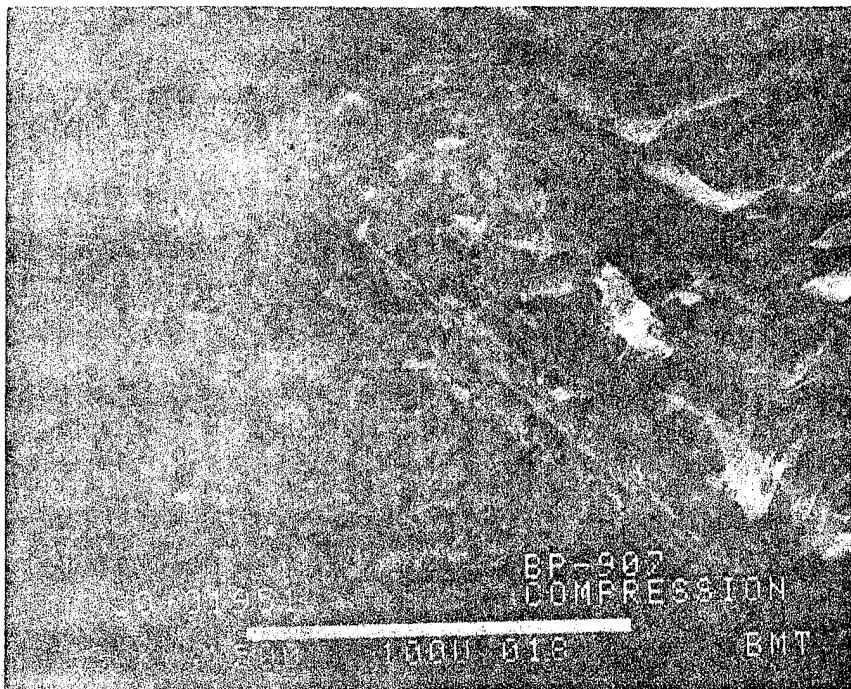


Figure 104. Compression-Loaded Shear Delamination, BP-907-LR
(100X)

ORIGINAL PAGE
BLACK AND WHITE PHOTOGRAPHY



Note: Similar face to figure 103.

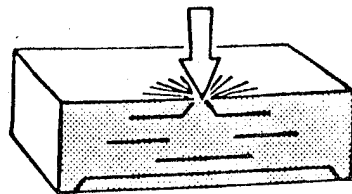
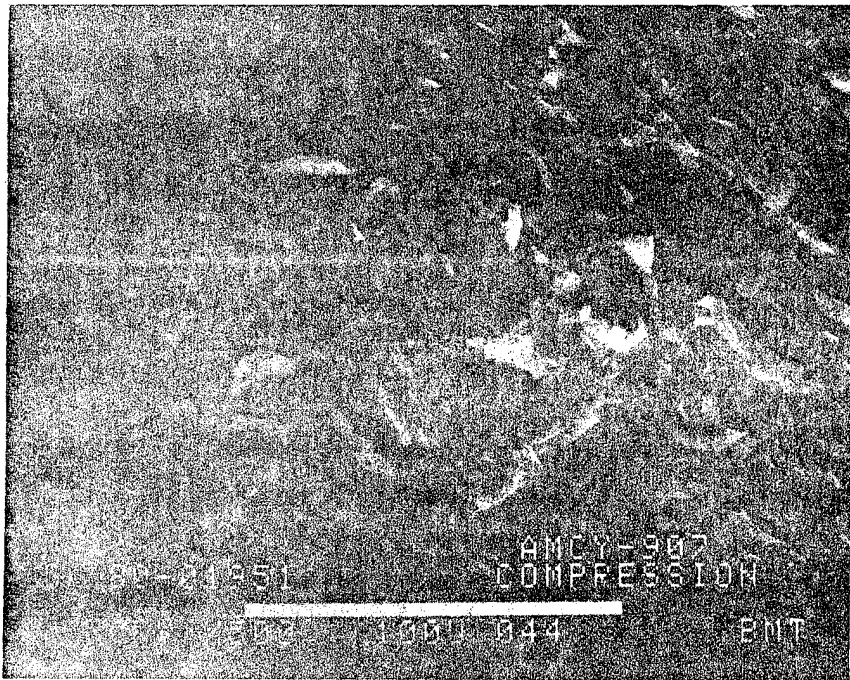


Figure 105. Ductile Flow, BP-907 (500X)



Note the lesser degree of deformation.

Figure 106. Ductile Flow, BP-907-LR (500X)

ORIGINAL PAGE
BLACK AND WHITE PHOTOGRAPH

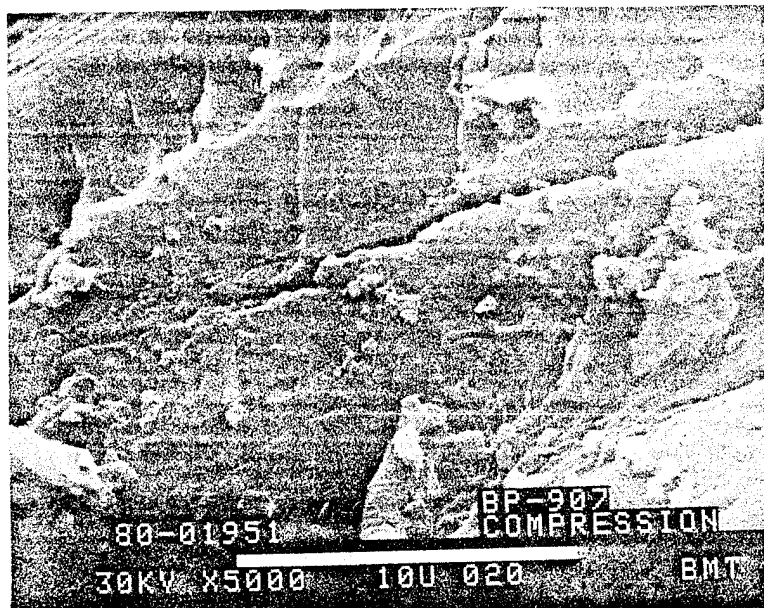


Figure 107. Microscopic Fracture Appearance, BP-907 (5000X)

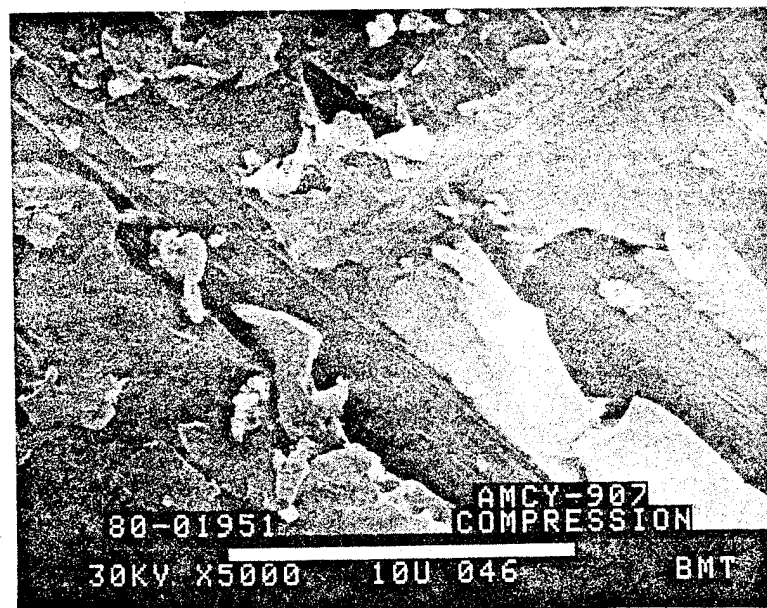
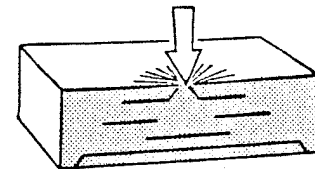


Figure 108. Microscopic Fracture Appearance, BP-907-LR (5000X)

ORIGINAL PAGE
BLACK AND WHITE PHOTOGRAPH

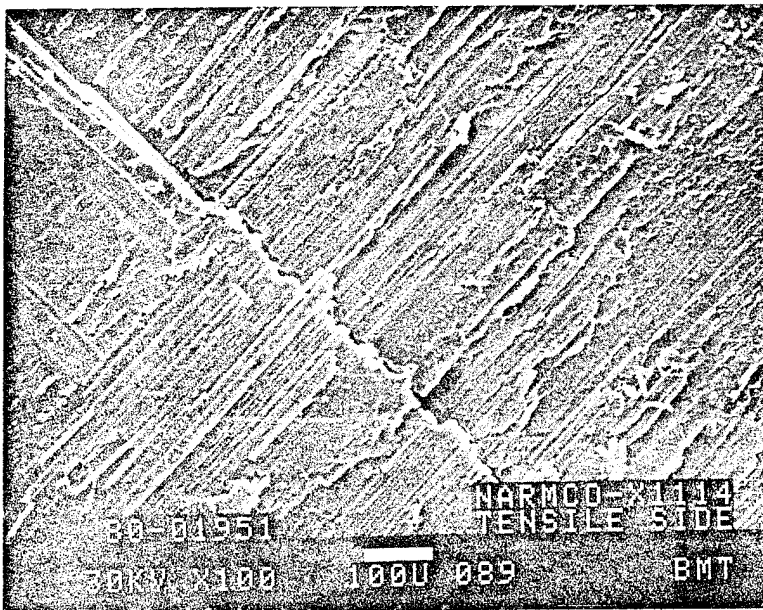


Figure 109. Shear Delamination, Narmco X1114 (100X)

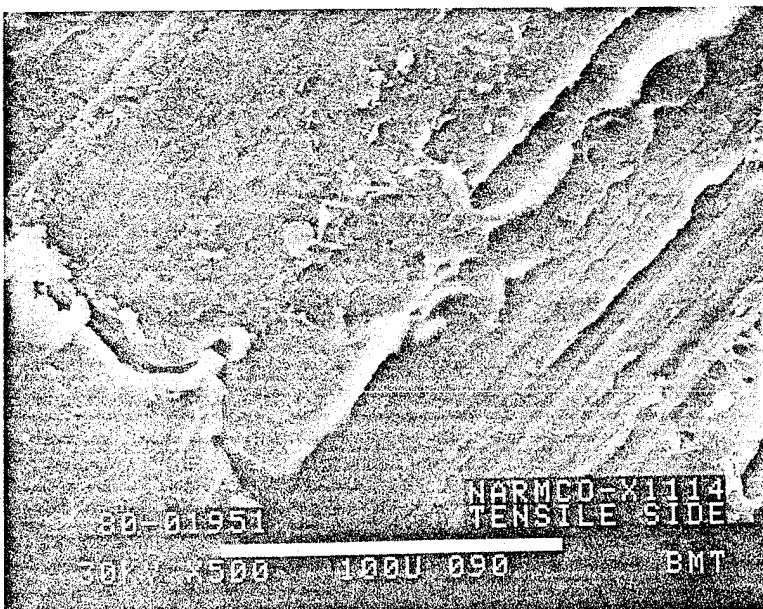
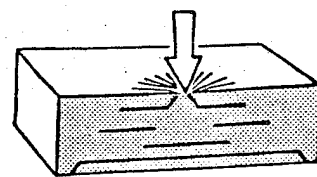


Figure 110. Shear Delamination, Narmco X1114 (500X)

ORIGINAL PAGE
BLACK AND WHITE PHOTOGRAPH

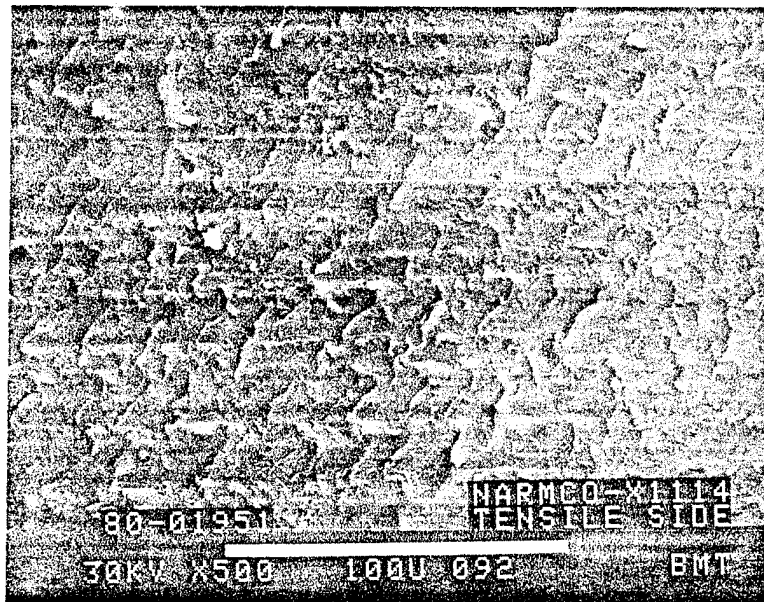
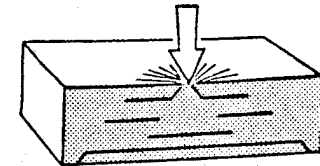


Figure 111. Deformed Resin After Shear, Narmco X1114 (500X)



Note stretched and collapsed resin.

Figure 112. Tension Failure, 90-deg Ply, Narmco X1114 (540X)

ORIGINAL PAGE
BLACK AND WHITE PHOTOGRAPH

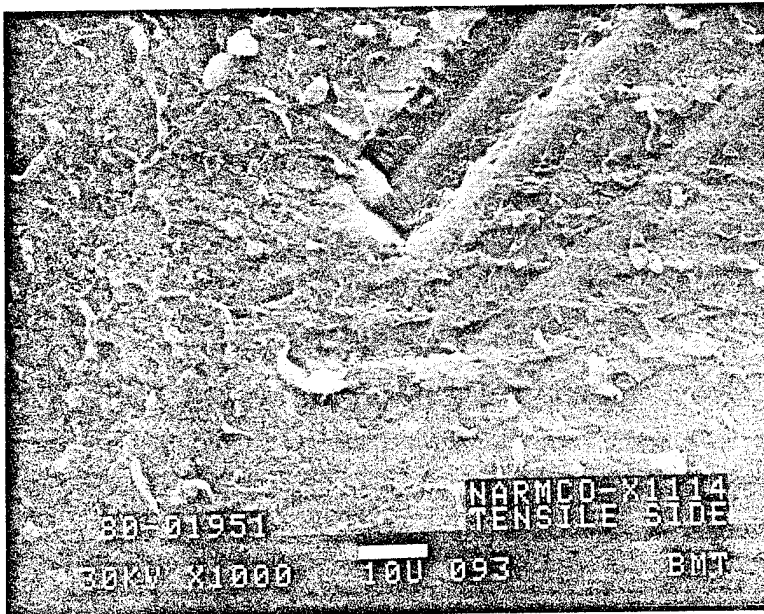


Figure 113. Delamination Face, Narmco X1114 (1000X)

Note lack of propagation of fiber failure.

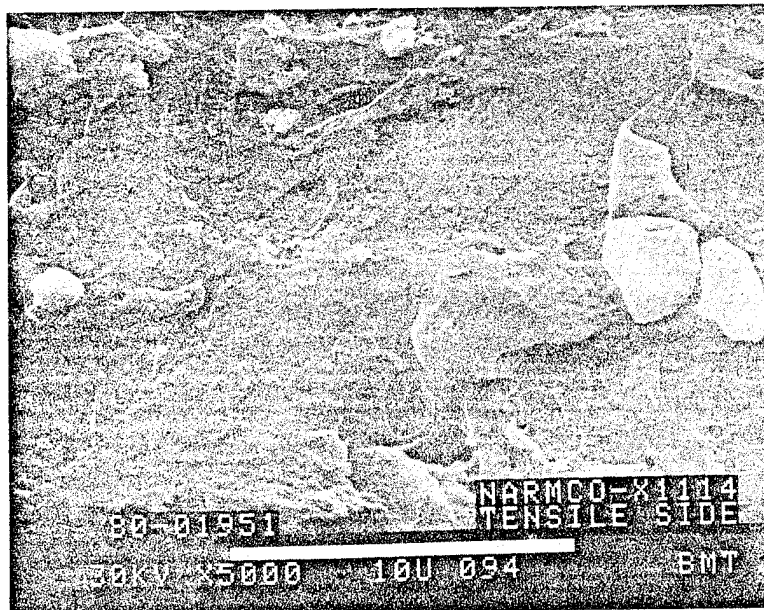
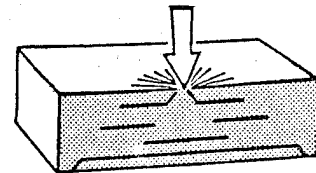


Figure 114. Fiber-Matrix Bond, Narmco X1114 (5000X)

ORIGINAL PAGE
BLACK AND WHITE PHOTOGRAPH

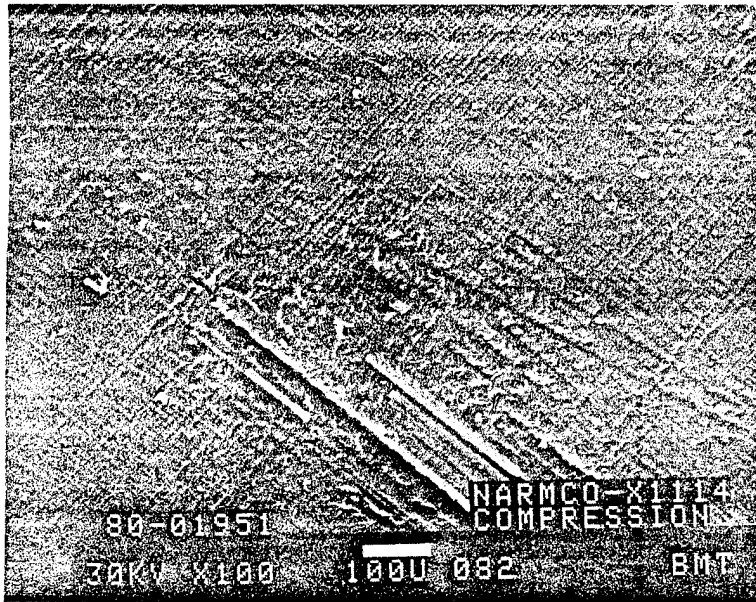
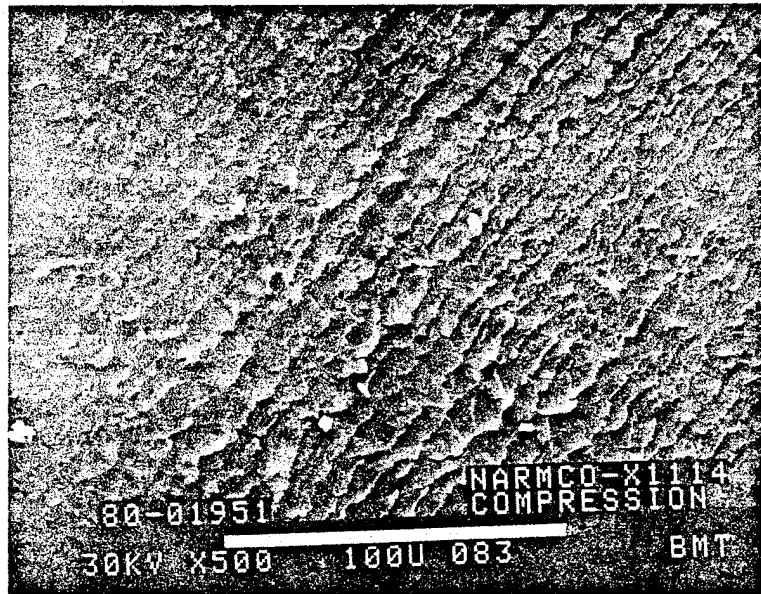
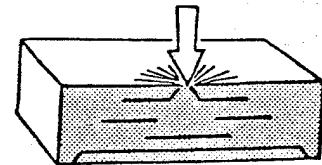


Figure 115. Compression-Loaded Shear, Narmco X1114 (100X)



Note flow in load direction.

Figure 116. Compression-Loaded Shear, Narmco X1114 (500X)

ORIGINAL PAGE
BLACK AND WHITE PHOTOGRAPH

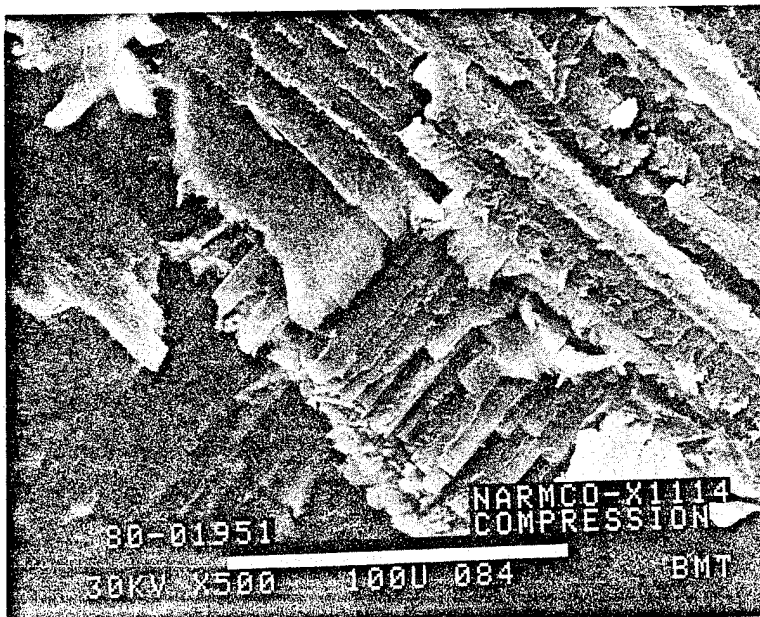


Figure 117. Deformed Resin at Crossply Boundary, Narmco X1114 (500X)

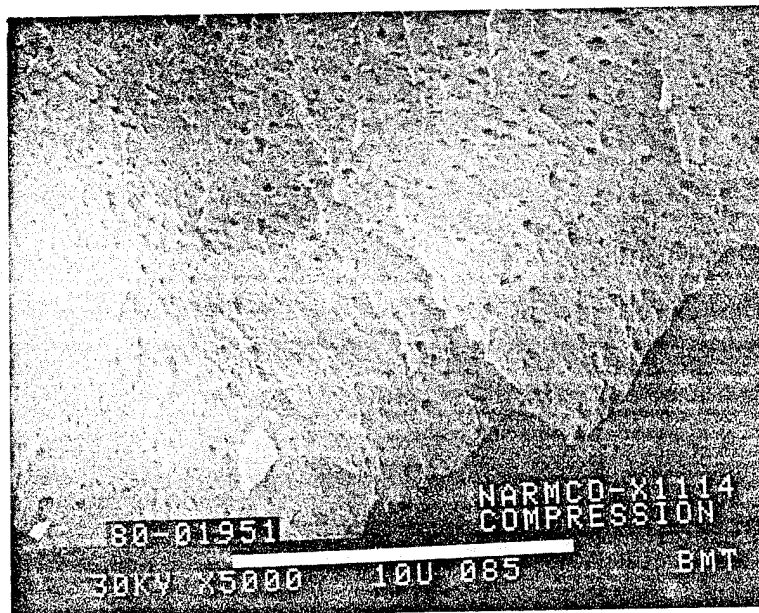
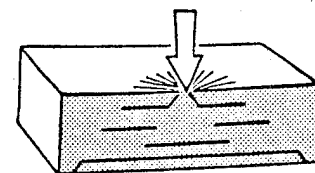


Figure 118. Deformation Pits in Flowed Resin, Narmco X1114 (5000X)

ORIGINAL PAGE
BLACK AND WHITE PHOTOGRAPH

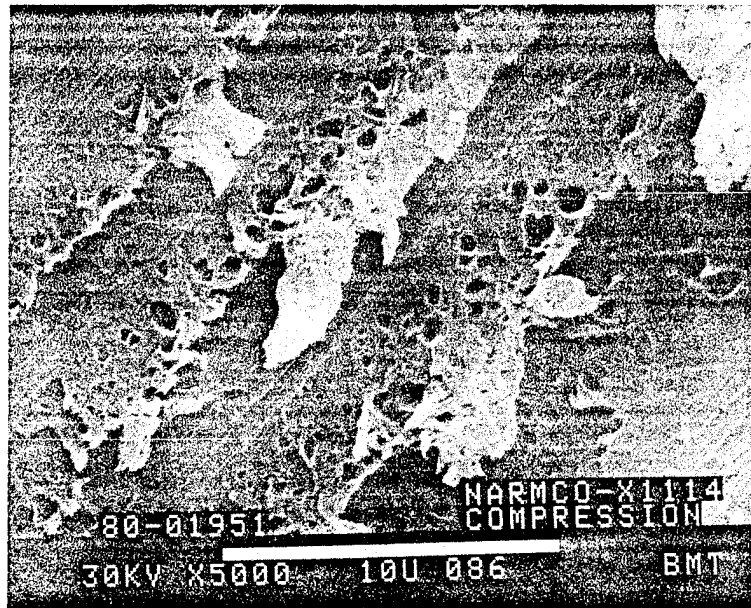


Figure 119. Possible Microvoid Formation in Strained Resin,
Narmco X1114 (5000X)

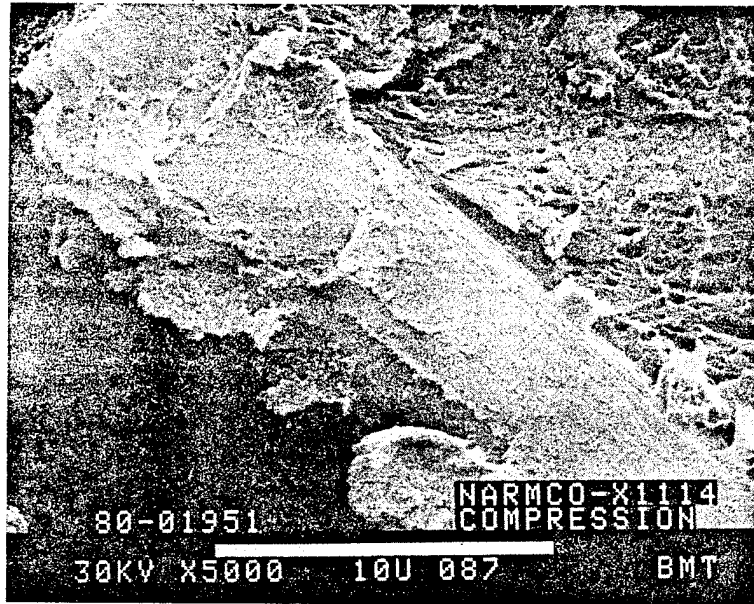
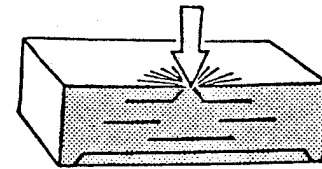


Figure 120. Fiber-Matrix Bond, Narmco X1114 (5000X)

ORIGINAL PAGE
BLACK AND WHITE PHOTOGRAPH

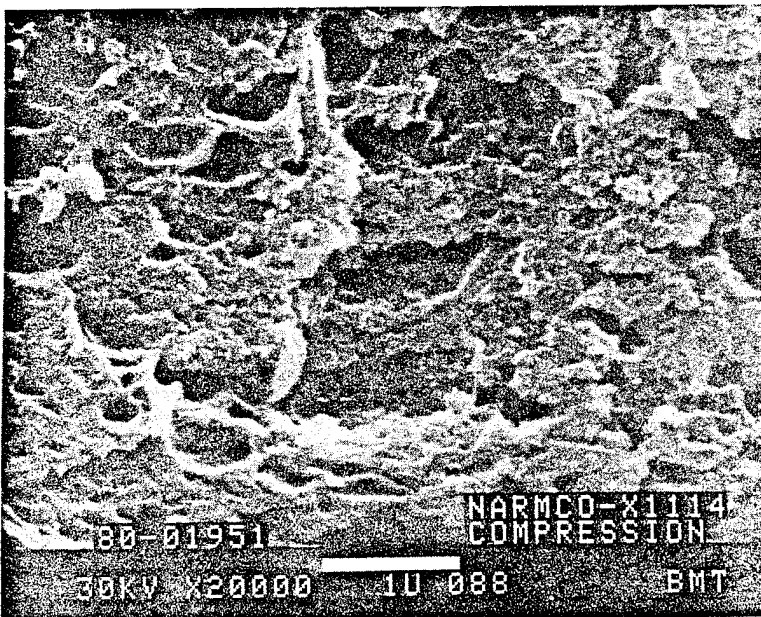


Figure 121. Possible Microvoid Initiation and Growth, Narmco X1114 (20,000X)

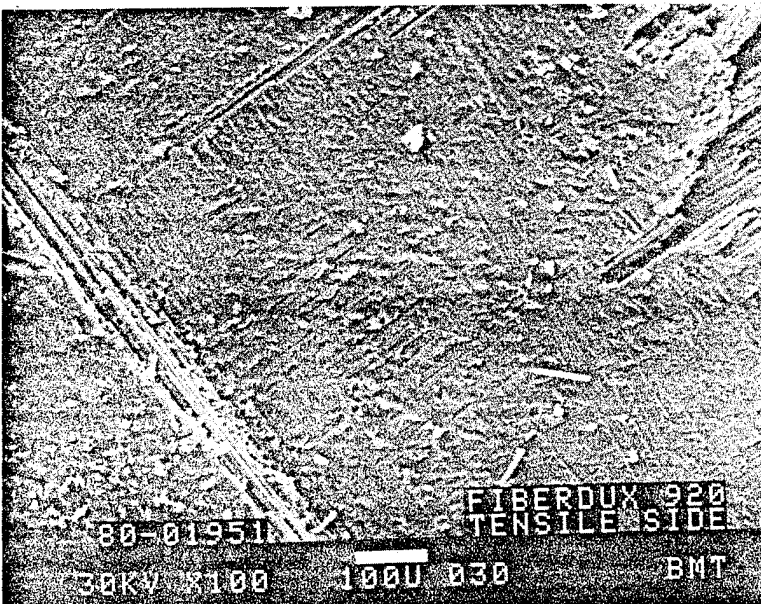
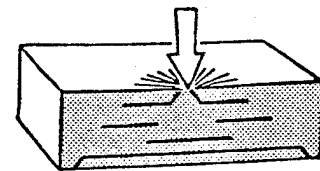


Figure 122. Delamination Face, Fibredux 920 (100X)

ORIGINAL PAGE
BLACK AND WHITE PHOTOGRAPH



Figure 123. Ductile Flow Around Fibers at Interlaminar Boundary, Fibredux 920 (500X)

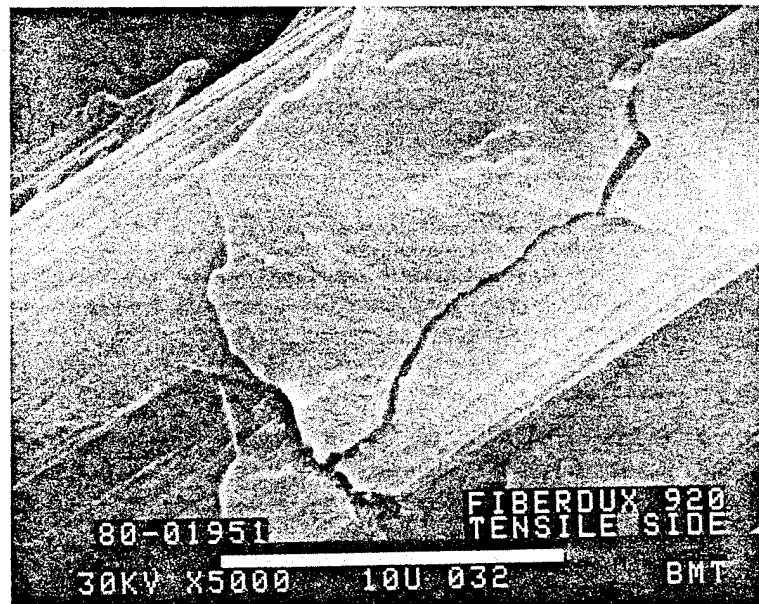
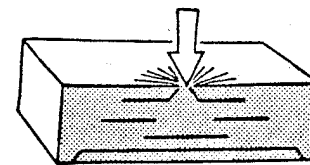


Figure 124. Crack Propagation After Fiber Failure, Fibredux 920 (5000X)

ORIGINAL PAGE
BLACK AND WHITE PHOTOGRAPH

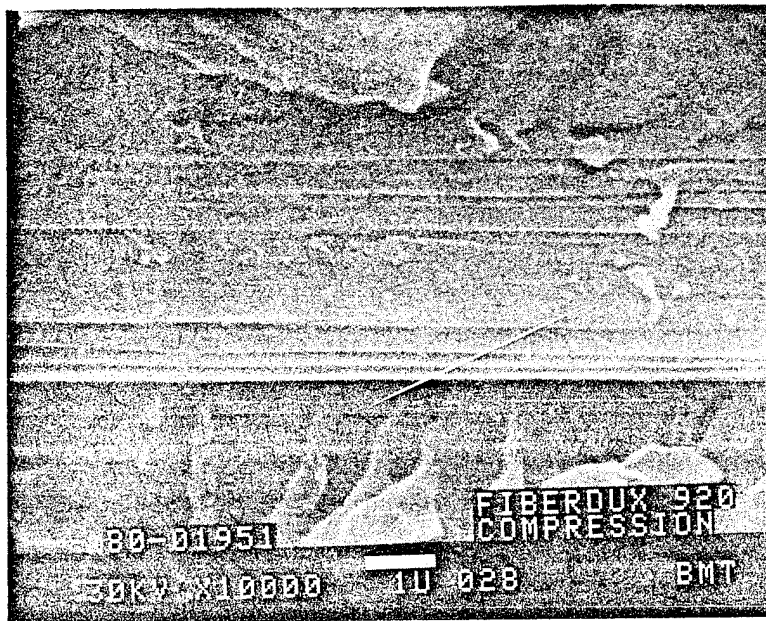


Figure 125. Fiber-Matrix Bond, Fibredux 920 (10,000X)

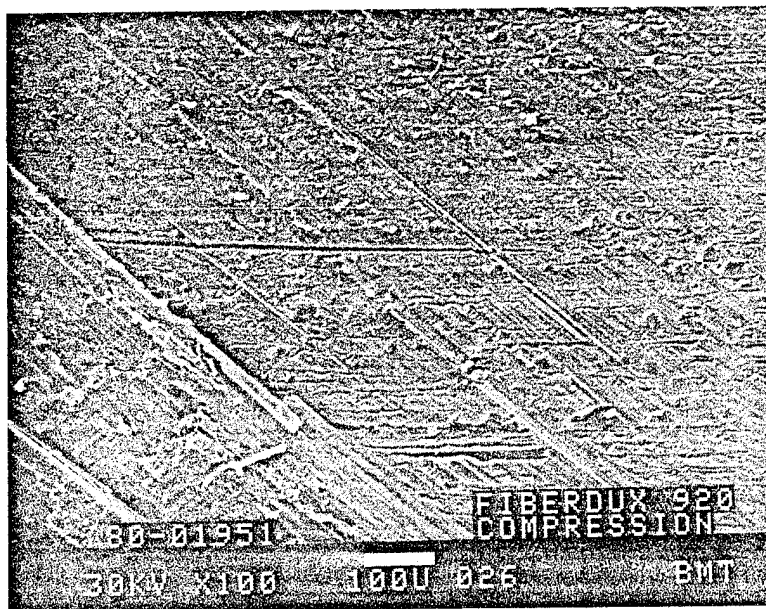
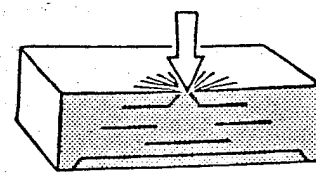
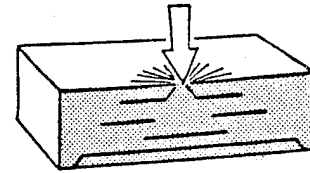
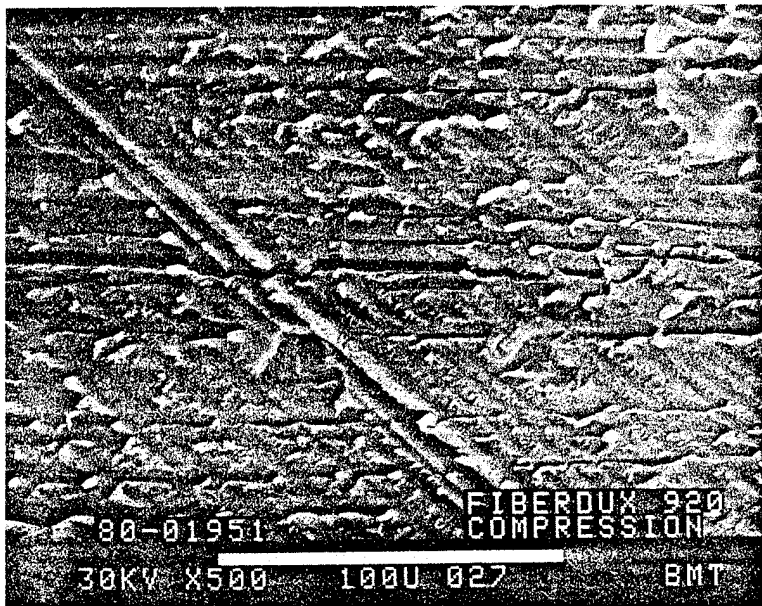


Figure 126. Compression-Loaded Shear at Interlaminar Boundary,
Fibredux 920 (100X)

ORIGINAL PAGE
BLACK AND WHITE PHOTOGRAPH



Note deformation of voids.

Figure 127. Compression Side Shear, Fibredux 920 (500X)